



UPPSALA
UNIVERSITET

*Digital Comprehensive Summaries of Uppsala Dissertations
from the Faculty of Science and Technology 1884*

Atomic Scale Modelling in Photoelectrocatalysis

*Towards the Development of Efficient Materials for
Solar Fuel Production*

GIANE B. DAMAS



ACTA
UNIVERSITATIS
UPSALIENSIS
UPPSALA
2020

ISSN 1651-6214
ISBN 978-91-513-0827-2
urn:nbn:se:uu:diva-398175

Dissertation presented at Uppsala University to be publicly examined in Å80101, Uppsala, Friday, 31 January 2020 at 13:30 for the degree of Doctor of Philosophy. The examination will be conducted in English. Faculty examiner: Professor Clas Persson (University of Oslo).

Abstract

Damas, G. B. 2020. Atomic Scale Modelling in Photoelectrocatalysis. Towards the Development of Efficient Materials for Solar Fuel Production. *Digital Comprehensive Summaries of Uppsala Dissertations from the Faculty of Science and Technology* 1884. 86 pp. Uppsala: Acta Universitatis Upsaliensis. ISBN 978-91-513-0827-2.

Using sunlight to produce valuable chemicals has been pointed out as an interesting alternative to deal with the well-known environmental problem related to the use of fossil fuels for energy generation. Thus, it is crucial for this field the development of novel photocatalysts that could drive the uphill reactions with high efficiency while presenting low price and toxicity. In this context, conjugated polymers with a donor-acceptor architecture have shown good photoactivity for the hydrogen evolution reaction (HER) due to their advantageous properties, including a broad UV-Vis absorption spectrum and thermodynamic driving force to carry out the charge transfer processes. In this thesis, a series of fluorene- and benzothiadiazole-based polymers are evaluated by means of ab initio methods as potential candidates for photocatalytic HER. A set of small-molecules with well-defined molecular weight have also been considered for this application. In general, tailoring a chemical unit has enabled an improvement of the absorption capacity in benzo(triazole-thiadiazole)-based polymers and cyclopentadithiophene-based polymers, with a higher impact exhibited upon acceptor tailoring. On the other hand, all systems under investigation present favorable thermodynamics for proton reduction or hole removal by an appropriate sacrificial agent. In particular, it is demonstrated the active role played by nitrogen atoms from the acceptor units in the hydrogenation process, whose binding strength is significantly decreased in benzo(triazole-thiadiazole)-based polymers. Furthermore, the extension of the electron-hole separation has been assessed through the calculation of the exciton binding energies, which are diminished with an improvement in the donating ability on cyclopentadithiophene-based materials.

In another approach to deal with the aforementioned problem, it has been considered the direct conversion of carbon dioxide into formic acid, an important chemical that finds applications in fuel cells, medicine and food industries. In this thesis, such electrocatalytic process has been investigated by using Sn-based electrodes and Ru-complexes. In the former case, a solid-state modelling approach based on slab geometries to model surface states has been employed to explore the reaction thermochemistry. The outcomes support the reaction mechanism where the carbon dioxide insertion into the Sn-OH bond is a thermodynamically favorable step prior to reduction, which has a redox potential in fair agreement with the measurements carried out by our collaborators. In a Ru-complex, the reaction mechanism is likely to follow the route with natural production of CO due to ligand release after the first reduction process, which is further protonated to originate the active species. In this case, the insertion occurs at the Ru-H bond to generate a carbon-bound species that is the intermediate in the formic acid production after the second protonation step. Finally, it has been studied the physical adsorption of carbon dioxide in metal-organic frameworks with a varying metallic center in a theoretical point of view.

Keywords: Photocatalytic hydrogen production, polymeric materials, donor-acceptor architecture, small molecules, density functional theory, hydrogen binding free energies, exciton binding energies, electrocatalysis, carbon dioxide conversion, formic acid production, Sn-based electrodes, Tin oxides, Ru-complexes, Metal Organic Frameworks, carbon dioxide capture.

Giane B. Damas, Department of Physics and Astronomy, Materials Theory, Box 516, Uppsala University, SE-751 20 Uppsala, Sweden.

© Giane B. Damas 2020

ISSN 1651-6214

ISBN 978-91-513-0827-2

urn:nbn:se:uu:diva-398175 (<http://urn.kb.se/resolve?urn=urn:nbn:se:uu:diva-398175>)

To my family

List of Papers

This thesis is based on the following papers, which are referred to in the text by their Roman numerals.

- I An Experimental and Theoretical Study of an Efficient Polymer Nano-Photocatalyst for Hydrogen Evolution**
Palas B. Pati, Giane B. Damas, Lei Tian, Daniel L. A. Fernandes, Lei Zhang, Ilknur B. Pehlivan, Tomas Edvinsson, C. Moyses Araujo, Haining Tian. *Energy Environ. Sci.* 2017, 10: 1372-1376.
- II On the Design of Donor-Acceptor Conjugated Polymers for Photocatalytic Hydrogen Evolution Reaction: First-Principles Theory-Based Assessment**
Giane B. Damas, Cleber F. N. Marchiori, C. Moyses Araujo. *J. Phys. Chem. C* 2018, 122(47): 26976-26888.
- III Tailoring the Electron-Rich Moiety in Benzothiadiazole-Based Polymers for Efficient Photocatalytic Hydrogen Evolution Reaction**
Giane B. Damas, Cleber F. N. Marchiori, C. Moyses Araujo. *J. Phys. Chem. C* 2019, 123(42): 25531-25542.
- IV Symmetric Small-Molecules with Acceptor-Donor-Acceptor Architecture for Efficient Visible-Light Driven Hydrogen Production: Optical and Thermodynamic Aspects**
Giane B. Damas, Fredrik von Kieseritzky, Jonas Hellberg, Cleber F. N. Marchiori, C. Moyses Araujo. Accepted in *J. Phys. Chem. C*.
- V On the Mechanism of Carbon-Dioxide Reduction on Sn-based Electrodes: Insights into the Role of Oxide Surfaces**
Giane B. Damas, Caetano R. Miranda, Ricardo Sgarbi, James M. Portela, Mariana R. Camilo, Fabio H. B. Lima, C. Moyses Araujo. *Catalysts* 2019, 9(8): 636.

VI X-Ray Photoelectron Fingerprints of High-Valent Ruthenium-oxo Complexes Along the Oxidation Reaction Pathway in Aqueous Environment

Jose L. Silva, Isaak Unger, Tiago A. Matias, Leandro R. Franco, Giane B. Damas, Luciano T. Costa, Kalil C. F. Toledo, Tulio C. R. Rocha, Arnaldo N. de Brito, Clara-Magdalena Saak, Kaline Coutinho, Koiti Araki, Olle Björneholm, Barbara Brena, C. Moyses Araujo. *J. Phys. Chem. Lett.* 2019, 10: 7636-7643.

VII Carbon Dioxide Reduction Mechanism on Ru-based Electrocatalysts: Insights from First-Principles Theory

Giane B. Damas, Dmitri Ivashchenko, Ivan Rivalta, C. Moyses Araujo. *In Manuscript*.

VIII Understanding Carbon Dioxide Capture on Metal-Organic Frameworks from First Principles Theory: The Case of MIL-53(X), with X=Fe, Al and Cu.

Giane B. Damas, Luciano T. Costa, Rajeev Ahuja, C. Moyses Araujo. *In Manuscript*.

Reprints were made with permission from the respective publishers.

Comments on my contributions for the abovementioned papers:

For articles **I-V**, **VII** and **VIII** I had the main responsibility for planning and performing the theoretical calculations, analyzing and discussing the results with the team. Furthermore, I had the main responsibility of writing and reviewing the manuscript in articles **II-V**, **VII** and **VIII**, whereas in Paper **I** this task has been limited to the theoretical assessment. In article **VI**, I have performed the quantum chemistry calculations to determine the spin states and minimum energy geometries for the Monte-Carlo simulations, also participating in the discussions throughout the work development. In fact, I have extended the electrochemistry analysis for the Ru-complexes from article **VI** to be presented in a future work.

Contents

| | |
|---|----|
| 1. Introduction..... | 9 |
| 1.1- Thesis Outline | 12 |
| 2. Theoretical Methods | 13 |
| 2.1- A Brief Introduction to Density Functional Theory..... | 13 |
| 2.1.1- The Time-Independent Schrödinger Equation | 13 |
| 2.1.2- The Electronic Density as the Central Quantity | 14 |
| 2.1.3- The Kohn-Sham Scheme | 15 |
| 2.1.4- The Exchange-Correlation Functional | 16 |
| 2.1.5- Molecular systems: Pople's Basis Sets..... | 18 |
| 2.1.6- Solid-State Modelling: Plane-Wave Basis Set | 18 |
| 2.2- Time-Dependent Density Functional Theory: Excited-state Assessment | 19 |
| 3. Molecular Modelling of Conjugated Polymers for Hydrogen Evolution . | 22 |
| 3.1. Benchmark for Density Functional Theory Methods..... | 22 |
| 3.2. On the Effects of D-A Architecture and π -spacer | 27 |
| 3.3. Replacing the Benzothiadiazole Moiety by its Derivatives or other Acceptor Units..... | 29 |
| 3.4. Donor Tailoring in Benzothiadiazole-based Polymers..... | 32 |
| 3.5. The Photocatalytic Process..... | 32 |
| 3.5.1. Optical Properties: Group A Polymers | 34 |
| 3.5.2. Optical Properties: Acceptor Tailoring..... | 36 |
| 3.5.3. Optical Properties and Electronic Structure: Donor Tailoring .. | 37 |
| 3.6. Theoretical Assessment of Redox Potentials | 39 |
| 3.6.1. Modelling the Hydrogen Evolution Reaction | 40 |
| 3.6.2. Thermodynamic Driving Force for Charge Transfer: Acceptor Tailoring | 42 |
| 3.6.3. Thermodynamic Driving Force for Charge Transfer: Donor Tailoring | 43 |
| 3.6.4. Hydrogen Binding Free Energies: Group A polymers | 44 |
| 3.6.5. Hydrogen Binding Free Energies: Acceptor Tailoring..... | 45 |
| 3.7. Kinetic Considerations | 46 |
| 3.8. Exciton Binding Energies..... | 47 |
| 4. Molecular Modelling of Symmetric Small-Molecules for Hydrogen Evolution..... | 50 |

| | |
|---|----|
| 4.1. Systems under investigation | 50 |
| 4.2. UV/Vis Absorption Spectra | 51 |
| 4.3. Reaction Thermodynamics | 52 |
| 5. Solid-State Modelling of the Carbon Dioxide Reaction on Sn-based Electrodes..... | 55 |
| 5.1. Computational Approach | 55 |
| 5.1.1. Bulk Structures | 55 |
| 5.1.2. Slab Models | 56 |
| 5.1.3. Electronic Structure | 57 |
| 5.2. Carbon Dioxide Insertion | 58 |
| 5.3. Reduction Reaction | 59 |
| 6. Molecular Modelling of Ru-complexes for Electrocatalytic Applications | 61 |
| 6.1. Computational Approach | 61 |
| 6.1.1. The $[\text{RuII}(\text{bpy})_2(\text{py})(\text{OH}_2)]^{2+}$ Complex and Derivatives | 61 |
| 6.1.2. The $[\text{RuII}(\text{bpy})_2(\text{CO})_2]^{2+}$ Complex and Derivatives | 62 |
| 6.2. Reduction Pathways for Ru- Complexes: Thermodynamics Aspects | 63 |
| 6.3. The Reaction Mechanism | 63 |
| 7. Solid-State Modelling of Metal-Organic Frameworks for Carbon Dioxide Capture | 65 |
| 7.1. Bulk Structures | 65 |
| 7.2. Electronic Structure | 66 |
| 7.3. Gas Capture | 67 |
| Sammanfattning på svenska | 69 |
| Acknowledgments | 72 |
| References | 74 |

1. Introduction

Solar energy is a natural candidate to meet the global demand for energy that is currently set at 14 TWh/year, since its incidence reaches 100 000 TWh in an annual basis with an amount given per day (274 TWh) that is found enough to fulfill the human needs.¹ In fact, the main use of fossil fuels to attain such energy demand has intensified the global warming throughout the years, a well-known environmental problem that our society has been facing since the industrial revolution.^{1,2} In such context, the solar energy harnessing by using a photocatalyst to produce electricity^{3–5}, water heating⁶ or solar fuels including hydrogen^{7–9}, alcohols or even short-chain hydrocarbons¹⁰ opens up a new area for development in clean energy that is expected to lead the market on energy production in a near future.

Techniques involving photodriven electrochemical devices for water splitting are by far better developed in comparison to carbon dioxide conversion at the present time, since the hydrogen evolution reaction (HER) is intrinsically a simpler chemical process.¹¹ In fact, this gas cannot be extracted from a natural source despite its abundance on Earth's crust, being obtained through reformation of natural gas or renewable biomass and water electrolysis, which are expensive and costly in an environmental perspective.^{7–9} The interest lying on this simple fuel is related to its high-quality as an energy carrier, showing high gravimetric energy density (143.0 MJ/Kg) compared to gasoline (44.4 MJ/Kg) for fuel-related applications at ambient conditions, besides the carbon-free residue that is generated after the combustion process.^{8,9,12,13} Nevertheless, the molecular hydrogen is already widely used in other fields, where 61% of the total production in the last decade was destined for ammonia-derived fertilizers, 23% to petroleum refinement and 9% to methanol production.^{12,14} Applications in fuel cells, power generation in turbines and space-related technologies are also taken into account.^{9,12}

The primary step on the solar-driven hydrogen generation comprises the use of an appropriate material with lower or comparable energy gap to the incident photon energy. Such need is justified by the slow kinetics associated with the hydrogen evolution reaction, which should take place at 4.40 V (pH=0, absolute potential) at ideal conditions.¹⁵ In this process, the photoexcitation promotes an electron from an occupied molecular orbital to a higher-level state that was previously empty. The molecular product is generated if the thermodynamic condition for electron transfer is fulfilled. Nonetheless, the formation of an intermediate state where the hydrogen is bonded to a specific

catalytic site or surface is associated with the need of an extra potential to drive the uphill reaction, a property known as overpotential.¹⁶ The same principle is valid for a semiconducting material, where the non-occupied levels are close enough in energy to form a conduction band that is separated from the valence states through a band gap.^{17,18}

At the valence band or highest occupied molecular orbitals in the molecular case, the effect of photoexcitation is given by the formation of an empty state with a positive charge, also referred as a hole in solid-state terminology. In an excitonic bound state, the electron-hole pair has an intrinsic electrostatic interaction whose strength is determined by the exciton binding energy.^{19,20} Such interaction can cause a return of the photoelectron to the initial state, further leading to a decrease in the photocatalytic efficiency through charge recombination processes. To overcome this problem, it is usually employed a reducing sacrificial reagent with potential for redox pair (D^+/D) lying higher than the value exhibited by the photocatalyst's redox pair (P^+/P) in order to consume the holes.^{18,21,22} In general, aliphatic amines and organic acids such as triethylamine^{21,23,24}, triethanolamine²¹, ethylenediaminetetraacetic acid (EDTA)²⁵, ascorbic acid or ascorbate^{8,21,23,26} and lactic acid^{21,27} can work quite well as sacrificial donors in presence of water, although other organic compounds have also been reported for such application. Nevertheless, some systems are found to directly promote the water decomposition without an additional reagent as mentioned by Maeda *et al.*¹⁸ In fact, the latter process is referred as photocatalytic water splitting, where the electrons/holes drive the water reduction/oxidation to produce hydrogen and oxygen molecular gases, respectively.¹⁸

Early studies at the University of Tokyo have shown the titanium dioxide (TiO_2) as a pioneer material to photocatalyze the water decomposition without applying an external bias.²⁸ Although its large band gap ($E_g=3.0$ eV)²⁹ restricts its use to the ultraviolet region, the surface-attachment of a photoadsorber improves the absorption range to the visible light, which raises the energy input and photocatalytic efficiency.^{7,30,31} In this case, the photoabsorber is a natural or synthetic dye-sensitizer that is responsible for the photoexcitation, whereas the semiconductor serves as a medium for electron transfer to produce hydrogen.^{7,30,31} First synthesized by Fujishima *et al.*³² as an oxide film, this material has been fabricated as nanoparticles, thin films, nanowires and nanotubes^{33–35}, with particular interest for doping (N, C, S, Ni)^{35,36} or decorating (CdS, CuO)^{33,37} the TiO_2 nanotubes to obtain a narrowed band gap and improved charge separation, respectively. Other several reports on oxides have been published in the last years, including doped- WO_3 ,^{38–40} ZnO ^{26,41}, CuO ⁴² and $XZnSO$ ($X=Ca$ or Sr)⁴³.

A further development in the field has enabled the fabrication of carbon-based materials for photocatalytic water splitting, which has the advantage of combining low price with earth abundance of the constituting elements. How-

ever, chemical stability, dispersibility in water and easy tunability are also desirable for future applications.^{23,44,45} Clearly, the scientific community has dedicated a great deal of attention to this topic in the last two decades, with a particular interest on the synthesis and design of organic photocatalysts. As an important example, polymeric g-C₃N₄ has been intensively investigated for HER⁴⁵⁻⁴⁸ and CO₂ reduction.^{45,49} This semiconductor is easily synthesized by thermal-condensation of N-rich precursors at 500-600° in air or inert atmosphere, exhibiting a direct band gap ($E_g = 2.7$ eV) that restrains the absorption edge to a lower wavelength, besides the fast recombination of photogenerated charges that takes place on its surface.^{44,45} These issues can be addressed by forming a heterojunction with other semiconductors^{44,50,51}, structural amorphization⁵² or by incorporating Pt,^{53,54} Ni,⁵⁵ and NiO⁵⁶ as co-catalysts. Thus, a red-shift of the absorption maximum is expected to promote a higher number of electron-hole pairs and enhanced photocatalytic efficiency, although the introduction of co-catalysts also increases the number of active sites.⁴⁵ Like TiO₂, a limited efficiency enhancement has been demonstrated by adding heteroatoms or molecular dopants or creating vacancies, but the presence of structural defects can create channels for charge recombination that are not desired, as mentioned by Ye *et al.*⁴⁵

Other subclasses of organic photocatalysts have also gained spotlight since the first publications on carbon-nitride materials. For instance, poly (azomethines) networks were obtained by polycondensation of different building blocks, but they exhibit much inferior performance in comparison with g-C₃N₄.²² In another work, Park *et al.*⁵⁷ prepared composites combining microporous organic nanorods and TiO₂/Pt systems, where the former should act as photosensitizers at $\lambda = 400$ -530 nm. The activity of 50 $\mu\text{mol h}^{-1}$ for hydrogen production in the first five hours was reported along with an enhanced stability of such composites.⁵⁷ Furthermore, a superior performance has been found for benzothiadiazole-based polymers with a donor-acceptor architecture that has a key role on the improvement of charge transfer and separation processes in these materials.⁵⁸ In general, these materials are characterized by having short-range order although the material itself is amorphous. An exception is covalent organic frameworks, a subclass of crystalline organic materials that has demonstrated HER activity even in absence of cocatalysts or sacrificial reagents.⁵⁹

An important point is that a decrease in the optical gap E_{opt} does not always lead to an improvement in the photocatalytic activity, although such reduction is expected to red-shift the absorption spectrum towards the visible region. For instance, the polycondensation of different ratios of pyrene and toluene to produce pyrene-based polymers has returned the highest amount for the system presenting an intermediate value for the optical gap ($E_{opt} = 2.33$ eV) with an absorption maximum lying at $\lambda = 534$ nm.⁶⁰ Similarly, some materials exhibit lower activity at higher wavelengths, as it is the case for the carbazole-derived

polymers synthesized by Woods *et al.*,⁶¹ where fractions with different solubilities have returned distinct performances. Particularly, the insoluble polymer showed higher efficiency at $\lambda > 295$ nm ($21.5 \mu\text{mol h}^{-1}$) whereas this value is decreased to $3.1 \mu\text{mol h}^{-1}$ at $\lambda > 420$ nm.

1.1- Thesis Outline

This thesis is divided in three parts for clarity reasons. First, I provide a brief description of the *ab initio* methodology that is utilized in this work, including the Hohenberg-Kohn theorems that constitute the core of density functional theory, as well as the Kohn-Sham approach that has been developed to apply the theory in real life. The time-dependent density functional theory is also described to provide the excited-state assessment of molecular structures, as well as the vertical electronic transitions that are necessary to compose the absorption spectra.

In Sections 3-8, I present the comprehensive summary of the publications included in this thesis. In this sense, Papers I-IV are focused on the photocatalyst design for hydrogen production by using organic materials with a donor-acceptor architecture. In particular, it has been evaluated how the structural configuration and tailoring can affect the optical and thermodynamic properties of these materials, as well as the use of hydrogen- and exciton binding energies as descriptors for the photocatalytic efficiency. These outcomes are presented in Sections 3-4. Furthermore, it has been investigated the carbon dioxide conversion reaction into formic acid on tin-based electrodes and Ru-complexes in Papers V and VII, respectively. In the former case, we have employed a solid-state approach where the surface thermochemistry has been built through the construction of slabs from a cut on the most stable facet, as determined by the surface energies (see Section 5). The Ru-complexes have their pathways of reduction and reaction mechanisms described in Section 6. In Paper VIII, it has been studied the carbon dioxide capture on metal-organic frameworks by using a solid-state modelling approach, which is presented in Section 7.

2. Theoretical Methods

In this thesis, the ground-state properties of molecular and solid-state materials have been attained in gas phase, solvated environment and solid-state within the density functional theory (DFT) framework⁶² that is implemented in Gaussian 09⁶³ and 16⁶⁴, as well as in Vienna *Ab Initio* Simulation Package (VASP).⁶⁵ This methodology has been originally formulated by Pierre Hohenberg and Walter Kohn in 1964.⁶⁶ However, it was the development of a practical approach by W. Kohn and Lu Jeu Sham (1965) that enabled the theory application in real problems.⁶⁷

In Section 2.1, I introduce the ground-state density functional theory by defining the time-independent Schrödinger equation along with the energetic contributions to the total Hamiltonian operator. I also present the core of density functional methods, i.e., the relation between electronic energy and density that was determined by the Hohenberg-Kohn (HK) theorems prior to the development of the Kohn-Sham (KS) approach. From this point, the exchange-correlation functionals and basis sets determining the level of theory for ground-state calculations will be presented in Subsections 2.1.4-2.1.6. In Section 2.2, the time-dependent density functional approach is briefly described to provide the excite-state assessment that was achieved in Papers II-IV.

2.1- A Brief Introduction to Density Functional Theory

2.1.1- The Time-Independent Schrödinger Equation

In Quantum Mechanics,⁶⁸ the wavefunction $|\psi\rangle$ defining the quantum state of a system is related to a certain property by employing an Hermitian operator, which acts over the eigenfunction multiplied by its complex-conjugated to give the expectation value. In the time-independent Schrödinger equation

$$\hat{H}\Psi = E\Psi, \quad (2.1)$$

the total energy E of the system can be obtained by using its relation with the Hamiltonian operator \hat{H} . Equation 2.2 clarifies the kinetic energy contributions from N electrons and M nuclei, as well as the interaction energy between particles with similar or distinct nature, i.e.,

$$\hat{H} = -\frac{1}{2} \sum_{i=1}^N \nabla_i^2 - \frac{1}{2} \sum_{A=1}^M \frac{1}{M_A} \nabla_A^2 - \sum_{i=1}^N \sum_{A=1}^M \frac{Z_A}{r_{iA}} + \sum_{i=1}^N \sum_{j>1}^N \frac{1}{r_{ij}} + \sum_{A=1}^M \sum_{B>A}^M \frac{Z_A Z_B}{R_{AB}}. \quad (2.2)$$

Here, the electrons are assigned with i and j labels, whereas A and B describe the nuclei. Z and R (also r) correspond to the nuclear charge and the distance between particles, respectively. In fact, this expression is written in a compact form by setting several constants to unity, including the electron mass and charge. Furthermore, the substantial difference in mass between the main atomic particles leads to a simplification in the Hamiltonian by excluding the terms associated with the nuclei motion and interaction between nuclei. Thus, the so-called *Born-Oppenheimer* approximation reduces the total Hamiltonian to its electronic form (\hat{H}_{elec}) which in turn yields the electronic energy of the system. This approximation is taken into account for further mentions about E .

2.1.2- The Electronic Density as the Central Quantity

Hohenberg and Kohn established the basis for the density functional theory by proving that using the electron density to obtain the properties of the system is plausible.⁶⁶ In other words, the first HK theorem establishes that the external potential $V_{\text{ext}}(\mathbf{r})$ and other properties of an interacting system are determined by the ground-state electron density ρ . In the second HK theorem, it is defined the relation between the ground-state energy E_0 and ρ , with a general expression for the intrinsic contributions to E_0 written as

$$E_0[\rho] = T[\rho] + E_{ne}[\rho] + E_{ee}[\rho], \quad (2.3)$$

where T is the kinetic energy and E_{ne} and E_{ee} represent the electron-nuclei and electron-electron interaction energies, respectively. In Equation 2.3, T and E_{ee} are summed up to give the universally independent Hohenberg-Kohn functional, as these terms are solely affected by the number of electrons N . At this point, it is important to highlight that the true-ground state energy is just accessible if the ground-state electron density can be attained, the so-called variational principle.⁶⁶ In practice, the impossibility to achieve this requirement leads to a resulting electronic energy that is always higher than the true-ground state value.

2.1.3- The Kohn-Sham Scheme

In the discussion held by Koch and Holthausen,⁶⁸ the kinetic energy of an interacting system appears as the main reason for the poor performance of the uniform gas model in the Thomas-Fermi scheme to determine the electronic energy of the system. In the Kohn-Sham scheme⁶⁷, this problem was overcome by assuming the kinetic energy T_s of a *non-interacting system* is described by an expression based on the Hartree-Fock (HF) theory as a functional of the electron density ρ ,

$$T_s [\rho] = -\frac{1}{2} \sum_i^N \langle \varphi_i | \nabla^2 | \varphi_i \rangle \quad (2.4)$$

where the Kohn-Sham orbitals $|\varphi_i\rangle$ are one-electron wavefunctions with spatial (\mathbf{r}) and spin (s) components, similar to the spin orbitals defined in the HF theory. In Equation 2.5, T_s is a counterpart that is added to other functionals to provide a good description of an *interacting* system,

$$E[\rho] = T_s[\rho] + J[\rho] + E_{ne}[\rho] + E_{xc}[\rho], \quad (2.5)$$

with J representing the classic Coulomb energy, whereas E_{xc} comprises the non-classical contributions to the correlation energy as well as the part of the kinetic energy that is not treated by the HF approach. In this sense, J is given by the following expression

$$J[\rho] = -\frac{1}{2} \sum_i^N \sum_j^M \iint |\varphi_i(\mathbf{r}_1)|^2 \frac{1}{r_{12}} |\varphi_j(\mathbf{r}_2)|^2 d\mathbf{r}_1 d\mathbf{r}_2. \quad (2.6)$$

Here, the probability of finding simultaneously two electrons at the volume elements defined by $d\mathbf{r}_1 d\mathbf{r}_2$ is given by the pair density $|\varphi_i(\mathbf{r}_1)|^2$ and $|\varphi_j(\mathbf{r}_2)|^2$ weighed by the distance between these particles (r_{12}). Furthermore, the functional describing the electron-nuclei interaction E_{ne} is determined as follows

$$E_{ne} [\rho] = \sum_i^N \int \sum_A^M \frac{Z_A}{r_{1A}} |\varphi_i(\mathbf{r}_1)|^2 d\mathbf{r}_1. \quad (2.7)$$

Thus, the electronic states described by the Kohn-Sham orbitals $|\varphi_i\rangle$ are related to the orbital energies ε_i through the Schrödinger-like equation

$$\left(-\frac{1}{2}\nabla^2 + V_{eff}(\mathbf{r})\right)\varphi_i = \varepsilon_i\varphi_i, \quad (2.8)$$

where the summation over the squared $|\varphi_i\rangle$ gives the electron density of the system,

$$\rho(\mathbf{r}) = \sum_i^N \sum_s |\varphi_i(\mathbf{r}, s)|^2. \quad (2.9)$$

In Equation 2.8, the term in parenthesis is called Kohn-Sham operator \hat{f}^{KS} , which includes an effective potential V_{eff} that is basically the sum between J ,

E_{ne} and E_{xc} counterparts. Here, it is important to mention that the KS equations are solved in a self-consistent procedure, where the search of new KS orbitals $|\varphi_i\rangle$ is performed iteratively until a certain convergence criterium is reached.

2.1.4- The Exchange-Correlation Functional

The exchange-correlation functional E_{xc} is considered to be a bottleneck for the development of density functional theory methods since this unknown quantity has only been determined to an approximated form until the present moment. In this sense, the validity of the Koopman's theorem in HF theory is not extended to the Kohn-Sham approach, i.e, the orbital energies ε_i cannot be associated with the ionization energies, excepting the maximum energy eigenvalue ε_{max} that can hold this relation with the employment of an exact E_{xc} .^{68–70} In fact, this relation can be used to estimate how close the approximated functional is to the exact form, which is expected to affect its ability to describe the properties of interest for a system under investigation.⁷⁰ Furthermore, it is fundamental to validate the theoretical methodology by testing how accurate is the functional to reproduce experimental values or well-known properties prior to any prediction assessment.

In Papers V and VIII, the Perdew, Burke and Enzerhof (PBE)⁷¹ functional has been employed to describe the reaction thermochemistry involved in the carbon dioxide conversion on Sn-based electrodes as well as the gas capture in metal organic frameworks, respectively. This functional has roots on the generalized gradient approximation (GGA), which assumes the idea of a uniform electron gas model with exchange-correlation energy per particle ε_{xc}^{GGA} depending on the electron density and its gradient to include the information about the ρ inhomogeneity, i. e.,^{71,72}

$$E_{xc}^{GGA} = \int \rho(\mathbf{r}) \varepsilon_{xc}^{GGA}[\rho(\mathbf{r}), \nabla\rho(\mathbf{r})] d\mathbf{r} \quad (2.10)$$

which is rewritten as

$$E_{xc}^{GGA} = \int \varepsilon_x^{hom} \rho(\mathbf{r}) F_{xc}[\rho(\mathbf{r}), \nabla\rho(\mathbf{r})] d\mathbf{r}, \quad (2.11)$$

where F_{xc} is a dimensionless quantity with a varying parametrization among different functionals. In general, this approximation fails on the description of the electronic structure of semiconductors and insulators by overestimating their intrinsic band gaps, but it does provide reasonable description of thermodynamic properties of solid-state materials. In Paper V, this fact has been evidenced on the redox potential for our SnOOH model, which is in fair agreement in comparison with the value measured by our collaborators. Nonetheless, it was still necessary to improve the level of theory by using the HS06⁷³ hybrid functional with 38% of exact exchange to determine the band gap with

high accuracy for the Sn-based electrodes. In Paper VIII, such improvement has been achieved by applying Hubbard corrections on d states from Fe and Cu atoms. However, the thermodynamics associated with the gas capture has been significantly affected by the use of such corrections due to the presence of spin-polarization effects in the metal-organic frameworks.

In Papers I, VI and VII, the functional E_{xc} has been treated by using the three-parameter B3LYP⁷⁴ functional, which is well-known to exhibit a good agreement with the experimental orbital energies for polymeric materials.⁷⁵ In Papers II-IV, other functionals have been used to improve the description of dispersion effects and non-covalent interactions, such as CAM-B3LYP,⁷⁶ M06⁷⁷ and M06-2X⁷⁷. Here, the discussion is restricted to B3LYP and M06, which have provided the best results for frontier orbital energies and optical properties in the theoretical benchmark. This point will be addressed in Section 3.1.

The B3LYP⁷⁴ is a hybrid functional based on the adiabatic connection formula,^{68,74} whose integration over the non-classical contribution to the exchange-correlation energy is given at the limits of a non-interacting system ($\lambda=0$) and a fully interacting system, $\lambda=1$. As seen in Equation 2.12,^{63,68,74,78}

$$E_{xc}^{B3LYP} = E_{xc}^{LSD} + a(E_x^{exact} - E_x^{LSD}) + bE_x^{B88} + c(E_c^{LYP} - E_c^{LSD}), \quad (2.12)$$

this functional has a portion of exact exchange (E_x^{exact}) to represent the lower limit ($\lambda=0$) added to the local and gradient-corrected terms (E_x^{B88}), whereas the LDA exchange-functional describes the fully interacting system. The correlation part is composed by non-local and local contributions expressed by the LYP and LSD functionals, respectively, although the VWN III functional is used for local correlation in Gaussian implementation.^{63,64} In Equation 2.12, $a=0.20$, $b=0.72$ and $c=0.81$, according to the original parametrization with the heats of formation of small molecules⁷⁴.

M06⁷⁷ is a hybrid functional that has been designed mainly for thermochemistry, non-covalent interactions and determination of barrier heights.⁷⁷ It contains 27% of HF exchange, whose expression is

$$E_x^{M06} = \sum dr [F_{x\sigma}^{PBE}(\rho_\sigma, \nabla\rho_\sigma) f(w_\sigma) + E_{x\sigma}^{LSD} f_x(x_\sigma, z_\sigma)], \quad (2.13)$$

where $F_{x\sigma}^{PBE}$ and $E_{x\sigma}^{LSD}$ are the energy density for exchange from the PBE model and the local spin density approximation for exchange, respectively. Above, $f(w_\sigma)$ is the spin kinetic energy density enhancement factor and x_σ is the reduced spin density gradient. In Equation 2.13, the dimensionless function $f_x(x_\sigma, z_\sigma)$ is non-local, being previously developed by Voorhis & Scuseria (1998)⁷⁹ for their functional VSXC, which is the basis for E_x^{M06} . The correlation form combines contributions from opposite-spin and parallel-spin separately and will not be described here for simplicity reasons.

2.1.5- Molecular systems: Pople's Basis Sets

In Gaussian 09⁶³ and 16⁶⁴, the Kohn-Sham (KS) equations are solved by expanding the KS molecular orbitals $|\varphi_i\rangle$ in a set of L basis functions η_μ , in the context of the linear combination of atomic orbitals expansion (LCAO),^{63,68,80}

$$\varphi_i = \sum_{\mu=1}^L c_{\mu i} \eta_\mu. \quad (2.14)$$

Thus, the KS equation can be rewritten as

$$\hat{f}^{KS}(\mathbf{r}) \sum_{v=1}^L c_{vi} \eta_{v_i}(\mathbf{r}_1) = \varepsilon_i \sum_{v=1}^L c_{vi} \eta_v(\mathbf{r}_1). \quad (2.15)$$

In Equations 2.14 and 2.15, the pre-defined basis function η_μ is a real function that should be complete to provide an exact φ_i . Although it is necessary to have an infinite L set, it is more achievable in practical terms to have a large basis set, not complete. Both sides of Equation 2.15 are multiplied to the basis η_μ and integrated over the space to give

$$\sum_{v=1}^L c_{vi} \int \eta_\mu(\mathbf{r}_1) \hat{f}^{KS} \eta_v(\mathbf{r}_1) d\mathbf{r}_1 = \varepsilon_i \sum_{v=1}^L c_{vi} \int \eta_\mu(\mathbf{r}_1) \eta_v(\mathbf{r}_1) d\mathbf{r}_1. \quad (2.16)$$

In Equation 2.16, the first integral is an element of the Kohn-Sham matrix ($F_{\mu\nu}^{KS}$) and the overlap matrix contains elements defined by the right-side integral. Outside the integrals, a c_{vi} also results in a matrix C with expansion vectors, and ε_i contains the orbital energies as a diagonal matrix. According to Koch and Holthausen⁶⁸, this equation is easily solved computationally.

In this thesis, the set of basis functions 6-311G**⁸⁰⁻⁸³ was chosen to create the molecular orbitals by expanding the Kohn-Sham orbitals. This basis set combines primitive gaussian-type functions with the contraction coefficients $d_{a\tau}$ in the general form,⁶⁸

$$\eta_\tau^{CGF} = \sum_a^A d_{a\tau} \eta_a^{GTO}. \quad (2.17)$$

As a triple-zeta basis set⁸², this basis set employs six primitive gaussian functions to represent each atomic orbital basis function whereas the valence orbitals are composed by three kind of basis functions <311>. Additionally, the adaptation to the molecular environment is ensured by employing polarization functions at the d and p orbitals.^{68,82}

2.1.6- Solid-State Modelling: Plane-Wave Basis Set

In solid-state modelling, the expansion of the Kohn-Sham orbitals $|\varphi_k\rangle$ should consider the periodicity of the crystal lattice. In this sense, the Bloch theorem for solid-state materials defines $|\varphi_k\rangle$ as the product of the periodic function $u_k(\mathbf{r})$ and the plane wave $e^{ik \cdot \mathbf{r}}$, i.e.

$$\varphi_{\mathbf{k}}(\mathbf{r}) = u_{\mathbf{k}}(\mathbf{r})e^{i\mathbf{k}\cdot\mathbf{r}}, \quad (2.18)$$

where \mathbf{k} is the crystal vector in the first Brillouin zone.⁸⁴ Thus, the expansion of the so-called plane-wave basis set is given by the relation

$$\varphi_{\mathbf{k}}(\mathbf{r}) = \frac{1}{\sqrt{\Omega_{cell}}} \sum_j c_j^n(\mathbf{k}) e^{i(\mathbf{k}+\mathbf{K}_j)\cdot\mathbf{r}}, \quad (2.19)$$

where Ω_{cell} , \mathbf{K}_j and n stand for volume of the primitive cell, reciprocal lattice vectors and band index, respectively. In practical calculations performed using VASP⁶⁵ code or other software packages, it is quite important to determine the so-called cutoff energy for the plane-wave basis set E_{cut} , which establishes a limited value for this quantity during the $|\varphi_{\mathbf{k}}\rangle$ search in the self-consistent procedure:

$$E_{cut} = \frac{\hbar^2}{2m} K_{cut}^2 \quad (2.20)$$

where

$$|\mathbf{K} + \mathbf{k}| < K_{cut}. \quad (2.21)$$

Thus, a higher E_{cut} leads to a larger number of plane-waves that are used in the calculation, which increases the computational time without necessarily improving the outcomes. In general, we can determine an appropriate value for E_{cut} by doing convergence tests on the electronic energy of the system under investigation. Furthermore, the number of k-points sampling the first Brillouin Zone should also be tested for a proper assessment of chemical or physical properties without using unnecessary computational effort.

2.2- Time-Dependent Density Functional Theory: Excited-state Assessment

The time-dependent Density Functional Theory (TD-DFT) is a popular^{85–89} approach to access the excited-state related properties, based on the time-dependent Schrodinger Equation for a many-body wavefunction $\Psi(t)$ at the initial state,

$$\Psi(t) = i \frac{\partial}{\partial t} \Psi(t). \quad (2.22)$$

Here, the Hamiltonian operator is given by the contribution of the time and space-dependent functionals describing the electronic kinetic energy \hat{K} , the

nuclei-electron \hat{V}_{ext} and electron-electron interactions \hat{V}_{ee} , where the time-dependent wavefunction is related to the initial state Ψ_0 by a factor $e^{-i\alpha(t)}$,

$$\Psi(t) = e^{-i\alpha(t)} \Psi[\rho, \Psi_0](t). \quad (2.23)$$

As previously described in the ground-state theory, Ψ_0 is approximated by choosing a single determinant of Kohn-Sham orbitals $\phi_i(\mathbf{r}, 0)$ to satisfy Equation 2.8. Similarly, in the time-dependent theory, the summatory of $|\phi_i(\mathbf{r}, t)|^2$ for N -electrons defines the non-interacting electron density $\rho(\mathbf{r}, t)$ that is used to represent the true interacting system.^{68,87-89} In this sense, the Runge-Gross theorem determines the one-to-one correspondence between the time-dependent density $\rho(t)$ of this system and the external potential, being $\rho(t)$ essential to obtain the other properties of an interacting many-body system.⁸⁷⁻⁸⁹ Hence, the time-dependent KS equation is given by

$$\left[\left(-\frac{1}{2} \nabla^2 + V_{KS}(\mathbf{r}, t) \right) \phi_j(\mathbf{r}, t) \right] = i \frac{\delta \phi_j(\mathbf{r}, t)}{\delta t}. \quad (2.24)$$

In Equation 2.24, the Kohn-Sham potential V_{KS} contains the exchange correlation potential V_{xc} to provide a reasonable description of the interacting system, besides the other contributions concerning the classical electron-electron interactions and electron-nuclei attraction potentials. In this sense, V_{xc} is given by the derivative of the time-dependent exchange-correlation energy A_{xc} in respect to $\rho(\mathbf{r}, t)$,

$$V_{xc} = \frac{\partial A_{xc}[\rho(\mathbf{r}, t)]}{\partial \rho(\mathbf{r}, t)} \cong \frac{\partial E_{xc}[\rho]}{\partial \rho(\mathbf{r})}, \quad (2.25)$$

a relation that is adiabatically approximated to the time-independent exchange-correlation, as expressed in the right side of Equation 2.25.⁸⁵⁻⁸⁹ In linear response TD-DFT, the external potential of the interacting system that is modified under an applied field is treated by using the relation^{87,88}

$$\hat{V}_{ext}(\mathbf{r}, t) = \hat{V}_{ext,0}(\mathbf{r}) + \hat{V}_t f(t), \quad (2.26)$$

where the first and second terms correspond to the external potential at the ground state and under perturbation, respectively.^{87,88} The response of $\rho(\mathbf{r}, t)$ to the varying external potential is given by expanding $\rho(\mathbf{r}, t)$ in a Taylor series, which includes the sum between the ground-state electron density to the first order element $\rho_1(\mathbf{r}, t)$ in the linear-response TD-DFT, whereas the higher order terms are treated by other extensions of TD-DFT.^{87,88} Particularly,

$$\rho_1(\mathbf{r}, t) = \int_0^\infty dt' \int d^3\mathbf{r}' \chi_{KS}(\mathbf{r}t, \mathbf{r}'t') \delta v_{KS}(\mathbf{r}', t') \quad (2.27)$$

with χ_{KS} defining the density-density response function of a non-interacting system, i.e., the derivative of the electron-density $\rho_I(\mathbf{r},t)$ in respect to the KS potential $\delta v_{KS}(\mathbf{r}',t')$ given by ^{87,88}

$$\delta v_{KS} = \delta v_{ext}(\mathbf{r},t) + \int d^3\mathbf{r}' \frac{\rho_1}{|\mathbf{r}-\mathbf{r}'|}(\mathbf{r}',t) + \int d^3t' \int d^3\mathbf{r}' f_{xc}[\rho_{GS}](\mathbf{r}t, \mathbf{r}'t')\rho_1(\mathbf{r}',t'). \quad (2.28)$$

Thus, the excitation energies and the intensities expressed by the oscillator strengths are extracted from derivation of the linear response equations, as discussed by Nogueira *et al.* ^{87,88}

In this thesis, the excited-state properties in Papers II-IV were obtained at the B3LYP⁷⁴/6-311G** and M06⁷⁷/6-311G** levels of theory by considering the first twenty singlet excited states. These calculations were held in gas phase on Gaussian 09⁶³ and 16⁶⁴, which is sufficiently good to provide a qualitative description that is necessary for photocatalyst design. However, the environment and vibronic effects might be important to improve the concordance with the experimental data.⁸⁵

3. Molecular Modelling of Conjugated Polymers for Hydrogen Evolution

In Paper I, three novel polymeric nanostructured photocatalysts containing fluorene (F_L) moieties have their photocatalytic activity evaluated for hydrogen evolution reaction. The polymer dots were obtained via nanoprecipitation, a procedure that was initiated by solubilization in tetrahydrofuran solvent in presence of a surfactant. The mixtures were then submitted to sonication and filtration to generate the clear polymer dots in aqueous solution, i.e., F8T2 (**1**) (poly(9,9-dioctyl-fluorenyl-2,7-diyl)-*co*-bithiophene)), PFBT (**2**) (poly(9,9'-dioctyl-fluorenyl-2,7-diyl)-*co*-(1,4-benzo-2,1,3-thiadiazole)) and PFO-DT-BT (**3**) (poly(2,7-(9,9-dioctylfluorene)-*alt*-4,7-bis(thiophen-2-yl)benzo-2,1,3-thiadiazole)), with F_L units intercalating with thiophene (T) in (**1**) or benzothiadiazole (BT) in (**2**). In (**3**), T is regularly considered as a π -spacer connecting the electron-donating (D) fluorene moiety to benzothiadiazole, an electron-poor unit that exerts the role as acceptor (A). By using a two-component system with ascorbic acid as the sacrificial reagent and the nanophotocatalyst, our collaborators have found an initial rate of $50 \mu\text{mol g}^{-1} \cdot \text{h}^{-1}$ for (**3**), which is excellent compared to other organic photocatalysts, such as pyrene⁶⁰ or carbazole-based polymers.⁶¹ Motivated by these experimental findings, a theoretical investigation was carried out with *ab initio* methodology to unveil the factors leading to an enhanced performance exhibited by (**3**), whereas (**1**) does not show any activity for hydrogen production. In the follow-up work, we have investigated other D-A polymers regarding their ability to photocatalyze the hydrogen evolution reaction by evaluating optical and thermodynamic properties, as well as hydrogen and exciton binding energies as descriptors for photocatalytic efficiency. In Paper II, it is of particular interest the molecular systems based on benzothiadiazole-derivatives connected to a F_L -T donor region. In Paper III, the benzothiadiazole unit has been constrained for further evaluation of donor tailoring effects on the chemical properties that are important for the photocatalyst design.

3.1. Benchmark for Density Functional Theory Methods

To model the fluorene-derivative polymers, I have built up molecular structures with a varying number of 1-4 repeated monomeric units with symmetric

terminations determined by the fluorene unit, verifying the convergence for the frontier orbital energies and testing different functional/basis set combinations to have a *first* assessment of the outcomes from cyclic voltammetry measurements in Paper I and Sato *et al.*⁹⁰ Such energies are directly obtained via population analysis of the neutral polymer, a static-like calculation that does not capture the relaxation or thermal effects on the species internal energy upon electron transfer processes. In this sense, the proper assessment of the electrochemical process can be achieved by calculating the redox potentials via Gibbs free energies of reaction in solvated environment. This point will be addressed in the next sections, but the simplified methodology provides similar chemical trends to those obtained by using the Gibbs free energies, while being time efficient in a computational perspective.

The benchmark for level of theory has been performed for Group A polymers, i. e., F8T2 (**1**), PFBT (**2**) and PFO-DT-BT (**3**), providing the method of choice for further calculations. The general molecular representation for these materials can be visualized in Figure 3.1.

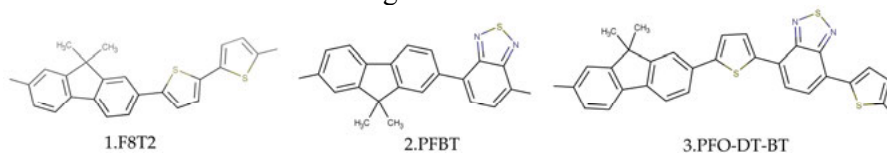


Figure 3.1- Molecular structures of fluorene-based polymers. The methyl groups have been added to replace the original long alkyl chains.

Table 3.1 shows the highest occupied molecular orbital energies (E_{HOMO}) that have been directly taken from the self-consistent calculations carried out in Gaussian 09. In the third column, the B3LYP/6-31G* level of theory is clearly inaccurate to reproduce the experimental results, with an absolute error ($\Delta\epsilon$) lying within the range of 0.39- 0.60 eV for these polymers. The larger basis set (6-311G**) that is presented in the nearest column brings an improvement on the determination of E_{HOMO} , particularly by using the monomeric models. In fact, this level of theory has been chosen for the theoretical calculations in Paper I in connection with its good predictability of thermodynamic properties that do not involve electron transfer processes.

In Paper II, the benchmark has been extended to other exchange-correlation functionals to account for weak long-range interactions such as CAM-B3LYP, M06, M06-2X and wB97x-D. The former functional shows inadequacy to predict orbital energies as E_{HOMO} is overestimated in absolute values, reaching an impressive $\Delta\epsilon= 0.88$ eV for monomeric (**3**). A similar conclusion has been obtained by McCormick *et al.*⁷⁵ in their comparative study involving different methodologies to estimate the orbital energies of polymeric compounds. For Minnesota functionals, the use of M06-2X results in a better estimative with an increasing alkyl chain. Nonetheless, M06 shows the best performance among all functional/basis sets combinations, with $E_{\text{HOMO}}=-5.39$, -5.75, -5.39

eV for **(1-3)** dimeric models, which gives a relative error in the range of 0.05-2.00% and $\Delta e=0.09-0.11$ eV.

A similar analysis regarding the lowest unoccupied molecular orbital (E_{LUMO}) is displayed in Table 3.2. These energies have been primarily taken from the self-consistent calculations, but it is well-known that the virtual orbitals are poorly described by standard density functional theory methods.⁷⁵ For instance, M06 fairly describes the qualitative results, but a significant relative error in the range 19.4 %- 18.3 % ($\Delta e= 0.51-0.99$ eV) has been found for these systems. By using the M06/6-311G** theory level, a small improvement could be obtained, with $E_{\text{LUMO}}=-1.99$, -2.51 and -2.74 eV for **(1-3)** polymers, respectively, but still far from a fair agreement. As reported elsewhere,^{75,91} in analogy to experimental LUMO determination using the optical band gap, the first excitation energies corresponding to an approximate HOMO \rightarrow LUMO transition (E_{opt}) can be added to E_{HOMO} such as

$$E_{\text{LUMO}}= E_{\text{HOMO}}(\text{SCF}) + E_{\text{opt}}(\text{TD-DFT}), \quad (3.1)$$

where E_{opt} is the energy gap obtained from TD-DFT calculations. In this sense, a significant improvement is verified by using M06 with a corrected energy gap (see Table 3.2, in parenthesis), with an average relative error of 5.0 % and $\Delta e = 0.07-0.32$ eV.

Table 3.1- Benchmark for different functional/basis set combinations to determine E_{HOMO} in Gaussian 09. The experimental values obtained from the literature are displayed in the last column. Adapted with permission from Damas *et al.*,⁹² Copyright (2018) American Chemical Society.

| Polymer | Number of units | B3LYP 6-31G* | B3LYP 6-311G** | M062X 6-31G* | M06 6-311G** | CAM- B3LYP 6-31G* | wB97x-D 6-31G* | Exp. |
|-----------|--------------------|-----------------|-------------------|-----------------|-----------------|-------------------------|-------------------|---------------------|
| HOMO (eV) | | | | | | | | |
| F8T2 | (1) | - | -5.400 | - | - | - | - | - |
| | (2) | -4.899 | -5.180 | -6.145 | -5.390 | - | - | -5.50 ⁹⁰ |
| | (3) | -4.842 | -5.110 | -5.829 | - | - | - | - |
| | (4) | - | - | - | - | - | - | - |
| PFBT | (1) | - | -5.840 | - | - | - | - | - |
| | (2) | -5.328 | -5.570 | -6.542 | -5.749 | - | - | -5.78 ⁸ |
| | (3) | -5.243 | -5.520 | -6.452 | - | - | - | - |
| PFO-DT-BT | (1) | -5.093 | -5.330 | -6.338 | - | -6.359 | - | - |
| | (2) | -4.932 | -5.170 | -6.159 | -5.390 | -6.182 | -6.978 | -5.48 ⁸ |
| | (3) | -4.892 | -5.130 | -6.122 | - | -6.139 | - | - |
| | (4) | -4.878 | - | -6.092 | - | -6.123 | - | - |

Table 3.2 - Benchmark for different functional/basis set combinations to determine E_{LUMO} in Gaussian 09. All energies correspond to direct output from SCF calculations, except for the values in parenthesis, where the TD-DFT gap has been used for correction. The experimental values obtained from the literature are displayed in the last column. Adapted with permission from Damas *et al.*⁹² Copyright (2018) American Chemical Society.

| Polymer | Number of units | B3LYP 6-31G* | B3LYP 6-311G** | M062X 6-31G* | M06 6-311G** | CAM- B3LYP 6-31G* | wB97x-D 6-31G* | Exp. |
|-----------|--------------------|-----------------|-------------------|-----------------|--------------------|-------------------------|-------------------|---------------------|
| LUMO (eV) | | | | | | | | |
| F8T2 | (1) | - | -1.790 | - | - | - | - | - |
| | (2) | -1.877 | -2.080 | -1.071 | -1.990 (-2.672) | - | - | -2.50 ⁹⁰ |
| | (3) | -1.967 | -2.180 | -1.530 | - | - | - | - |
| | (4) | - | - | - | - | - | - | - |
| PFBT | (1) | - | -2.570 | - | - | - | - | - |
| | (2) | -2.438 | -2.660 | -1.603 | -2.510 (-3.180) | - | - | -3.50 ⁸ |
| | (3) | -2.478 | -2.630 | -1.657 | - | - | - | - |
| | (4) | - | - | - | - | - | - | - |
| PFO-DT-BT | (1) | -2.611 | -2.830 | -1.811 | - | -1.504 | - | - |
| | (2) | -2.677 | -2.900 | -1.899 | -2.740 (-3.330) | -1.568 | -1.170 | -3.40 ⁸ |
| | (3) | -2.710 | -2.930 | -1.918 | - | -1.602 | - | - |
| | (4) | -2.724 | - | -1.953 | - | -1.614 | - | - |

Therefore, M06 is the most suitable method to describe the properties of interest in Papers II-III, where a two-unit symmetric model have been employed to represent the polymers under investigation. As displayed in Figure 3.2, the symmetric model is appropriate since different terminations lead to anomalies in the structure, including different torsional angles between similar units throughout the molecule.

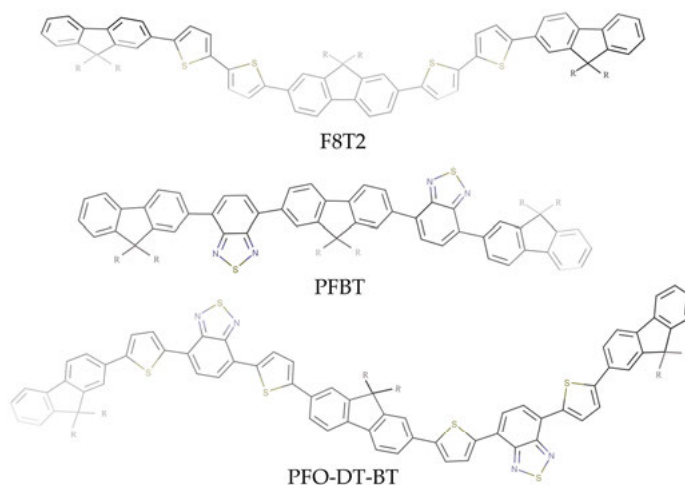


Figure 3.2- Symmetric dimer models built for the different polymer classes under investigation. R indicates the replacement of the original long alkyl chains by methyl groups.

3.2. On the Effects of D-A Architecture and π -spacer

In this section, I consider the first group of polymeric materials studied in this work (**1-3**). As previously mentioned, a two-unit model with symmetric terminations has been chosen to represent the molecular structure of these materials that have been synthesized as nanoparticles (see Paper I). Based on early experience, a helical structure was used as starting point for the optimization carried out in Gaussian 09.

Figure 3.3 displays the main torsional angles between chemical units in the simplified monomeric models for (**1-3**) polymers. F8T2 (**1**) has a non-planar structure with a substantial torsional angle between fluorene-thiophene units ($\theta_1 = 26.8^\circ$). Furthermore, this polymer has no photocatalytic activity for hydrogen production that is partially associated with its high energy gap ($E_g = 2.72$ eV). In general, it is well disseminated the idea that a more-planar configuration enhances the π -electron distribution over the polymer backbone to promote a decrease in E_g . However, we can verify a somewhat different behavior in this polymer group, where a substantial decrease in E_g is not necessarily accompanied by an improvement of the structural planarity. For instance, (**2**) has calculated $E_g = 2.57$ eV while exhibiting $\theta_3 = 39.0^\circ$. On the other

hand, the insertion of a thiophene unit between fluorene-benzothiadiazole units in **(3)** is indeed followed by reduction in the torsional angle between the donor-acceptor region ($\theta_4 = 11.6^\circ$), which leads to a local planar configuration that can be associated with the decrease in $E_g = 2.06$ eV.

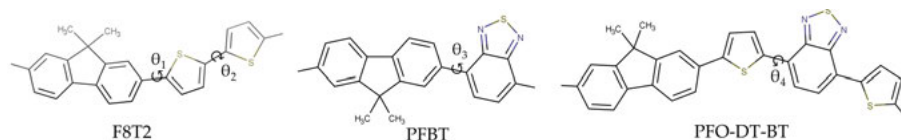


Figure 3.3- Group A molecular structures along with the torsional angles between chemical units (θ_1 - θ_4).

The total and partial density of states for **(1)** and **(3)** polymers give an interesting insight into the orbital composition around the frontier orbital region, as displayed in Figure 3.4. It is important to highlight that the virtual orbitals are shown with a small displacement in accordance with the theoretical optical gaps. For Group A polymers, the highest occupied molecular orbital does not exhibit a well-defined peak due to the superposition with other deep-lying states. This indicates that this orbital is distributed over the molecule (see Figure 3.5), despite of the high torsional angles between units, with major contributions from F_L and T units. In fact, the latter units contribute in a higher extension for both **(1)** and **(3)**, with respective $\sim 56\%$ and $\sim 46\%$. Thus, these findings suggest that thiophene units do not act merely as a π -system that improves the conjugation length, but have an electron-donating character along with fluorene units for these polymeric systems. In fact, this moiety has been previously reported as an electron-donor unit when linked to benzothiadiazole⁹³ or as a π -bridge in a D- π -A structure.^{94,95} From this point, this moiety is solely referred as an electron-donating or donor unit.

Above the energy gap, the first unoccupied orbital peak is partially mixed with higher energy states in **(1)**, showing predominant contribution from T ($\sim 49\%$) that is followed by F_L units ($\sim 40\%$). By substituting T for the well-known strong acceptor BT in **(2)**, the LUMO is significantly moved towards lower energies while presenting a localized peak composed in $\sim 81\%$ by BT, with details available in Paper II. This percentage is reduced to around 67% in **(3)** when introducing an extra donor unit (thiophene), but there is a displacement towards lower energies that leads to a reduced energy gap. The spatial orbital distribution shows a clear electronic density localization at the BT sites, as depicted in Figure 3.5- bottom.

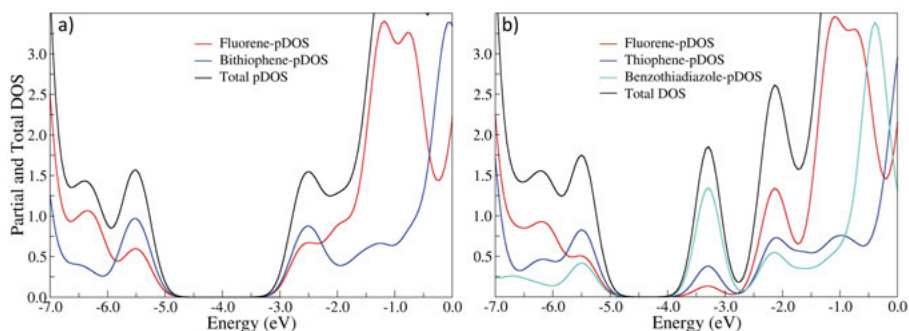


Figure 3.4- Total and partial density of states for a) F8T2, b) PFO-DT-BT. The virtual orbitals are slightly shifted to meet the TD-DFT predictions for the energy gap. Adapted with permission from Damas *et al.*⁹² Copyright (2018) American Chemical Society.

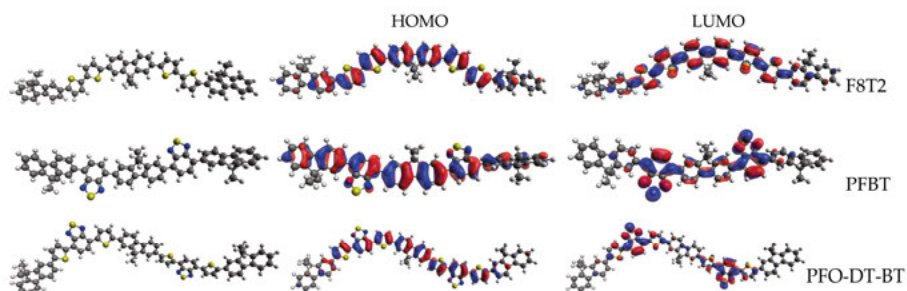


Figure 3.5- Spatial distribution of frontier orbitals for Group A polymers within the isovalue 0.02. Level of theory: M06/6-311G**. Reprinted with permission from Damas *et al.*⁹² Copyright (2018) American Chemical Society.

3.3. Replacing the Benzothiadiazole Moiety by its Derivatives or other Acceptor Units

In Paper II, the replacement of the benzothiadiazole unit in **(3)** by its derivatives is evaluated on the electronic properties and absorption range of the resulting polymeric materials (see Figure 3.6). To facilitate the discussion, these systems are separated in three groups: in Group B (**4-6**), the acceptor unit has been functionalized by fluorine, cyano or methoxy groups; in Group C (**7-8**), the sulfur atom at the thiadiazole subunit has been replaced by nitrogen or selenium atom in the benzotriazole (BTr)- or benzolediazole (Sed)-based polymer, respectively; in Group D (**9-10**), a fused ring given by hybrid benzo(triazole-thiadiazole) is considered as the acceptor unit.

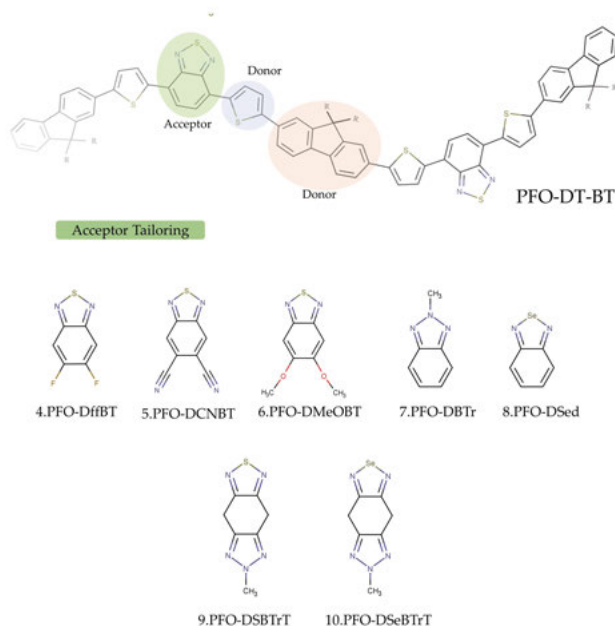


Figure 3.6- Structural formula of the reference polymer PFO-DT-BT (**3**) along with the acceptor units under investigation in Paper II. In detail, the final polymer name is written under each acceptor unit.

The helical conformation previously determined for (**3**) has been used as the starting point for geometry optimization of Group B-D polymers. Most final molecular structures are characterized by having symmetric thiophene (T) groups with sulfur atoms oriented towards the benzene ring. The exception is (**5**), where an inversion in such orientation reduces the electrostatic repulsion between cyano groups and sulfur atoms, stabilizing the structure by 0.14 eV while lowering θ_4 from 35.5° to 30.2°. In general, all systems show little variation for θ_1 (3.3°) in comparison to (**3**), but an interesting impact on the chain conformation is seen by functionalizing the 5,6 positions of the BT unit. Likewise, the replacement of sulfur atoms at the thiadiazole ring and hybrid benzo(triazole-thiadiazole)-derived units implicate in a slight variation of torsional angles between T and the benzothiadiazole-derivative unit (θ_4) while E_g is substantially altered for these materials. In particular, the fluorination in (**4**) implies in a low value for $\theta_4 = 1.3^\circ$ that is not necessarily correlated with its high energy gap ($E_g = 2.11$ eV), an effect that is also verified for (**7**). Thus, these findings strongly suggest the lack of direct correlation between the polymer stability that is given by E_g and the extension of the π -conjugation length in Group C. In Group D, a significant decrease in $E_g = 1.30$ eV for (**10**) is clearly related to a more effective π -conjugation expressed by the torsional angle ($\theta_4 = 1.9^\circ$).

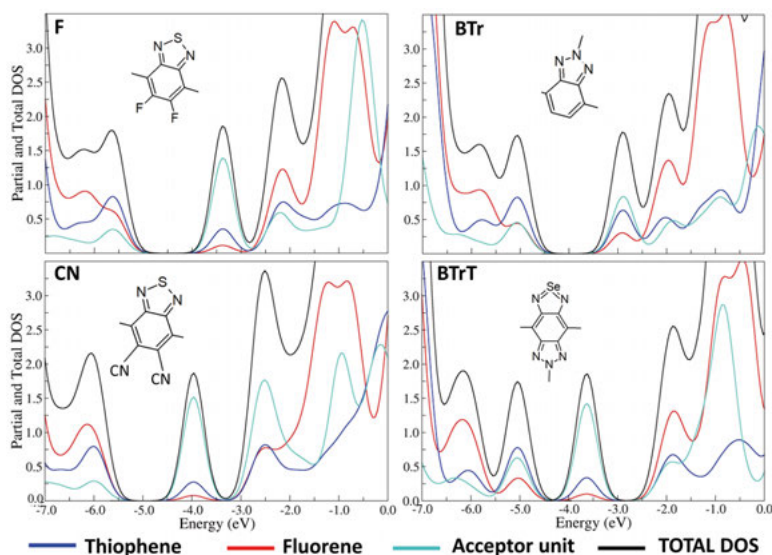


Figure 3.7- Total and partial density of states calculated for fluorene-thiophene based polymers with a varying acceptor unit. Adapted with permission from Damas *et al.*⁹² Copyright (2018) American Chemical Society.

In Figure 3.7, the total and partial density of states are given for each polymer from Groups B-D at the range -7.0 to 0 eV. Accordingly, the highest occupied molecular orbital of these polymers has a π -bonding character, being mainly composed by T rings (around 40-46%), followed by a wide range of F_L (16-39%) and BT-derived (3.8%-32%) contributions. In particular, the HOMO from the cyano-functionalized polymer (**5**) has the highest fluorene character (39%), along with a low percentage from BT units (4%). For benzo(triazole-thiadiazole) (BTrT)-based polymers (**9-10**), the contribution from the BT rings reaches 32%, specially from the HOMO- n orbitals with $n=0$ and 1. Therefore, these materials exhibit π -electron delocalization that results in a well-distributed orbital over the polymer backbone, as discussed for the D-A polymers in the previous section. Another important point is the electron-donating character exhibited by thiophene units, as evidenced by the significant contribution from these moieties to form the first HOMO- n orbitals. Most systems have a defined peak describing the first LUMO+ n orbitals, whose composition is dominated by the acceptor units in (69-80%) in their respective groups. The thiophene units have 10-17% of participation in such energy levels, revealing as the second most important units for these electronic states. Nonetheless, (**7**) has an overall delocalized LUMO with dominant benzotriazole character (39%), but also showing participation from T (32%) and F_L (15%) rings.

3.4. Donor Tailoring in Benzothiadiazole-based Polymers

In Paper III, we have performed an extensive evaluation of benzothiadiazole-based polymers with a varying donor region that is defined by two types of electron-rich moieties: Donor I, i. e, fluorene (F_L or PFO), cyclopentadithiophene (CPT), methoxybenzodithiophene (O-BzT), thiophenebenzodithiophene (T-BzT) and Donor II, a thiophene-(T, VT) or thienethiophene-(TT, VTT) based unit that acts a π -spacer in these systems. All combinations are depicted in Figure 3.8.

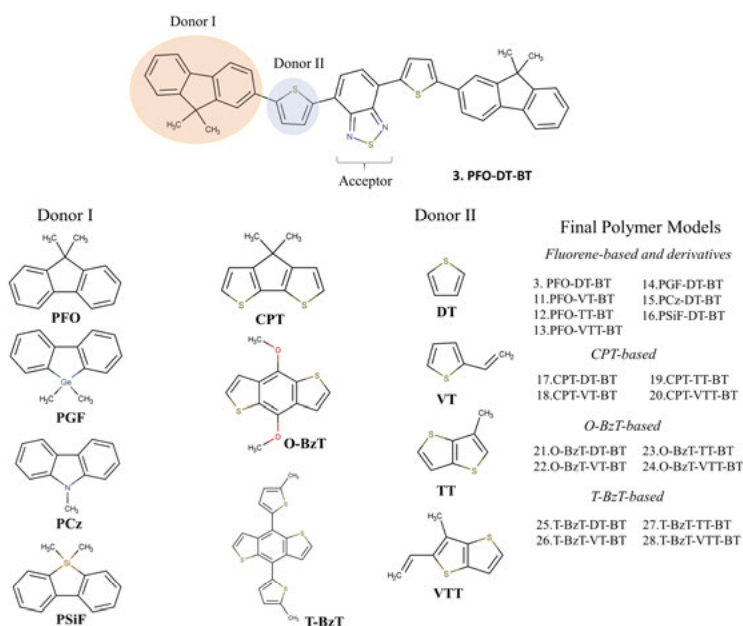


Figure 3.8- Benzothiadiazole-based polymers with a varying donor region. Reprinted with permission from Damas *et al.*¹⁹ Copyright (2019) American Chemical Society.

3.5. The Photocatalytic Process

As it well-known in general sciences, the terrestrial solar spectrum has 40% of its composition by visible light extending from 400-700 nm, while 8% is composed by ultraviolet light (200-400 nm).⁹⁶ Thus, it is presumably important for the applicability of a photocatalyst in solar water splitting to be active in this region. At this interval, the photon energy is absorbed by the molecule to promote an internal electronic transition between molecular orbitals, although vibrational and rotational transitions are expected to take place at the same time.⁹⁷ During this process, a positive charge region is left behind in the occupied states, also referred as a hole in the solid-state terminology.

Both charge carriers are initially bound to each other by a certain amount of energy to form an excitonic state, which could lead to a decrease in photocatalytic efficiency due to charge recombination process.⁹⁸ This step is represented by I in Figure 3.9, where P^* stands for the polymeric system containing an excitonic state. To deal with the abovementioned problem, the so-called electron-hole pair must be separated by removing either charge carrier. In Figure 3.9 (left-hand side), the hole is consumed by using a sacrificial agent or donor (D/D^+) that is followed by the electron transfer to carry out the hydrogen evolution reaction (HER).^{60,99,100} If the polymeric system has a high pK_a that assures the protonation takes place right after the photoexcitation, it will be the electron the charge carrier that is first consumed (Step IIa). The initial photocatalyst is then recovered after hole transfer to the sacrificial agent (Step IIIa).

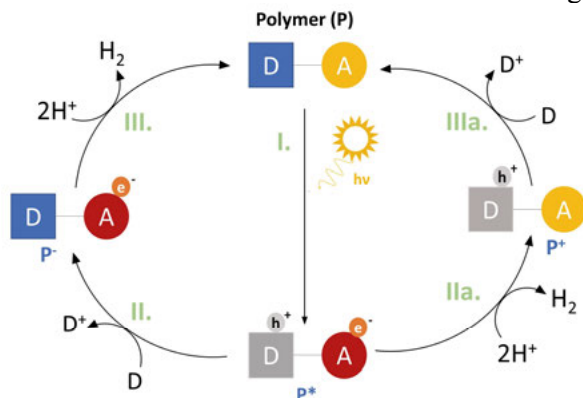


Figure 3.9- General representation of the hydrogen evolution reaction photocatalyzed by conjugated polymers in presence of a sacrificial agent. Reprinted with permission from Damas *et al.*¹⁹ Copyright (2019) American Chemical Society.

In Figure 3.9, the left pathway (Steps II and III) can be represented by the potentials of the redox pairs (P^*/P^-) and (P/P^-), as shown in Equations 3.2 and 3.3, respectively:^{36–38}



and



In this sense, the electron affinity of a molecular system, as well as the energy of its lowest unoccupied molecular orbital (E_{LUMO}) have a close relation to the potential of the redox pair (P/P^-).^{101,102} Nonetheless, the latter carries information about enthalpic and entropic contributions that are expected to affect the internal energy of a neutral system upon reduction, whereas the electron affinity is defined as the enthalpy energy associated with this process.^{92,42,57,58} Finally, the orbital energy is an eigenvalue obtained via diagonalization of the

Kohn-Sham equations, therefore being a static value that is related to the electronic energy of the system.

In Figure 3.9, the right pathway is denoted by the potentials of redox pairs (P^+/P^*) and (P^+/P), as shown by the electrochemical reactions:



and



Similar to the aforementioned discussion, the potential of the redox pair (P^+/P) is usually associated to the ionization potential and E_{HOMO} .¹⁰¹ It is important to highlight that this nomenclature may exhibit some variations regarding the species order or the acronym that is more appropriate for small-molecules (SM) or the sacrificial agent (D^+/D) in Papers II-IV.

3.5.1. Optical Properties: Group A Polymers

In Paper I, the ability of Group A polymers (**1-3**) to absorb light has been verified through UV-spectroscopy by our collaborators, with experimental absorption spectra displayed in Figure 3.10 (a). Comparatively, the theoretical predictions for the main absorption peaks are shown in the bottom, along with the absorbance intensities as adjusted with their oscillator strength (f). The detailed information on the main electronic transitions is given in Table 3.3.

To verify the disparity concerning the absorption range of these UV/Vis theoretical spectra in the wavelength (λ) range between 300-1000 nm, the λ difference between the first and the last transitions having $f > 0.2$ is defined as the absorption range (Δb). The polymer (**1**) presents the lowest value for $\Delta b = 182.18$ nm, a parameter that is not altered by introducing the benzothiadiazole unit in (**2**). However, the acceptor unit promotes a separation between the main peaks that is 49.69 nm higher compared to (**1**). This separation is increased by adding the thiophene unit in (**3**) along with an improvement in the absorption range ($\Delta b = 273.2$ nm). In this case, this is associated with the polymer stabilization by extending the π -conjugation length and reducing the torsional angle between T and BT units (11.6°).

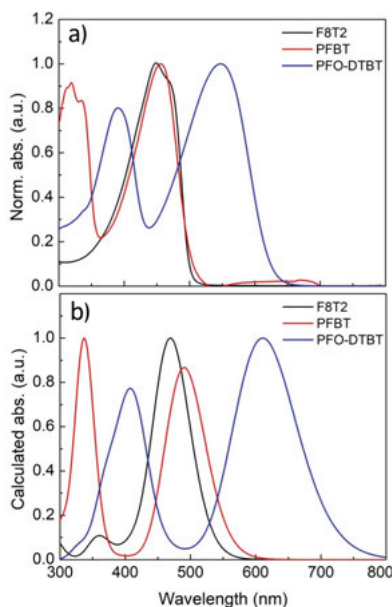


Figure 3.10- UV-Vis spectra of Group A polymers (a) and theoretical predictions as obtained from TD-DFT calculations (b). Level of theory: M06/6-311G.** Reprinted with permission from Damas *et al.*⁹² Copyright (2018) American Chemical Society.

Now considering the nature of each excitation, F8T2 ($S_0 \rightarrow S_1$) has the first maximum at $\lambda_{\text{max}} = 455.80$ nm, whereas the last transition with $f > 0.02$ occurs at $\lambda = 273.62$ nm. The former transition has predominant contribution from the HOMO \rightarrow LUMO transition (86%). Hence, all excitations in this polymer are originated from a π -binding to a more energetic π -antibonding molecular orbital, being both of them fairly distributed over the molecule in the first twenty singlet excited states. This kind of excitation is commonly referred as a π - π^* transition.

In **(2)** and **(3)**, 3-4 electronic transitions are characterized by excitations between widely distributed HOMO, whereas LUMO+ n orbitals exhibit high localization at the BT units. Therefore, these electronic transition has a charge transfer character that is usually associated with an improvement in the charge separation processes in organic solar cells and photocatalytic hydrogen production.²³ In both polymers, the UV-Vis absorption spectra have a double-peak shape that is typical for donor-acceptor (or similarly, D- π -A) polymers,^{104–110} whereas the first peak is found to be red-shifted to 481.98 nm and 600.58 nm, respectively. Similar to **(1)**, the second absorption maximum for **(2)** and **(3)** are intramolecular π - π^* transitions. Jespersen *et al.*¹⁰⁵ have found similar results regarding the orbital localization and transition nature of these materials in a study employing the semi-empirical method (ZINDO) to describe the UV/Vis spectrum from **(2)** and **(3)**.¹⁰⁵

Table 3.3 - Optical properties obtained at the range 300-1000 nm with TD-DFT calculations. In the last column, nCT is the number of charge transfer transitions with $f > 0.02$. Adapted with permission from Damas *et al.*⁹² Copyright (2018) American Chemical Society.

| Group A | λ (nm) | Character | f | Major Contributions | nCT |
|-----------|-------------------------|-------------------------|-------|-----------------------------|-----|
| F8T2 | S ₁ :455.80 | $\pi \rightarrow \pi^*$ | 3.262 | H \rightarrow L (86%) | 0 |
| | S ₄ :353.60 | $\pi \rightarrow \pi^*$ | 0.331 | H-1 \rightarrow L+1 (71%) | |
| | S ₂₀ :273.62 | $\pi \rightarrow \pi^*$ | 0.020 | H-4 \rightarrow L (38%) | |
| PFBT | S ₁ :481.98 | CT | 1.382 | H \rightarrow L (87%) | 3 |
| | S ₇ :330.09 | $\pi \rightarrow \pi^*$ | 1.593 | H \rightarrow L+2 (85%) | |
| | S ₁₅ :297.56 | $\pi \rightarrow \pi^*$ | 0.220 | H \rightarrow L+4 (52%) | |
| PFO-DT-BT | S ₁ :600.58 | CT | 2.220 | H \rightarrow L (76%) | 4 |
| | S ₇ :404.76 | $\pi \rightarrow \pi^*$ | 1.610 | H \rightarrow L+2 (80%) | |
| | S ₁₆ :327.38 | $\pi \rightarrow \pi^*$ | 0.108 | H-1 \rightarrow L+3 (50%) | |

3.5.2. Optical Properties: Acceptor Tailoring

All theoretical UV/Vis spectra for Group B-D polymers can be visualized in Figure 3.11 (a), where the dashed-line representation for **(3)** is intended to facilitate further comparisons. In Figure 3.11 (b), the calculated λ_{\max} exhibit linear correlation to their respective experimental values, showing a low mean absolute error (MAE=35.48 nm) that indicates a very good accuracy for the theoretical assessment.

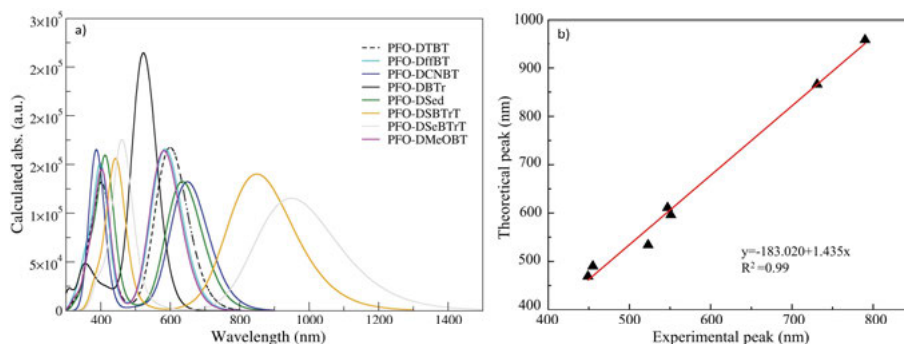


Figure 3.11- a) Theoretical UV-Vis spectra and b) Correlation between theoretical and experimental absorbance for polymers from Groups B-D. The linear equation is given by $y = -183.020 + 1.435x$. Reprinted with permission from Damas *et al.*⁹² Copyright (2018) American Chemical Society.

As seen in Figure 3.11 (a), most polymers have a UV/Vis absorption spectrum represented by a double-peak shape, while exhibiting an average $\Delta b = 274.1$ nm. Clearly, the introduction of BTrT units in their derivatives dramatically enhances the absorption range to reach $\Delta b = 557.74$ nm in **(10)**. As a comparison, the narrowest UV/Vis spectrum that is displayed by **(7)** ($\Delta b = 217.73$ nm) has a similar form to F8T2 **(1)**, an electron-donating polymer with poor photocatalytic activity for hydrogen production. In Paper II, we have discussed the attribution of λ_{max} to the HOMO \rightarrow LUMO transition for F8T2, PFBT and PFO-DT-BT. This transition is also responsible for λ_{max} of BT-derivatives, showing a charge transfer character for those polymers **(4-6, 8-10)** due to the localized nature of LUMO. In general, λ_{max} peaks were found red-shifted in the order BTr < MeO < F < Sed < CN < SBTrT < SeBTrT units. In particular, **(10)** exhibits the highest displacement towards lower energies ($\Delta\lambda = 350$ nm), with an absorption peak ($\lambda_{\text{max}} = 950.5$ nm) that lies very close to the infrared region edge. It is also interesting to notice that the number of charge-transfer transitions increases from nCT=5 (for **3**) to nCT=8 for **(10)**, an indication that the electron density is concentrated at the acceptor unit upon photoexcitation at different λ . Therefore, this factor might positively impact the photocatalytic efficiency of this material in comparison with the reference polymer **(3)**.

3.5.3. Optical Properties and Electronic Structure: Donor Tailoring

The UV/Vis fingerprints of selected benzothiadiazole-based polymers upon structural modifications at the donor units can be visualized in Figure 3.12. As expected, their absorption spectra present a double-peak shape that is typical for polymeric materials with a donor-acceptor architecture, although some systems also present a third peak with high intensity at lower λ . Their main absorption peaks ($\lambda_{\text{max}} = 609.61 - 767.41$ nm) exhibit a red-shift displacement of $\Delta\lambda = 9.0 - 166.8$ nm upon comparison with **(3)**. In this sense, the upper limit is achieved by combining the chemical units with higher $\Delta\lambda$, i. e., CPT and VTT units in CPT-VTT-BT **(20)**. This is still a weaker effect than that verified upon acceptor tailoring in Paper II, where a red-shift of about $\Delta\lambda_{\text{max}} = 349.9$ nm has been shown by the BTrT-unit in a fluorene-thiophene-based polymer.

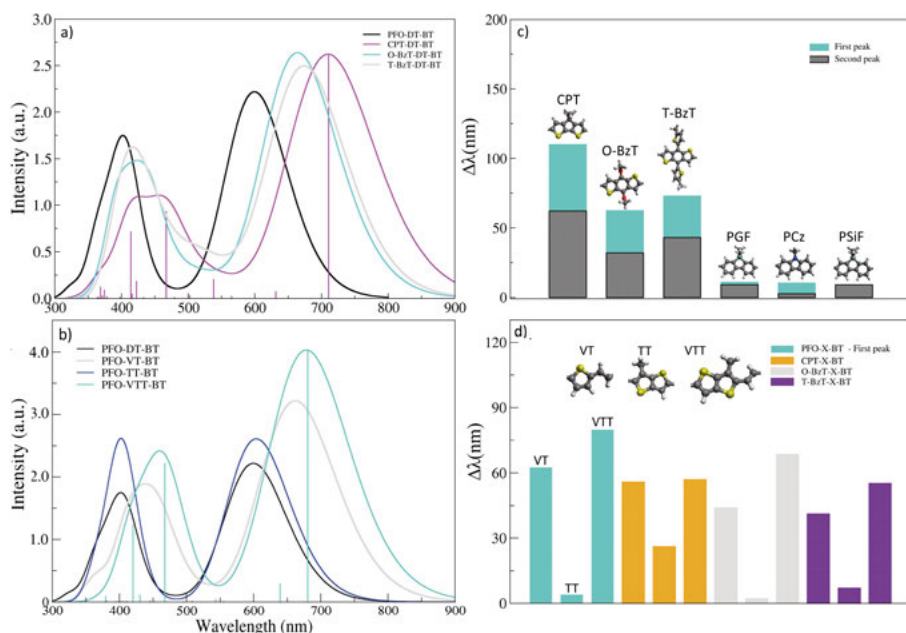


Figure 3.12- Donor tailoring effects on the (a,b) UV/Vis absorption Spectra of benzothiadiazole-based polymers and (c,d) $\Delta\lambda$ (in nm) of the main peaks compared to Donor I-DT-BT at the M06/6-311G (d,p) level of theory. Reprinted with permission from Damas *et al.*¹⁹ Copyright (2019) American Chemical Society.

The highest absorption peak has predominant contributions given by HOMO \rightarrow LUMO (67-87%), whereas the weaker peak is mainly associated with HOMO \rightarrow LUMO+2 (29-87%). The former electronic transition presents a charge-transfer character in benzothiadiazole-based polymers. As previously mentioned, this is associated with the localized nature of the first unoccupied orbital at the BT unit, which remains unaltered upon structural modifications at the donor region. As depicted in Figure 3.13, N2p and S2p orbitals from the BT unit have the major contributions to the first unoccupied orbital, being followed by C2p and S2p orbitals from the donor units in a much lower extent. In this sense, the HOMO is mainly composed by the Csp² atoms that form the π -conjugated system, with almost insignificant contributions from other atoms. It is also interesting to notice that O2p or S2p orbitals from the donor units do not compose HOMO, but they do contribute for a shift downwards of the first HOMO-*n* orbitals.

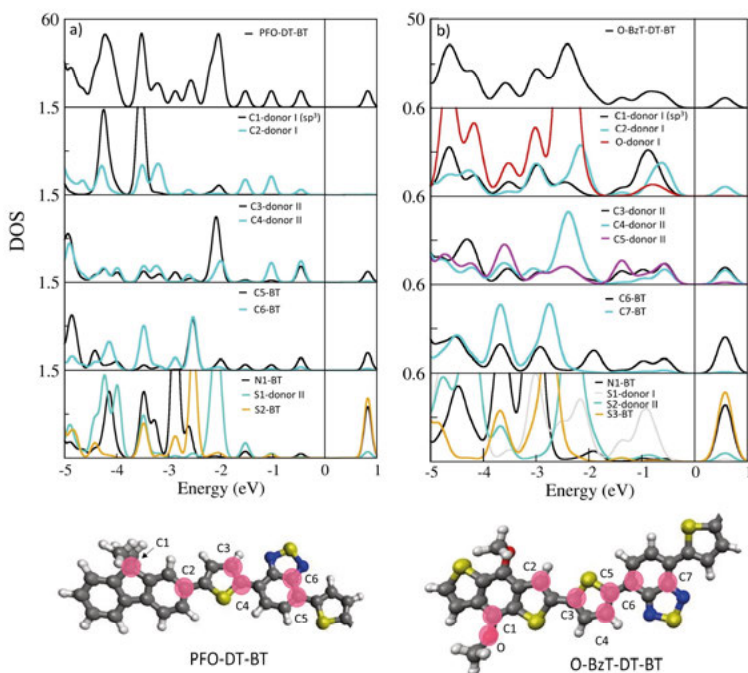


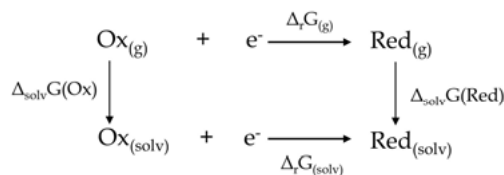
Figure 3.13- Partial density of states for some thiophene-benzothiadiazole-based systems with varying Donor I unit. Level of theory: PBE, 400 eV/Vasp code. Adapted with permission from Damas *et al.*¹⁹ Copyright (2019) American Chemical Society.

3.6. Theoretical Assessment of Redox Potentials

To compute the potentials of redox pairs (P^*/P^-), (P^+/P), (P^+/P^*) and (P/P^-), we have employed the thermodynamic relation between the standard redox potential ϕ and the Gibbs free energies variations $\Delta G_{(solv)}$ of the reduction processes once described by Equations 3.2-3.5:

$$\phi = - \frac{\Delta_r G_{(solv)}(Red)}{nF}, \quad (3.6)$$

where F is the Faraday constant ($23.06 \text{ kcal mol}^{-1} \text{ V}^{-1}$) and n corresponds to the number of electrons that are involved in the reduction process. The Gibbs free energies of reaction $\Delta_r G_{(solv)}$ should be calculated in solvated environment for further description of polarization effects on the ionic species. These calculations can be carried out in a direct approach involving relaxation steps in the solvent medium, but it is the Born-Haber thermodynamic cycle (see Scheme 3.1)^{111,112} the method of choice in Papers I-V and VII. This approach involves the calculation of free Gibbs energies of the reduction in gas phase $\Delta_r G_{(g)}$, but the Gibbs energies of each species in solvated environment is taken as a single-point calculation, which is particularly advantageous for the solid-state modelling (Paper V).¹¹³



Scheme 3.1- Born-Haber thermodynamic cycle for calculation of free Gibbs energy of reaction in solvated environment.

In Scheme 3.1,

$$\Delta_r G_{(\text{solv})}(\text{Red}) = \Delta_r G_{(g)}(\text{Red}) + \Delta G_{(\text{solv})}(\text{Red}) - \Delta G_{(\text{solv})}(\text{Ox}), \quad (3.7)$$

where

$$\Delta_r G_{(g)}(\text{Red}) = \Delta U_{(g)}(\text{Red}) + PV - T\Delta S_{(g)}(\text{Red}). \quad (3.8)$$

In Equation 3.7, $\Delta G_{(\text{solv})}$ is the solvation energy from the oxidized (Ox) or reduced (Red) species, as obtained using the polarizable continuum model (PCM)¹¹⁴ to reproduce the dielectric constant of the medium, i. e., water ($\epsilon=78.35$),⁶³ 1-bromooctane ($\epsilon=5.02$) or acetonitrile ($\epsilon=35.69$). In Equation 3.8, variations in internal energy and entropy are described by the terms $\Delta U_{(g)}$ and $\Delta S_{(g)}$, respectively. The Gibbs free energy of each component is estimated as¹¹⁵

$$G_{(g)} = E_{\text{elet}} + E_{\text{ZPE}} + (U_{\text{vib}} + U_{\text{trans}} + U_{\text{rot}}) + PV - T(S_{\text{vib}} + S_{\text{trans}} + S_{\text{rot}}), \quad (3.9)$$

with a total enthalpic contribution given by the sum between the total-energy (E_{elet}), the zero-point correction (E_{ZPE}), the pression-volume term and the thermal corrections ($U_{\text{vib}} + U_{\text{trans}} + U_{\text{rot}}$) to the internal energy. Similarly, the total entropy ($S_{\text{vib}} + S_{\text{trans}} + S_{\text{rot}}$) is multiplied by the temperature T to express the entropic contribution.¹¹⁵

To calculate the potentials of redox pairs (P^+/P^*) and (P^*/P^-), the polymer species (P^*) has been optimized in the first excited state within the TD-DFT approach by employing stepwise calculations within M06/6-31G(d) and 6-311G(d,p) levels of theory, as used for the other cases. Furthermore, the excited state optical gap has been added to the electronic energy of P^* to compose $\Delta_r G_{(\text{solv})}$ in a proper way.

3.6.1. Modelling the Hydrogen Evolution Reaction

The overall reaction to form molecular hydrogen is a well-known process described as¹¹⁶



To generate molecular hydrogen, the hydrogen atom is first bound to the catalytic center as a result of a proton-coupled electron transfer, further forming the intermediate state $H_{(ad)}^*$, as indicated by the reaction



In Equation 3.11, the asterisk corresponds to the catalytic site from the polymer, i.e., nitrogen, sulfur, oxygen and selenium atoms. The strength on the hydrogen-copolymer chemical bond has been evaluated by computing the hydrogen binding free energy ΔG_H , also reported as an important descriptor for the process.¹⁶ In this sense, a high positive ΔG_H indicates poor hydrogen bonding ability, whereas too negative values do not favor the hydrogen release. Therefore, a good catalyst is expected to have a hydrogen binding free energy lying between these limits, while as close as possible from the ideal condition ($\Delta G_H=0$).¹⁶

The procedure to calculate the descriptor ΔG_H consists basically of obtaining the thermal corrections to the electronic energy, which has been attained by submitting the molecular structures to the frequency calculations at the ground-state after the optimization step. The hydrogen binding free energy in gas phase is then calculated through the relation⁸

$$\Delta G_{H(g)} = G_{(P-H)} - G_{(P)} - 1/2 G_{(H_2)} \quad (3.12)$$

where the first term gives the Gibbs free energy of the hydrogenated polymeric system and the second and third terms represent the free energies of the pristine polymer and hydrogen molecule, respectively. Solvation effects on $\Delta G_{H(g)}$ have also been evaluated by using the Born-Haber thermodynamic cycle described in Scheme 3.1. In Papers I-II, water was the solvent of choice for the theoretical predictions, based on its use in the experimental measurements. In Paper III, the analysis was extended to 1-bromooctane and acetonitrile.

Conjugated polymers acting as photocatalysts for hydrogen production should also present favorable thermodynamic driving force to promote the reduction reaction described in Equation 3.10, a quantity often called as catalytic power, i. e.:

$$\Delta G = \left| \phi_{P/P^-} - \phi_{H^+/H_2} \right|, \quad (3.13)$$

or, equivalently,

$$\Delta G = \left| \phi_{P^+/P^*} - \phi_{H^+/H_2} \right|, \quad (3.14)$$

where ϕ_{P/P^-} and ϕ_{P^+/P^*} correspond to the potential of redox pairs (P/P^-) and (P^+/P^*), respectively. In Papers II-III, we have used the proton reduction potential in standard conditions ($\phi_{H^+/H_2} = 4.44$ V).¹⁵

3.6.2. Thermodynamic Driving Force for Charge Transfer: Acceptor Tailoring

In Section 3.1, I have started the discussion about how approximating the potentials of redox pairs (P/P^+) and (P^+/P) to the frontier orbital energies can be misleading even using experimental optical gaps to correct E_{LUMO} . Here, I present a qualitative comparison between both methods to estimate the thermodynamic driving force (ΔG) for electron transfer processes in fluorene-based polymers, which is shown in Figure 3.14. General trends for Group A (**1-3**) remain unaffected by the methodology, but other Groups (B-D) exhibit slight variations that are found important for photocatalytic design purposes. All polymers exhibit suitable ΔG to promote the proton reduction, as well as $\phi_{P^+/P}$ or E_{HOMO} lying sufficiently low for further reduction by a sacrificial agent.

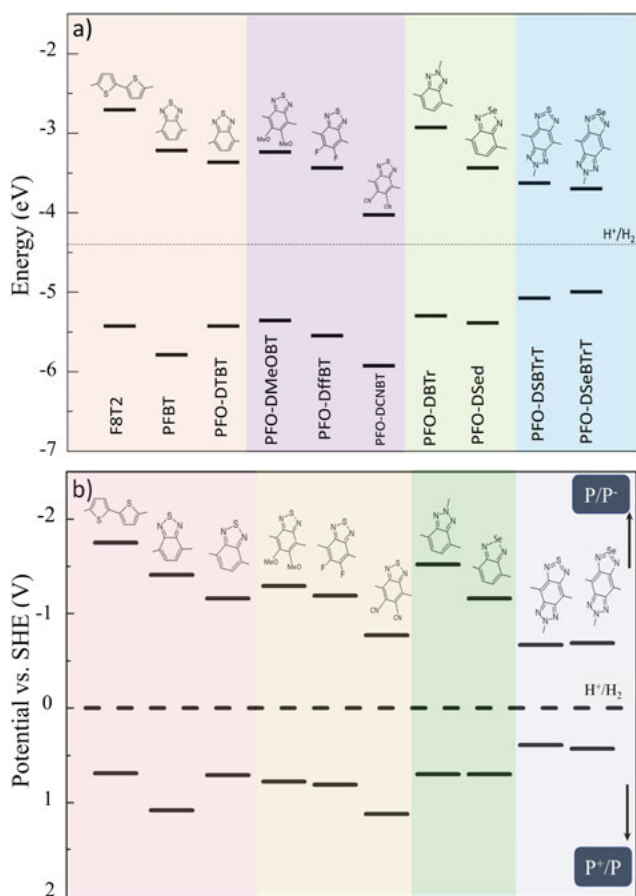


Figure 3.14- a) Diagram of energy levels for fluorene-based polymers containing different acceptor entities and b) potentials of redox pairs (P/P^+) and (P^+/P). The proton reduction energy is defined at pH=0 with -4.40 eV (a) or 4.40 V (b). Adapted with permission from Damas et al.⁹² Copyright (2018) American Chemical Society.

An interesting feature is revealed by using the Hammett parameter (σ_p)¹¹⁷ to quantify empirically the substituent effect in Group B polymers (4-6). In this sense, an increase in the withdrawing character is correlated with a shift downwards in ϕ_{P/P^+} and $\phi_{P^+/P}$ or, equivalently, E_{LUMO} and E_{HOMO} . However, ϕ_{P/P^+} for (4) and (6) has much lower difference than that found by using the frontier orbital energies. In this sense, a diminished thermodynamic driving force for electron transfer for (5) can represent a disadvantage to drive this uphill reaction and compensate for the overpotentials, even with a potential of the redox pair (H^+/H_2) positioned at -4.16 eV for pH= 4. From this point of view, MeO and F-substituted polymers are stronger candidates for HER photocatalysis than the CN-based compound itself. However, Group D (9-10) are still more interesting for photocatalytic purposes because they present a drastically decrease in the optical gap, while still showing driving force to promote the charge transfer processes.

3.6.3. Thermodynamic Driving Force for Charge Transfer: Donor Tailoring

In this part, I evaluate the electrochemical window for benzothiadiazole-based polymers with a varying donor unit in 1-bromooctane or aqueous medium. The former environment gives us the description of charge transfer processes that takes place inside the bulk material, but it is the latter that comprises the ideal condition where the polymer is well dissolved in aqueous solvent. Figure 3.15 displays the potentials for redox pairs (P^+/P) and (P/P^+) in the black curves, being these quantities comparable to the reported values from cyclic voltammetry. The so-called fundamental gap exhibits better agreement with experimental values by using water as the implicit solvent, with deviations of about 0.05-0.32 eV.

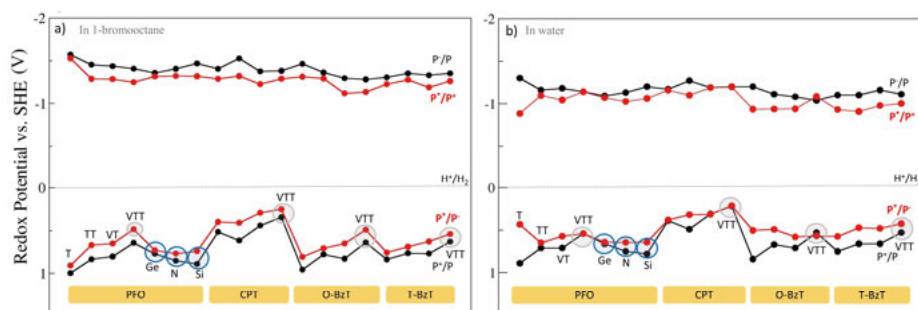


Figure 3.15- Electrochemical window obtained for benzothiadiazole-based polymers via *ab initio* calculations in a) 1-bromooctane and b) water. Ge, N and Si are simplifications for PGF, PCz and PSiF-based polymers. Reprinted with permission from Damas *et al.*¹⁹ Copyright (2019) American Chemical Society.

In Figure 3.15, it is also clear that the solvent environment does not affect the general trend upon donor tailoring, but it does affect ϕ_{P/P^*} to promote a shift downwards in this quantity. The potentials for redox pairs (P^+/P^*) and (P^*/P^-) that are represented by red curves indicate lower thermodynamic driving forces for charge transfer processes upon photoexcitation, which demonstrate its importance for proper assessment of these quantities. All systems have catalytic power for proton reduction, being ϕ_{P^*/P^-} a quantity this is more affected upon donor tailoring. In particular, cyclopentadithiophene units promote a higher shift in ϕ_{P^*/P^-} to diminish ΔG for hole removal.

3.6.4. Hydrogen Binding Free Energies: Group A polymers

In Table 3.4 and Figure 3.16 (a), we can visualize the thermodynamic properties of the hydrogen binding free energies in gas phase and including the solvation effects. These results were obtained at B3LYP/6-31G* with single point using 6-311G** basis set, being published in Paper I. In principle, no significant differences were found in the ΔG_H values upon inclusion of an implicit solvent, indicating that the gas phase can be safely used to describe these properties while saving computational resources and time. From this point, $\Delta G_{H(g)}$ will be referred simply as ΔG_H . It is also valid to mention that the dimer models utilized for this study provide a total number of four nitrogen atoms at the BT blocks, enabling an analysis on the hydrogen content over the binding free energy, as described in the last lines in Table 3.4 and Figure 3.16 (b).

Table 3.4 - Hydrogen binding free energies obtained in gas phase and aqueous medium. Level of theory: B3LYP/6-31G*(6-311G**). Palas *et al*⁸- Published by The Royal Society of Chemistry.

| System | Site | Gas phase | | Solvated phase | |
|--------------------|------|-----------------------------|---------------------------|--------------------------------|------------------------------|
| | | $\Delta G_{H(g)}$ (a.u.) | $\Delta G_{H(g)}$ (eV) | $\Delta G_{H(solv)}$ (a.u.) | $\Delta G_{H(solv)}$ (eV) |
| F8T2-H | S | 0.083 | 2.264 | 0.083 | 2.264 |
| PFBT-H | S | 0.078 | 2.110 | 0.073 | 1.990 |
| PFBT-H | N | 0.024 | 0.657 | 0.022 | 0.599 |
| PFO-DT-BT-H | S | 0.082 | 2.218 | 0.081 | 2.217 |
| PFO-DT-BT-H | N | 0.026 | 0.711 | 0.023 | 0.632 |
| PFO-DT-BT-2H (cis) | N | 0.020 | 0.272 | 0.017 | 0.235 |
| PFO-DT-BT-3H (cis) | N | 0.045 | 0.408 | 0.039 | 0.357 |

The first hydrogenation process shows remarkable differences if considered the nitrogen or sulfur atoms as the interaction sites. As displayed in Table 3.4 and Figure 3.16 (a), the energetics towards H_2 formation is clearly enhanced from the analysis of the N-H bond at the BT block in **(2)** and **(3)**, with a reduction in 1.5 eV ($\Delta G_H \sim 0.7$ eV) in the overpotential required to form the intermediate state in comparison to the S-sites ($\Delta G_H \sim 2.2$ eV). The stronger

interaction is also noted by considering that the H-N bond is shortened in 0.38 Å compared to H-S bond in both cases. Comparatively, the absence of nitrogen catalytic sites in **(1)** reflexes in an unfavorable ΔG_H lying in the same range as the sulfur sites in **(2)** and **(3)**.

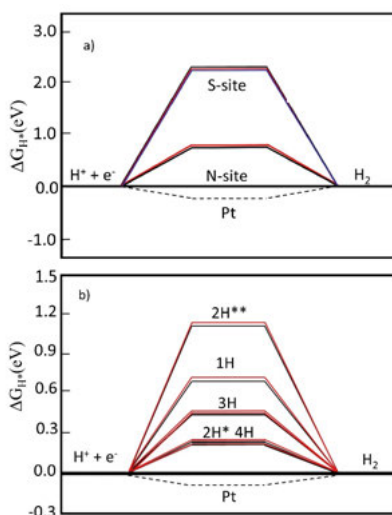


Figure 3.16- Hydrogen binding free energy (ΔG_H) a) for the first hydrogenation at the nitrogen and sulfur catalytic sites and b) for different hydrogen content. Level of theory: B3LYP/6-31G* (6-311G**). Palas *et al*⁸- Published by The Royal Society of Chemistry.

The hydrogen content has a great influence over the adsorption energy, as shown in Figure 3.16 (b). For polymers **(1)** and **(2)**, the second hydrogenation process at the same BT unit -symbolized by 2H* in Figure 3.16 (b) - reduces the adsorption energy to about 0.27 eV, whereas a raise to about 1.1 eV is seen when considering the same process at different monomeric units, as symbolized by 2H**. By saturating the first BT unit, the addition of a third hydrogen (3H) raises the overpotential compared to 2H*, but not enough to reach the first hydrogenation overpotential. Moreover, the fourth catalytic site can receive a hydrogen atom with the cost in energy of about 0.28 eV, which strongly indicates that the first/third hydrogenation favors the second/forth ones.

3.6.5. Hydrogen Binding Free Energies: Acceptor Tailoring

In Paper I, the role of nitrogen catalytic sites in **(2)** and **(3)** was unveiled through an analysis that involves ΔG_H as a descriptor for HER. It has been basically demonstrated that a more favorable $N \cdots H$ interaction was responsible to decrease the overpotential from 2.2 eV to approximately 0.7 eV for both

polymers. This study has been expanded to the Groups B-D polymers to give an interesting picture within the M06/6-311G** scheme. In Figure 3.17, these results are graphically summarized with additional value for platinum ($\Delta G_H = -0.1$ eV, dashed line).¹¹⁸

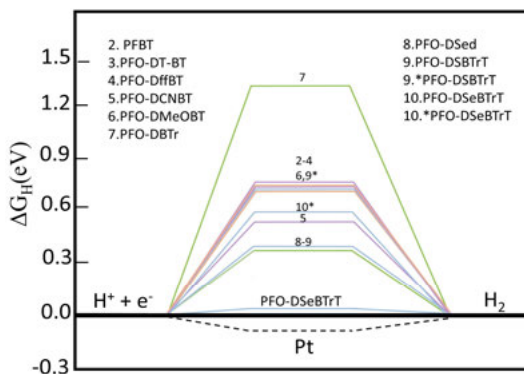
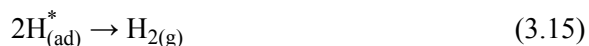


Figure 3.17- Overpotential for hydrogen evolution reaction calculated for polymers (2-10). For (9) and (10), the values referring to the second catalytic site at the triazole sub-unit present an asterisk (*). Adapted with permission from Damas *et al.*⁹² Copyright (2018) American Chemical Society.

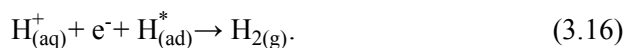
Similar to F8T2 (**1**), the combined properties of high overpotential (1.31 eV) and narrow absorption spectrum ($\lambda_{\max} = 523.40$ nm) indicate that (**7**) might not be interesting for application in photocatalysis. Nonetheless, the other materials have an improved interaction with the hydrogen atom allowing the formation of an intermediate state with lower energy cost. Except by fluorination of the BT block, the cyano-functionalization (**5**) and the replacement of sulfur atom by selenium in (**8**) sinks ΔG_H to 0.35 eV. An even deeper impact is seen by considering the BTrT-derived units in (**9**) and (**10**), where the combination of the fused ring with selenium atom in PFO-DSeBTrT (**10**) is responsible for a very low $\Delta G_H = 0.02$ eV. This excellent prediction is specially close to the thermodynamic ideal value, while lower than platinum in absolute values.¹¹⁸

3.7. Kinetic Considerations

As the intermediate state is formed, there are several pathways the molecular hydrogen can undergo. As mentioned by Putungan *et al.*¹¹⁶, two plausible mechanisms can be cited as



and



In Equation 3.15, the adsorbed hydrogen atoms interact among themselves to generate the final product, whereas in the second process one adsorbed atom receives a proton-coupled electron transfer involving protons from the solvent medium.

In Paper I, as a first assessment for the kinetic barrier involving transition states for hydrogen production, I have built several possible structures with a varying H-H distance in order to simulate the reaction mechanism described in Equation 3.15. In this sense, the $\text{H}\cdots\text{H}$ interactions at the same moiety or from different dimers are considered as distinct pathways. Since these transition states are not local minimum in the potential surface given by the optimization process, it was necessary to freeze these distances, although the polymeric system was fully optimized. A first analysis of the kinetic barriers through different pathways toward H_2 formation has been achieved within the B3LYP/6-31G* level of theory. In the black pathway shown in Figure 3.18, two interacting hydrogen atoms are located at the BT moiety, with a calculated barrier of 3.12 eV. On the other hand, when this interaction occurs between hydrogen atoms from different dimers, a significant decrease in the activation energy is observed, strongly suggesting that this pathway is more likely to occur, although the thermodynamics results point out for a favored second hydrogenation at the same catalytic center.

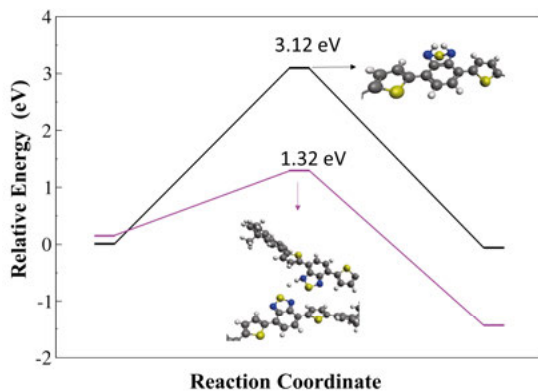


Figure 3.18- Kinetic barriers calculated through different pathways for hydrogen evolution reaction. Palas *et al*⁸- Published by The Royal Society of Chemistry.

3.8. Exciton Binding Energies

In Section 3.5, the excitonic state has been introduced as an electron-hole pair that is formed under photoirradiation at a certain wavelength (λ). This quasiparticle has an intrinsic electrostatic interaction holding the charge carriers together by a certain amount of energy, the so-called exciton binding energy (E_b). Thus, we should expect that lower E_b would lead to faster charge dissociation processes that can positively impact the photocatalytic efficiency for

hydrogen production. In fact, the recent report by Lan *et al.*¹¹⁹ have demonstrated this relation in dibenzothiophene-*S,S*-dioxide-based polymers with donor-acceptor architecture, which shows the relevance of computing this property for photocatalyst design. In Paper III, E_b has been calculated by taking the difference between the fundamental (E_f) and optical gap (E_{opt}), i. e.:⁵¹

$$E_b = |(\phi_{P/P^-} - \phi_{P^+/P})| - E_{opt}. \quad (3.17)$$

To compute ϕ_{P/P^-} and $\phi_{P^+/P}$, we have first considered the convention of approximating the Gibbs free energies of reaction in solvated environment ($\Delta_r G_{(solv)}$) by the sum⁵¹

$$\Delta_r G_{(solv)}(Red) \approx \Delta E_{elet(g)}(Red) + \Delta G_{(solv)}(Red) - \Delta G_{(solv)}(Ox). \quad (3.18)$$

This is justified by assuming that the exciton state is a very fast process that does not enable any relaxation upon electron transfer. In Equation 3.18, the total electronic energy (E_{elet}) of the ionic species, as well as E_{opt} have been calculated on the ground-state geometry of the neutral polymer.^{101,120} Relaxation effects are account for by using a non-approximated quantity for $\Delta_r G_{(solv)}$ to obtain the fundamental gap. Additionally, these effects are assessed by optimizing the geometry structures in the first excited state to estimate the optical gap. Partial results are shown in Figure 3.19, but the reader is referred to Paper III for more details.

It should also be pointed out that these photocatalysts usually form thin films or nanoparticles where excitons are formed/dissociated in their inner part. To account for such different chemical environments, we have used different solvents with varying dielectric constant in the implicit solvation model such as water, acetonitrile and 1-bromooctane.^{20,121} The latter solvent is of particular interest since its dielectric constant ($\epsilon \sim 5.0$) is very close to that measured for similar polymers.¹²¹ In general, E_b shows a substantial decrease from gas phase to solvated environment. In this sense, higher dielectric constants offered by acetonitrile and aqueous environment are expected to promote easier exciton dissociation in these materials, which is particularly valid upon good dispersion in the solvent medium.

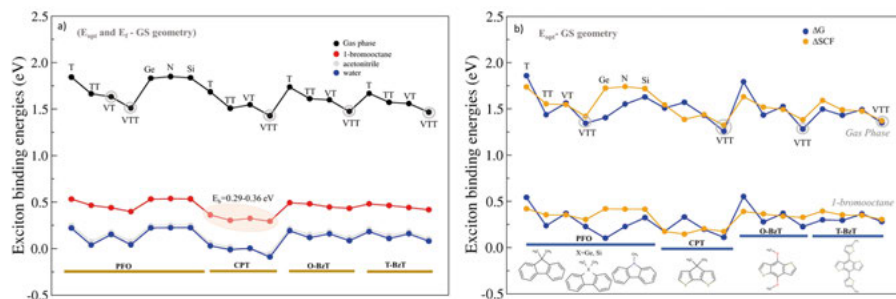


Figure 3.19- Exciton binding energies for benzothiadiazole-based compounds in gas phase (black curve) and solvent environment (colorful curves). Adapted with permission from Damas *et al.*¹⁹ Copyright (2019) American Chemical Society.

Although the heteroatom substitution at the fluorene unit by Ge, N or Si is not effective, the cyclopentadithiophene-based polymers present a great reduction in $E_b = 0.29\text{--}0.36$ eV in 1-bromooctane (see Figure 3.19 (a)), but this effect is verified regardless the dielectric constant or if the relaxation effects are taken into account. As detailed in Table 3.5, an increase in the donor/acceptor ratio to form HOMO leads to a diminished E_b , as the charge carriers present higher spatial separation with an improved donating character.

Table 3.5- Donor/Acceptor ratio for composition of frontier orbitals and E_b in gas phase as obtained through ground-state geometries. Level of theory: M06/6-311G(d,p). Adapted with permission from Damas *et al.*¹⁹ Copyright (2019) American Chemical Society.

| System | D/A ratio HOMO | D/A ratio LUMO | E_b (eV) |
|--------------|-------------------|-------------------|---------------|
| PFO-DT-BT | 3.68 | 0.32 | 1.84 |
| PFO-VTT-BT | 6.61 | 0.31 | 1.51 |
| CPT-DT-BT | 6.24 | 0.43 | 1.69 |
| CPT-VTT-BT | 10.90 | 0.43 | 1.43 |
| O-BzT-DT-BT | 5.32 | 0.44 | 1.74 |
| O-BzT-VTT-BT | 9.30 | 0.42 | 1.47 |
| T-BzT-DT-BT | 6.19 | 0.35 | 1.67 |
| T-BzT-VTT-BT | 9.07 | 0.41 | 1.47 |

4. Molecular Modelling of Symmetric Small-Molecules for Hydrogen Evolution

Small-molecules (SM) constitute a class of organic materials with well-defined weight that offers the possibility of synthesis in several configurational architectures.^{122–125} In this sense, these materials can be applied in photocatalytic hydrogen production as they have exhibit sunlight absorption at the UV-Vis region,^{126–129} with an energy gap that can be adjusted by combining chemical moieties with donating and accepting character.¹³ In the next sections, I summarize the results from Paper IV, where a set of small-molecules have been evaluated via *ab initio* methods for potential applicability in photocatalytic hydrogen production.

4.1. Systems under investigation

In Figure 4.1 the small-molecules of interest have their central donor region given by the cyclopentadithiophene unit, which is linked to thiophene (T) or 3,4-ethylenedioxythiophene (EDOT) units. The acceptor is the well-known benzothiadiazole (BT) unit in connection with thiophene or accepting 1,3,4-thiadiazole (Tz) units. In SM-DFM compounds, the benzothiadiazole unit has been functionalized in the 5,6 positions by difluoromethoxy (DFM) groups.

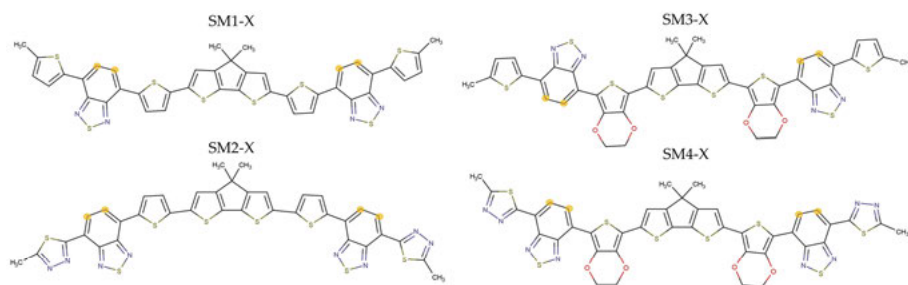


Figure 4.1– Chemical structures of SM-X compounds (X=H or DFM). They differ by the difluoromethoxy (-OCF₂H, DFM) functionalization at the benzothiadiazole unit, as indicated by the orange dots.

To assess the UV-Vis absorption fingerprints and the thermodynamic driving force for charge transfer-related processes, we have chosen Gaussian 16⁶⁴ to

perform the calculations in gas phase and aqueous environment within the M06/6-31G*(6-311G**) level of theory in a stepwise sequence. More details on the computational approach are available in Paper IV.

4.2. UV/Vis Absorption Spectra

The systems herein under investigation exhibit a low intrinsic energy gap lying in the range 1.72-1.82 eV that enables their applicability for UV-Vis absorption. This property is determined by the electronic transition between HOMO/LUMO orbitals to generate the first maximum at $\lambda_{\text{max}} = 684\text{-}719\text{ nm}$. Hence, these molecules present a broad absorption spectrum with $\lambda = 318\text{-}719\text{ nm}$, as depicted for selected systems in Figure 4.2.

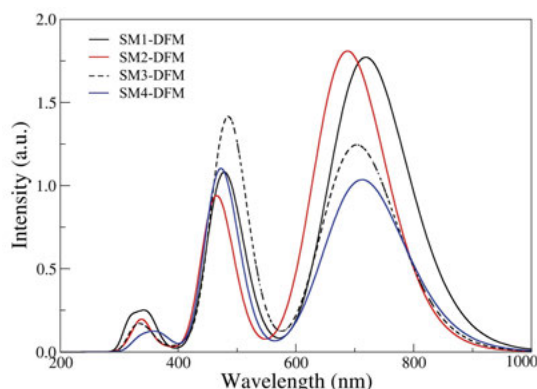


Figure 4.2- Theoretical UV-Vis spectra for SM-DFM compounds with intensities weighed by the oscillator strength of each electronic transition. Level of theory: M06/6-311G**. Reprinted with permission from Damas *et al* (Paper IV). Copyright (2019) American Chemical Society.

To unveil the electronic transition nature with highest contribution to the main absorption peaks, we have plotted the spatial distribution of frontier orbitals for the functionalized molecules. In Figure 4.3, we can visualize an overall delocalization of the highest occupied molecular orbital over the donor region defined by cyclopentadithiophene, T or E-DOT units. The benzothiadiazole unit guarantees a localized electron density upon photoexcitation, which is partially extended to the thiadiazole units in the termination sites. Therefore, the first electronic transition has a charge-transfer nature that is expected to avoid losses from charge recombination processes.⁸ In contrast, the HOMO \rightarrow LUMO+2 occurring at $\lambda_2 < 490\text{ nm}$ has an intramolecular $\pi\text{-}\pi^*$ character, as the involved orbitals are found widely distributed over the π -conjugated system.

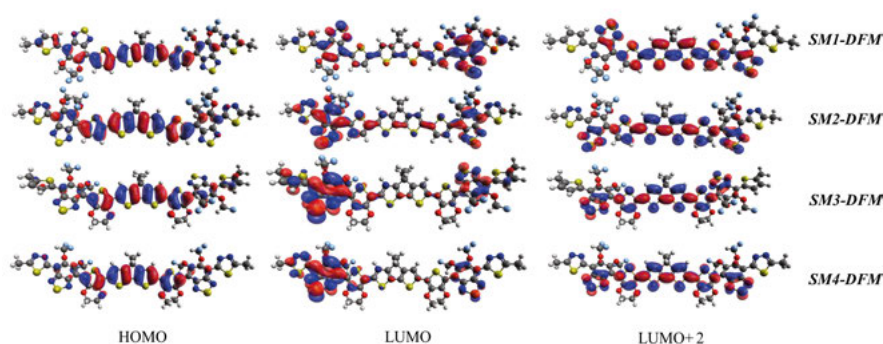


Figure 4.3 –Spatial distribution of frontier orbitals that participate in the main electronic transitions of SM-DFM compounds obtained at the isovalue= 0.02. Reprinted with permission from Damas *et al.* (Paper IV). Copyright (2019) American Chemical Society.

4.3. Reaction Thermodynamics

The analysis of potentials of redox pairs that are depicted Figure 3.9 has been extended to the small-molecules in the present study. The outcomes clarify that a positive catalytic power for electron transfer to generate hydrogen is found for all systems. Furthermore, the following effects have been verified upon structural modifications (see Figure 4.4):

- (1) Thiadiazole (Tz) units at the terminations promote a shift of ~ 0.3 V on the potentials of redox pairs (SM^+/SM^-) and (SM/SM^-);
- (2) The donating character from EDOT units moves upwards the potentials of (SM^+/SM^-) redox pairs in about 0.34-0.48 V, but it does not affect significantly the redox potentials associated with E_{LUMO} ;
- (3) Difluoromethoxy (DFM) groups improve the acceptor character from the BT unit by shifting the potentials of redox pairs (SM/SM^-) and (SM^+/SM) downwards in about 0.04-0.26 V.

Based on earlier work by Wang *et al.*,¹²⁸ we have explored the concept of forming cooperative photocatalysts couples aiming at enhance the photocatalytic efficiency. As illustrated in Figure 4.4 (a), three couples have been proposed in accordance with the proper alignment of their redox potentials. For instance, in Couple 2 the photoexcitation of SM2-DFM at $\lambda = 687.96$ nm leads to a favorable hole transfer ($\text{SM2} \rightarrow \text{SM3}$). Similarly, SM3-DFM can be photoexcited at $\lambda = 704.26$ nm, a process that is followed by electron transfer from $\text{SM3} \rightarrow \text{SM2}$. The thermodynamic driving force (ΔG) is about 0.3 eV for these processes.

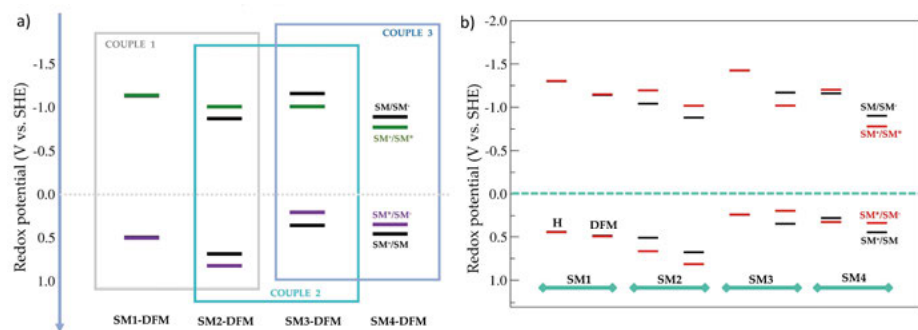


Figure 4.4— Redox potentials (vs. SHE) for the systems under investigation are indicated by the black and colourful horizontal bars. Reprinted with permission from Damas *et al.* (Paper IV). Copyright (2019) American Chemical Society.

The quantity defined by the hydrogen binding free energies (ΔG_H) has been employed for further evaluation of nitrogen atoms acting as the catalytic sites to form the intermediate species. In Paper IV we have basically tested the nitrogen atom originated from BT or Tz sites. At the BT unit, ΔG_H suffers a decrease of ~ 0.2 eV upon introduction of EDOT units in SM3- and SM4-DFM compounds. However, Tz sites hold the lowest values for hydrogen binding free energies in the series. In particular, this quantity reaches a minimum value for the Tz site in SM4-DFM ($\Delta G_H = 0.08$ eV) that is comparable to the well-known platinum catalyst ($\Delta G_H = -0.10$ eV)¹¹⁸. As depicted in Figure 4.5, the lowest binding free energies are found for the catalytic sites that are situated next to EDOT or DFM groups. In fact, the latter group has an important role on improving the hydrogen interaction with the molecular system by providing oxygen atoms that are also able to interact with the newly added hydrogen atom. In SM-H compounds, the absence of DFM groups is actually the reason behind the higher hydrogen binding free energies for similar compounds (see Paper IV for more details).

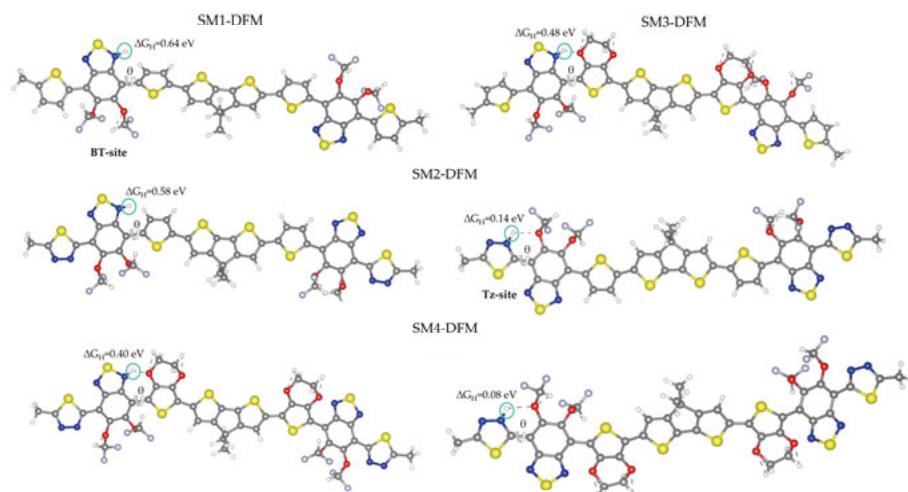


Figure 4.5 – Molecular structures of SM after hydrogenation at the benzothiadiazole (BT) or thiadiazole (Tz) site. In detail, the hydrogen binding free energies (ΔG_H) at the corresponding catalytic site. Reprinted with permission from Damas *et al.* (Paper IV). Copyright (2019) American Chemical Society.

5. Solid-State Modelling of the Carbon Dioxide Reaction on Sn-based Electrodes

In the context where new alternatives are sought to deal with the global warming problem,^{2,132} the carbon dioxide recycling into valuable fuels represents a step forward to an environment friendly society. Sn-based electrodes have been extensively investigated for this application^{132–136} for its low toxicity and price, while also exhibiting high efficiency for formic acid production with a low associated energy cost.¹³⁷ In the contribution from Paper V, we have combined experimental and theoretical approaches to understand the role of tin oxide surfaces in the formic acid production from carbon dioxide. In particular, our collaborators have prepared two tin-based electrodes that were submitted to acid etching process for further removal of the tin oxide layer. Interestingly, the analysis from X-ray photoelectron spectroscopy (XPS) has shown that both electrodes presented a very similar composition of SnO₂ (86 and 94%) and metallic Sn (14% and 6%) regardless the time of air exposure. Furthermore, the cyclic voltammetry measurements have returned an onset potential at *ca.* -0.8 to -0.9 V (vs. RHE) for product formation, with a maximum faradaic efficiency of about 90- 92% at -1.25 V (vs. RHE). In this Section, I describe the theoretical modelling of tin-based electrodes based on SnO and Sn₆O₄(OH)₄ bulk structures along with the main outcomes to provide important insights into the reaction mechanism herein under investigation.

5.1. Computational Approach

The Vienna Ab-Initio Simulation Package (VASP)⁶⁵ is the code of choice to perform the *ab initio* calculations in Paper V. The Kohn-Sham equations were solved within the project augmented wave (PAW) scheme. In the next subsections, I detail the stepwise procedure to attain the SnO_x surface model that is suitable to study the reaction thermochemistry in the present study.

5.1.1. Bulk Structures

The description of the SnO_x layers has been achieved by selecting SnO and Sn₆O₄(OH)₄ as the tin-based materials. The initial lattice parameters and ionic positions have been obtained from the crystallographic data,^{29,138–140} being

fully optimized by using the Perdew-Burke-Ernzerhof functional (PBE)⁷¹ with inclusion of D3-Grimme corrections.⁶² The bulk structures for these systems are illustrated in Figure 5.1.

The tin (II) oxide is usually described as a semiconductor with small band gap ($E_g = 0.7$ eV),¹⁴¹ but it can also present semi-metallic character. This material has tetragonal structure with the symmetry determined by the $P4/nmm$ space group. At the PBE/700 eV level of theory, the band gap is underestimated to 0.3 eV, a problem that is not supposed to affect the reaction thermochemistry. However, it has been verified that the HS06 functional is able to reproduce the experimental value by using 38% of exact exchange. The tin (II) oxyhydroxide has crystallization within the $P\bar{4}2_1c$ space group showing large band gap ($E_g = 3.36$ eV) as determined with the HS06 functional (38% exact exchange).

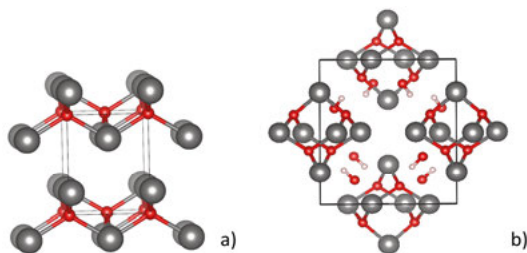


Figure 5.1. a) Tin (II) oxide (SnO) and b) tin (II) oxyhydroxide ($\text{Sn}_6\text{O}_4(\text{OH})_4$) bulk structures as obtained from optimization at PBE level. Red, silver and white colors represent O, Sn and H, respectively (Damas *et al.*).¹¹³

5.1.2. Slab Models

At this stage, the bulk structures have been cut in different directions for crystal growth. From this point, a varying number of 3-11 layers for SnO and 2-6 layers for $\text{Sn}_6\text{O}_4(\text{OH})_4$ were used to determine the most stable facet. This analysis has been performed based on the energy that is necessary to form the surface from an initial bulk material, i. e., the surface energies (γ)¹⁴²

$$\gamma = \frac{E_{\text{slab}} - t \times E_{\text{bulk}}}{2A}. \quad (5.1)$$

In Equation 5.1, E correspond to the total energies from the slab model E_{slab} and the bulk structure E_{bulk} , whereas t is the number of layers and A is the surface area.

The outcomes reveal that the lowest surface energy for the SnO slabs is the [001] orientation, with $\gamma = 0.353$ J/m². For $\text{Sn}_6\text{O}_4(\text{OH})_4$, the [011] orientation has been selected since it presents a closed-packed structure with low $\gamma = 0.175$ J/m². The final slab structure was constructed by expanding the surface area in 2x2, while reducing the slab thickness to two-layers to reduce the computational time. For SnO, it has also been added -OH surface groups in order to

reproduce the hydroxylation process on tin-based electrodes (see Figure 5.2 (a)). Therefore, this model is further referred as SnOOH or Model I. For $\text{Sn}_6\text{O}_4(\text{OH}_4)$, now referred as Model II, it has also been considered the isolated cluster placed in the middle of an empty box (see Figures 5.2 (b) and (c)).

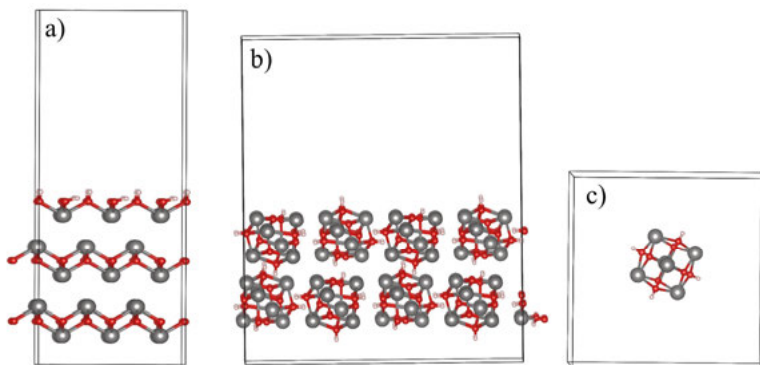


Figure 5.2. Slab structure for Models (a) I and (b,c) II. In (c) the cluster from Model II is disposed in the centrum of an empty box, simulating a non-crystal environment. In Model I, there is a relation of two hydroxyl groups for each Sn surface atom (Damas *et al.*).¹¹³

5.1.3. Electronic Structure

The total and partial density of states for Models I and II are shown in Figure 5.3. The top of the valence band is formed by O $2p$ and Sn $5s$ orbitals, which is indicative of charge transfer between these atoms. On the other hand, Sn $5p$ and O $2p$ antibonding states have predominant contribution to form the bottom of the conduction band. Here, the unique difference exhibited by the cluster system is the enlarged band gap due to quantum confinement effects.

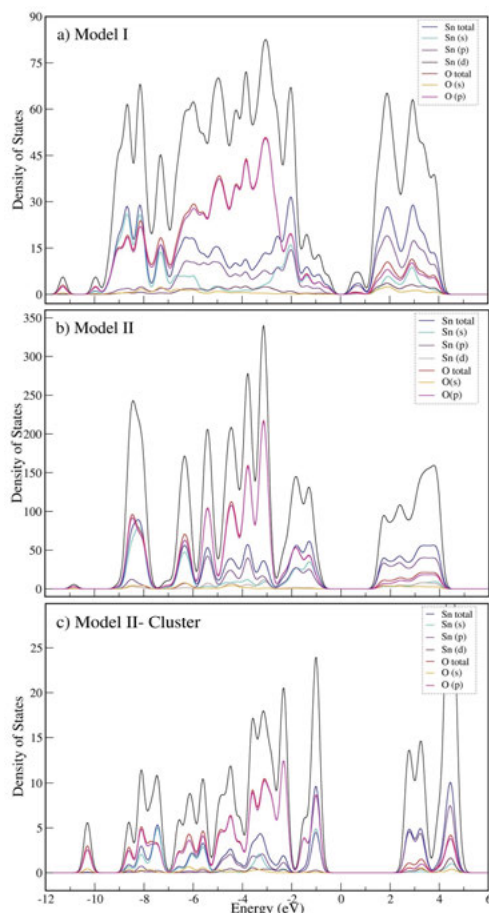


Figure 5.3. Total and partial density of states of Models a) I, b) II and c) the cluster in a non-periodic environment. The Fermi energy is set to zero (Damas *et al.*).¹¹³

5.2. Carbon Dioxide Insertion

The first step in the electrocatalytic process for formic acid generation is the insertion of carbon dioxide molecule into the -OH group localized at the surface from Models I and II, but also present in the cluster system. This insertion step is followed by the formation of a tin-carbonate species that remains bound to the surface model until the applied potential is raised. In order to evaluate the feasibility of this process in a thermodynamic point of view, the variation in energy (ΔE) with the molecule adsorption has been calculated in gas phase and aqueous environment. The latter has been attained by using the Born-Haber thermodynamic cycle described in Scheme 3.1, with solvation energies obtained in VASP-Sol code.¹⁴³ It is clear from Figure 5.4 that the carbon dioxide insertion into the -OH group is a thermodynamic favorable process re-

ardless the model ($\Delta E = -0.32$ to -0.75 eV), although SnOOH (Model I) exhibits a stronger C-O bond between the adsorbate and surface to hold the intermediate species.

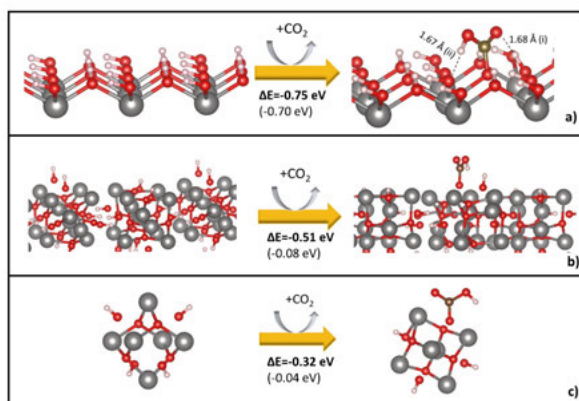


Figure 5.4. Schematic representation of carbon dioxide insertion at -OH site in the electrocatalyst surface of a) Model I, b) Model II and c) cluster. ΔE stands for variation in the electronic energy with inclusion of solvation energies, except for the values in parenthesis (Damas *et al.*).¹¹³

5.3. Reduction Reaction

In the next step, the tin-carbonate species undergoes to a proton-coupled electron transfer that results in product formation, where the formic acid is released by connecting the hydrogen atom to the carbon site (see Figure 5.5). Nonetheless, tin and oxygen atoms have also been tested as interaction sites with the newly added hydrogen atom to generate water, carbon monoxide or molecular hydrogen in Model I, as seen in Figure 5.6. These processes have been evaluated by computing the reduction potentials (ϕ) from Equations 3.6-3.8. To accomplish this task, the Gibbs free energies of reaction in aqueous environment have been approximated to the sum between electronic and solvation energies, a relation that was clarified in Equation 3.18. Values in Figures 5.5 and 5.6 are given in reference to the reversible hydrogen electrode (RHE).

Model I ($\phi = -1.09$ V) has the best agreement with our experimental outcomes, i.e., onset potential at -0.8 to -0.9 V and maximum faradaic efficiency at $\phi = -1.25$ V. In Figure 5.7 (b), the alternative pathway resulting in hydrogen evolution reaction is expected to be a competitive reaction in a theoretical point of view ($\phi = -0.57$ V), but its production is just found significant at much lower potentials upon the SnO_x layer reduction to metallic Sn. On the other hand, Model II has a much lower value $\phi = -1.65$ V that is far more coherent with the previous report by Baruch *et al.*¹³² For this system, the crystal environment does not exhibit major differences from the layered structure in the pathway involving the release of formic acid.

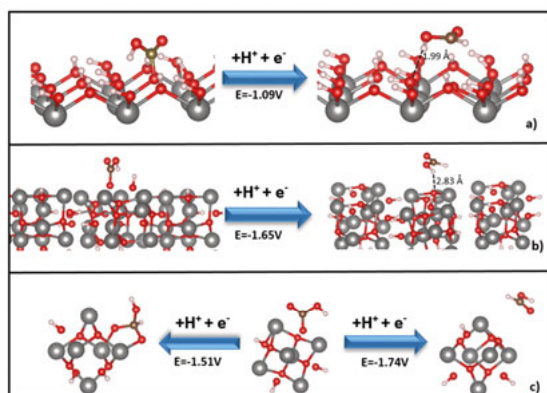


Figure 5.5. Schematic representation of the proton-electron coupled transfer in the electrocatalyst surface of Models a) I, b) II and c) the isolated cluster. E stands for redox potential vs. RHE (Damas *et al.*).¹¹³

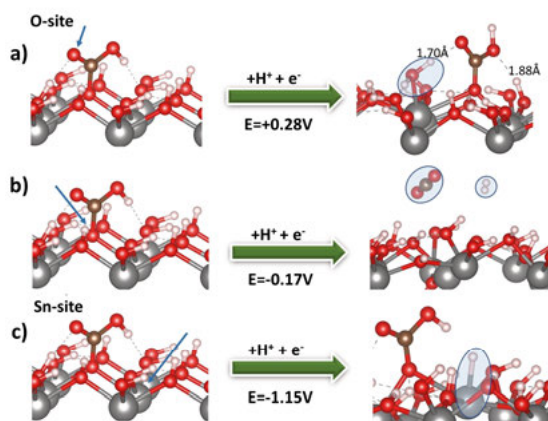


Figure 5.6. Alternative pathways for the first hydrogenation process on the a) and b) O-site and c) Sn-site, with no formic acid as the resulting product. Values are given vs. RHE (Damas *et al.*).¹¹³

6. Molecular Modelling of Ru-complexes for Electrocatalytic Applications

In this section, I briefly describe the initial assessment of minimum energy geometries and multiplicity states for $[\text{RuII}(\text{bpy})_2(\text{py})(\text{OH}_2)]^{2+}$ and its oxidation products, which have been investigated in Paper VI. Additionally, I consider the $[\text{Ru}(\text{bpy})_2(\text{CO})_2]^{2+}$ complex as the starting material for carbon dioxide conversion into formic acid in the contribution from Paper VII. In this study, the reduction pathways have been studied along with the reaction mechanism that takes into account the formation of a hydride complex in solution. In fact, the electrochemistry associated with the oxidation processes has also been investigated for a future publication, but it will not be shown in this thesis.

6.1. Computational Approach

6.1.1. The $[\text{RuII}(\text{bpy})_2(\text{py})(\text{OH}_2)]^{2+}$ Complex and Derivatives

The $[\text{RuII}(\text{bpy})_2(\text{py})(\text{OH}_2)]^{2+}$ starting complex has an octahedral coordination geometry with water and pyridine ligands disposed at the cis-positions related to each other (see Figure 6.1). In Paper VI, this d^6 complex undergoes to different pathways upon oxidation leading to molecular intermediates that can be represented by the general formula $[\text{Ru}(\text{bpy})_2(\text{py})(\text{L})]^{+y}$, where L is the ligand (water, hydroxo or oxo ligand) and y is the complex total charge (+1,+2,+3). Additionally, the ruthenium atom presents a varying formal charge (II-V).

The quantum chemistry calculations were held in gas phase within the density functional theory framework as implemented in Jaguar code program.¹⁴⁴ The B3LYP/6-311G (d,p) level of theory was chosen for the energetic calculations at 0 K, but thermal corrections were also applied to the internal energy for a proper assessment of the Gibbs free energies of each system. For ruthenium, it was necessary to use the LACV3P pseudopotential. The molecular geometries with minimum energy were then used to perform the Monte Carlo simulations in aqueous environment, an approach that is out of scope of this thesis. In general, the lowest spin multiplicity is the configuration of choice for $[\text{Ru}(\text{bpy})_2(\text{py})(\text{L})]^{+y}$ and $[\text{RuIV}(\text{bpy})_2(\text{py})(\text{O-OH})]^+$ complexes by about 1.2- 36.9 kcal/mol, where L is the water or hydroxo ligand. On the other hand,

other monomeric RuIV-based complexes have shown a higher stabilization with two unpaired electrons by about 12-23 kcal/mol.

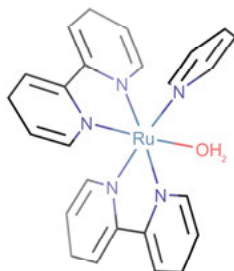


Figure 6.1- Molecular geometry of $[\text{RuII}(\text{bpy})_2(\text{py})(\text{OH}_2)]^{2+}$, as determined within the B3LYP/LACV3P/6-311G (d,p) level of theory in Jaguar code.¹⁴⁴

6.1.2. The $[\text{RuII}(\text{bpy})_2(\text{CO})_2]^{2+}$ Complex and Derivatives

In Paper VII, the pathways of reduction of the starting Ru-complex $[\text{RuII}(\text{bpy})_2(\text{CO})_2]^{2+}$ have been investigated by using density functional methods in Gaussian 09.⁶³ To compute the redox potentials in aqueous environment from Equations 3.6- 3.9, it has been employed the Born-Haber thermodynamic cycle shown in Scheme 3.1. Figure 6.2 exhibits the structural formula of the starting Ru-complex (**1**), which has electrocatalytic activity for carbon dioxide reduction upon the attachment on N-Ta₂O₅ semiconductor in acetonitrile/TEA (5:1) solution.¹⁴⁵ This complex is stabilized in an octahedral geometry containing a ruthenium metallic center with electronic configuration $[\text{Kr}] 4d^6$ and valence +2. Thus, (**1**) is a low spin state complex with a closed shell configuration.

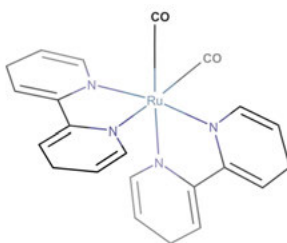


Figure 6.2- Molecular geometry of $[\text{RuII}(\text{bpy})_2(\text{CO})_2]^{2+}$, as determined within the B3LYP/SDD/6-311++G (2df,2p) level of theory in Gaussian 09.⁶³

6.2. Reduction Pathways for Ru- Complexes: Thermodynamics Aspects

In Figure 6.3, we can follow the possible undergoing pathways for the starting complex $[\text{Ru}(\text{bpy})_2(\text{CO})_2]^{2+}$ (**1**) upon reduction. All values for redox potentials are given in V (vs. the calculated SHE, $\phi = +4.26\text{V}$). The first electron injection has a calculated $\phi = -0.69\text{ V}$ at the B3LYP/6-311++G (2df,2p) level of theory and solvation model (PCM), showing a very good agreement with the experimental reported value in acetonitrile ($\phi = -0.7\text{ V}$).¹⁴⁵ From this point, (**2**) is likely to release the CO ligand in the solvent medium, a process that is followed by the generation of the hydride complex (**7**) at $\phi = -1.04\text{ V}$, which is the active species for the electrocatalytic process. In fact, this reduction step is supported by the experimental measurement in presence of carbon dioxide ($\phi = -1.0\text{ V}$).¹⁴⁵ In Figure 6.3, it is also available the route that takes into account the bipyridine ligand release (left pathway), which leads to the polymerization in solution.

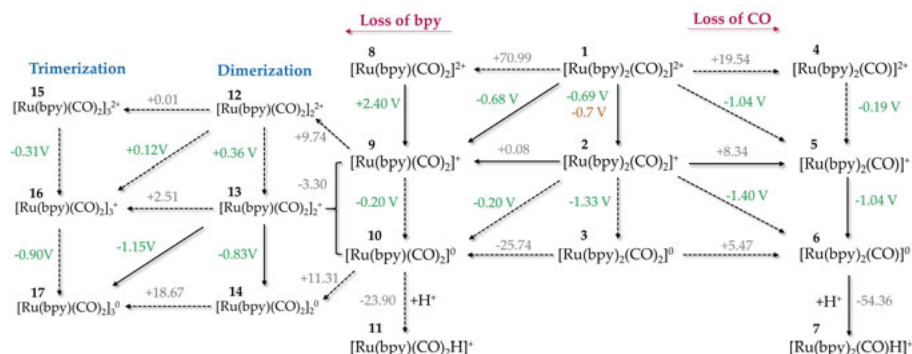


Figure 6.3- Reduction Pathways of Ru-based electrocatalysts for carbon dioxide conversion into formic acid, with values given in V vs. SHE (green) or kcal/mol (blue). Level of theory: B3LYP/6-311++G(2df,2p)/ PCM solvent implicit model.

6.3. The Reaction Mechanism

To further evaluate the formation of different intermediates for formic acid production, we have considered the carbon dioxide insertion via carbon ($-\text{COOH}$) or oxygen ($-\text{OCHO}$) atom into the Ru-H bond from the so-called hydride complex (**7**). The reaction pathway is displayed in Figure 6.4, where the $\Delta_r G_{(\text{solv})}$ values are given in reference to the initial hydride complex (**7**).

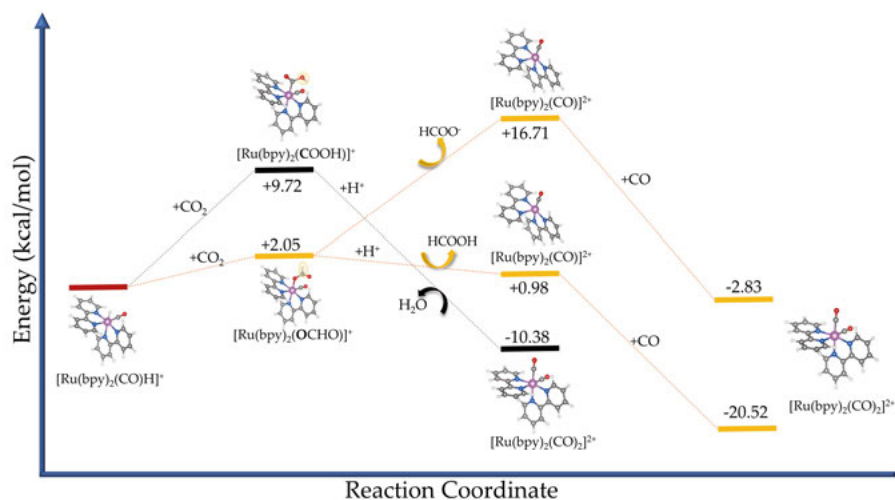


Figure 6.4-Energy diagram for different pathways of CO₂ conversion with $\Delta_r G_{(\text{solv})}$ (kcal/mol) given in relation to the hydride complex (7).

In this process, the proper alignment between reduction potentials from carbon dioxide and the Ru-complex itself enables an internal charge transfer to the reactant, as evidenced by the negative charge ($-0.41e$ and $-0.52e$) concentrated on these intermediates. In this sense, the estimated energy barrier to generate $[\text{Ru}(\text{bpy})_2(\text{CO})(\text{COOH})]^+$ (**18**) is $\Delta_r G_{(\text{solv})} = +9.72$ kcal/mol, whereas the $[\text{Ru}(\text{bpy})_2(\text{CO})(\text{OCHO})]^+$ (**19**) system has a much more favorable value ($\Delta_r G_{(\text{solv})} = +2.05$ kcal/mol). From this step, the complex **18** is protonated to regenerate the starting complex (**1**), while producing water. On the other hand, the complex **19** is likely to generate a weakly bound formic acid upon protonation at an energy cost $+0.98$ kcal/mol in relation to the hydride complex (**7**), with a regeneration of the starting complex that is highly favorable (-20.52 kcal/mol). At this point, one should notice that the CO is a natural product resulting from the ligand loss after the first reduction process.

7. Solid-State Modelling of Metal-Organic Frameworks for Carbon Dioxide Capture

Metal-organic frameworks have received a great deal of attention in the last decade for gas capture and storage applications due to their attractive structural properties, including a high surface area and pore size as well as the presence of open metal sites for several systems with high adsorption capacity.^{146,147} Here, I summarize the outcomes from Paper VIII, where it has been investigated the effects of substituting the metallic center in the electronic structure and applicability in carbon dioxide capture of a MIL-53 (X) series, where $X = \text{Fe}^{3+}$, Al^{3+} , Cu^{3+} . This project has a theoretical viewpoint with employment of solid-state modelling approach based on plane-wave expansion of atomic basis functions.

7.1. Bulk Structures

Modelling the metal-organic frameworks here under consideration has required the use of reported crystallographic data from MIL-53 (Fe^{3+}) as the primary step.¹⁴⁸ The original structure has been altered since hidden hydrogen atoms in the hydroxyl groups are found necessary to provide a better description of the real system. Additional water molecules have been removed to attend the requirement for structure activation in these systems.¹⁴⁹

Figure 7.1 illustrates the pore structure for MIL-53 (Fe^{3+}) after ionic position relaxation within the PBE¹⁵⁰/800 eV level of theory. MIL-53 (Al^{3+} , Cu^{3+}) exhibit a similar configuration since their initial crystalline structures have been built upon replacement of the iron ions by aluminum or copper ions. These materials have unit cell defined by the lattice parameters $a = 19.32 \text{ \AA}$, $b = 15.04 \text{ \AA}$, $c = 6.84 \text{ \AA}$ and $\beta = 96.3^\circ$ with crystallization in the $P 2_1/c$ space group.

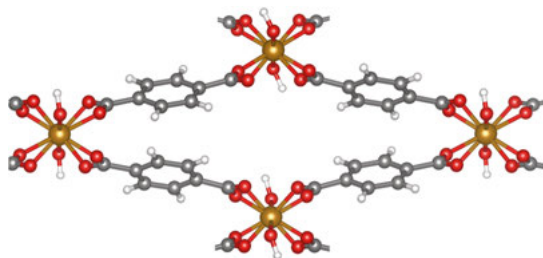


Figure 7.1- Pore detail in MIL-53 (Fe^{3+}) after optimization at the PBE/800 eV level of theory with inclusion of spin-polarized effects. Code: VASP.⁶⁵

7.2. Electronic Structure

This analysis has been initially performed to provide a quantitative description of the intrinsic band gaps that are necessary to validate the theoretical methodology. In this sense, Figure 7.2 displays the density of states distribution for all metal-organic frameworks under investigation within the PBE level with Hubbard corrections in (a) and (c), whereas such corrections have not been applied in (b). In Figure 7.2 (a), MIL-53 (Fe^{3+}) displays theoretical band gap ($E_g = 2.20$ eV) that is in fair agreement with the report by Zhang *et al.*¹⁵¹ In this system, Fe^{3+} ions have atomic magnetic moment estimated as $4.5 \mu_B/\text{atom}$, suggesting a high-spin electronic configuration with 5 unpaired d electrons in the outermost shell of each ion. Furthermore, MIL-53 (Fe^{3+}) has valence band maximum composed by O $2p$ and Fe $3d$ states whereas the spin-down contributions from Fe $3d$ states play a major role on the conduction band minimum.

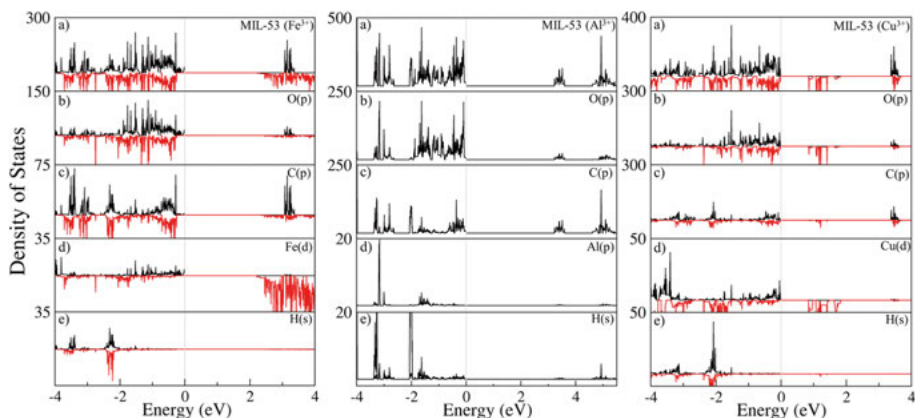


Figure 7.2- Density of states obtained for a series of metal-organic frameworks. Level of theory: PBE/ 800 eV for MIL-53 (Al^{3+})/ GGA+U/ 800 eV, with $U = 7$ eV on Fe $3d$ states for MIL-53 (Fe^{3+}) and 7 eV on Cu $3d$ states for MIL-53 (Cu^{3+}).

In Figure 7.2 (b), the large band gap of MIL-53 (Al^{3+}) arises from the high-lying C $2p$ and O $2p$ antibonding orbitals in the conduction band minimum, whereas Al $3p$ states do not exert any contribution in this region. In this study,

MIL-53 (Al^{3+}) has theoretical gap ($E_g = 3.23$ eV) that also exhibits good agreement with the experimental report.¹⁵² In Figure 7.2 (c), MIL-53 (Cu^{3+}) has a similar density of states distribution to the iron-based MOF, but the band gap is significantly reduced to 0.83 eV, whereas the copper atoms display a much lower atomic magnet moment ($0.91 \mu_b$) resulting from the unique unpaired valence electron.

7.3. Gas Capture

To evaluate the effects of replacing the metallic center on the gas capture related properties in the MIL-53 series, the initial bulk structure has been expanded into a 2x2 supercell for placement of carbon dioxide molecules inside the pore structure. In this sense, the interaction strength between the guest molecule and the framework has been estimated by using the relation

$$\Delta E = E_{\text{MOF-gas}} - E_{\text{MOF}} - E_{\text{gas}}, \quad (7.1)$$

which is basically the difference in electronic energy of the final system after gas adsorption ($E_{\text{MOF-gas}}$) and the isolated species (E_{gas} and E_{MOF}). In Paper VIII, $E_{\text{MOF-gas}}$ has been computed by placing the guest molecules in different positions inside the pore structure (see Figure 7.3).

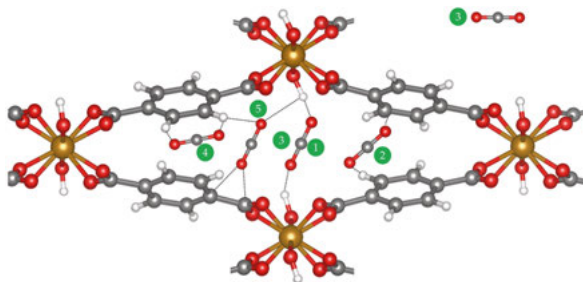


Figure 7.3- Initial configurations for carbon dioxide adsorption inside the pore structure in MIL-53 (Fe^{3+}).

In this MIL-53 series, the most favorable configuration for the guest molecule is in the middle of the pore, where long-range interactions take place with hydrogen atoms from -OH groups, as shown in Figure 7.4. Thus, such interaction is not sufficient to change any involved bond length in a significant way. In general, it has been found that spin-polarization effects exert an influence on the binding energies and chemical trends that cannot be neglected. For instance, MIL-53 (Fe^{3+}) has binding energies lying in the range -28.80 to -146.88 kJ/mol including spin-polarization effects within the PBE level, whereas an interval of about 31.68 to -73.92 kJ/mol was found for non-polarized case. Additionally, the intrinsic atomic magnetic moment for Fe and Cu

atoms was solely described in a proper way by using Hubbard corrections before and after gas adsorption, which suggests that the electronic energies are affected in a different way throughout this process, which might be the reason for the overestimated values for binding energies found for the iron-based MOF. MIL-53 (Al^{3+}) has the most favorable binding energy estimated as -33.60, which is in better agreement with the experimental reported absorption enthalpy than previous works. Furthermore, MIL-53 (Cu^{3+}) has binding energy of -33.60 kJ/mol at the most favorable configuration without spin-polarization effects and using PBE functional. This is actually comparable to MIL-53 (Al^{3+}) within the same level of theory, which suggests that this material can be interesting for gas capture purposes. At GGA+U level, this quantity has a decreased value to -20.37 kJ/mol.

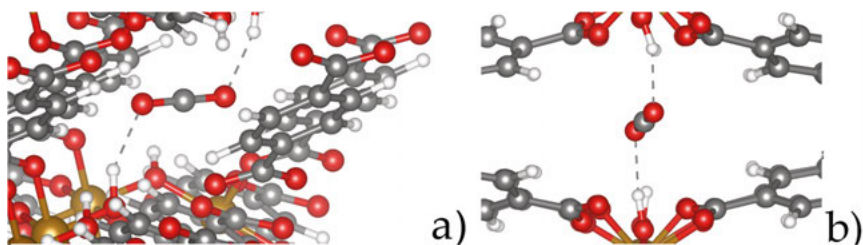


Figure 7.4- Final configuration (1) after the relaxation process carried out with spin-polarization for MIL-53 (Fe^{3+}). Level of theory: PBE/ 550 eV.

Sammanfattning på svenska

Solenergi är en naturlig kandidat för att tillfredsställa den globala efterfrågan på energi som för närvarande är satt till 14 TWh/år, eftersom dess förekomst når 100 000 TWh på årsbasis med ett belopp per dag (274 TWh) som är tillräckligt för att uppfylla de mänskliga behoven. Faktum är att den huvudsakliga användningen av fossila bränslen för att uppnå ett sådant energibehov har intensifierat den globala uppvärmningen alltigenom åren, ett välkänt miljöproblem som vårt samhälle står inför sedan den industriella revolutionen. I detta sammanhang öppnar solenerginäringen genom att använda en fotokatalysator för att producera el, vattenvärme eller solbränslen inklusive väte, alkoholer och även kortkedjiga kolväten ett nytt område för utveckling av ren energi som förväntas leda marknaden på energi produktion inom en nära framtid.

Tekniker som involverar elektrokemiska anordningar som använder solljusenergi är mycket bättre utvecklade för väteproduktion än för koldioxidomvandling till organiska bränslen för närvarande. Just nu bör det betonas att denna viktiga gas inte kan utvinnas från en naturlig källa trots dess överflöd på jordskorpan, men den erhålls genom reformering av naturgas eller förnybar biomassa och vattenelektrolys, som är dyra och miljömässigt kostsamma. I denna mening är intresset som ligger på detta bränsle relaterat till dess höga duglighet som energibärare, eftersom det uppvisar högre gravimetrisk energitäthet än bensin för bränslerelaterade tillämpningar vid omgivningsförhållanden, förutom den kolfria återstoden som genereras efter förbränningsprocessen. Däremot används molekylärt väte mycket inom andra områden, varav 61% av den totala produktionen under det senaste decenniet avsett för ammoniak-härledda gödselmedel, 23% till petroleum-raffinering och 9% till metanolproduktion. Tillämpningar i bränsleceller, kraftproduktion i turbiner och rymdrelaterad teknik beaktas också.

För att vara en potentiell kandidat i solstyrd vätegenerering är det ett grundläggande krav att fotokatalysatorn har ett inre energigap, som definieras som energiförskjutningen mellan det sista besatta tillståndet av en elektron och det första tillståndet som är tillgänglig att besättas, det ska vara mindre eller jämförbart med den infallande fotonenergin. Med andra ord bör solljusenergin vara tillräcklig för att ta bort elektroner från materialet som vidare överförs till protonen för att bilda en vätefotokatalysatorbindning. Detta är faktiskt den grundläggande mekanismen från solceller, men de fotoexciterade elektronerna används för att producera elektricitet i detta fall. Som ett ytterligare steg

bör de bundna väteatomerna kombineras ihop för att frigöra det molekylära bränslet. Tidigare studier vid universitetet i Tokyo har visat titandioxid(TiO_2) som ett pionjärmaterial för att fotokatalysera den så kallade vattendelningen utan att tillämpa en extern potential, men kolbaserade material har representerat ett ytterligare framsteg på området för att kombinera lågt pris med jordens överflöd av dess utgörande element. Som ett viktigt exempel har polymert kolnitrid ($\text{g-C}_3\text{N}_4$) intensivt undersökts för väteproduktion och koldioxid-omvandling. Dessutom har en överlägsen prestanda funnits för bensotiadiazolbaserade polymerer med en givar-acceptorarkitektur som har en nyckelroll för förbättring av laddningsöverföring och separationsprocesser i dessa material. I allmänhet kännetecknas dessa material av ordning på nanonivå även om själva materialet är amorf.

I denna avhandling har en serie fluoren- och bensotiadiazolbaserade polymerer med givar-acceptorarkitektur utvärderats med hjälp av täthetsfunktionalteori-(DFT) och tidsberoende täthetsfunktionalteori-(TD-DFT) metoder som potentiella kandidater för fotokatalytisk väteproduktion. En uppsättning små molekyler med väl definierad molekylvikt har också beaktats för denna tillämpning. DFT/TD-DFT är ett beräkningsverktyg som har använts allmänt av forskare för att reproducera/förutsäga experimentella resultat för optiska och termodynamiska egenskaper, men också den fotokatalytiska effektiviteten i fast tillstånd eller molekylära material genom att använda de så kallade deskriptorerna. Här har intensiteten av den kemiska bindningen mellan väteatomen och fotokatalysatorn, såväl som excitonbindande energier, som bestämmer om den fotoexciterade elektronen kommer att utföra den kemiska reaktionen eller helt enkelt återgå till det ursprungliga tillståndet, använts som deskriptor för att bestämma tillämpningen av de nämnda materialen i fotokatalytisk väteproduktion. I allmänhet har kemiska modifieringar av dessa material möjliggjort en förbättring av absorptionsområdet i benso(triazol-tiadiazol)baserade polymerer och cyklopentaditiofenbaserade polymerer, med en högre påverkan uppvisad genom modifiering av acceptorenheten. Däremot presenterar alla undersökta system katalytisk effekt för protonreduktion eller borttagning av ett lämpligt kandidat. I synnerhet visades den aktiva roll som kväveatomer spelade från acceptorenheterna i hydreringsprocessen, som fungerar som de katalytiska platser för vätebindning. Dessutom ses en bättre laddningsseparation för cyklopentaditiofenbaserade polymerer en innehållande bensotiadiazolenhet som förväntas leda till en högre fotokatalytisk effektivitet för dessa material.

I ett annat tillvägagångssätt för att hantera det ovannämnda miljöproblemet har det betraktats som direkt omvandling av koldioxid till myrsyra, en viktig kemikalie som hittar tillämpningar i bränsleceller, medicin och matindustrier. Detta är en process med flera steg som också kräver användning av en lämplig foto- eller elektrokatalysator för att minska de kinetiska barriärerna för reaktion. I denna avhandling har Sn-baserade material och Ru-komplex använts

som elektrokatalysatorer för att genomföra koldioxid-omvandlingen till myrsyra genom att lägga på en extern potential. I det tidigare fallet stöder resultaten reaktionsmekanismen där koldioxid införs i Sn-OH-bindningen innan reduktionsprocessen som leder till myrsyraproduktion. I detta steg uppvisar den beräknade reduktions- potentialen ett gott överensstämmande med de mätningar som utförs av våra medarbetare, vilket bekräftar giltigheten för de teoretiska metoder som vi har använt. I ett Ru-komplex kommer reaktionsmekanismen sannolikt att följa vägen med naturlig produktion av kolmonoxid på grund av ligandfrisättning efter den första reduktionsprocessen, som ytterligare protoneras för att originera den aktiva arten. I detta fall kommer koldioxidinsättningen att ske vid Ru-H-bindningen för att generera en kolbunden mellanprodukt som är ytterligare protonerad för att frisätta myrsyra. Slutligen har det studerats den fysiska adsorptionen av koldioxid i metallorganiska ramverk med ett varierande metalliskt centrum i en teoretisk synvinkel.

Acknowledgments

First of all, I would like to thank God for guiding me through this long path-way to fulfill my dreams.

To my supervisors Rajeev Ahuja and C. Moyses Araujo, for the opportunity to work at their research group. I am thankful for the guidance throughout these years, particularly helping me to enhance my scientific writing skills and the ability for listening external suggestions as a part of the work development. Furthermore, it would *not* be possible to build a solid knowledge basis in the theme without the discussions, meetings and even classes that were held by you. I also praise for the impressive professionalism that this work has been conducted since the very first day.

To Luciano Tavares, for all the incentive and project writing that has enabled me to get the scholarship for the PhD studies at Uppsala University, along with my current supervisors. I am grateful for your scientific contributions, advices and the friendship we have built since the master times.

To the collaborator Cleber Marchiori for the co-supervision in several projects, as well as for the friendship built since the beginning of our project on Polymeric materials. I will certainly miss the fika times that included long and good discussions about donor-acceptor polymers.

To Fabio H. Lima for receiving me well in his research group for the development of our collaborative work. I am very proud of the final article that we have written.

To Caetano Miranda and Aline. I have learned a lot about solid-state calculations during my short visit in the University of São Paulo.

To Haining Tian for giving me the opportunity to join the project on Polymeric Materials. I was great to work in our collaborative project.

To the colleagues in this department and friendships that I have built during this time: Ernane, Henrik, Claudia, Mailing Berwanger, Roseli, Mariam, Ageu, William Espinoza, Emel, Rabab, Ricardo, Caroline, Debora, Ivan, Raghuveer, Niklas, Rafael, Xiaoyong. It was nice to have you here.

To my unconditional friend Pamela Svensson. You are the best office mate one can have.

To Juan David Jaramillo for the wonderful friendship since the very first month in Uppsala. I miss all laughs and conversations from the golden times.

To my dear friend Mahsa Ebadi for all sharings, fikas and scientific discussions in more than four years of friendship. Your kindness and patience are an inspiration to me.

To my friend Rodrigo de Carvalho for the scientific help and support when I needed. It has been nice all singing and fikas during the last year. To Jose Luis for all the help you have provided throughout the years.

To John Wörnå for the friendship and technical assistance with the Swedish language in this thesis.

To my mother Noene Damas for being the most wonderful person that I have ever met. Your support has been essential to help me getting through this arduous time. To my lovely brother Ruan Oliveira for always giving me reasons to smile. Unfortunately, my dear father João Damas (*in memoriam*) cannot see this important moment in my life, but I am certain he would be happy and proud of the daughter he has raised.

To David Karlsson, for being such a lovely soul. I am very thankful for having you in my life since the beginning of my PhD studies in Sweden. Having a balanced professional and personal life is something that I am still trying to learn with you. To our little cats Maya and Eddie for giving me so many reasons to be happy in my everyday life when I thought I could not anymore.

To my extended Brazilian family that have always given support during my entire life: Ieda, Rovilson, Perciliana, Levita, Vera (*in mem.*), Maria Fernanda, Leonardo, Samuel, Tania, Vitor (*in mem.*), Pedro, Adriana. To my lovely grandmother Benvinda L. Vilaça (*in mem.*), your love and dedication to the family have certainly influenced how close we all are to each other. It is really hard to express how important you have always been to me.

My special thanks to aunt Leontina for being such an amazing person that I love so much. It is nice to remember that the consciousness about my individual role on planet conservation was introduced by you during my childhood. I have learned so much with you! I also thank my cousin Afrânio Damas for being so helpful and present in several important moments of this journey.

To my dear cousin Francielly Damas, the big sister I did not have. Thank you very much for all the support in my whole life. You are an inspiration to me!

To my grandmother Neusa Silva and my lovely aunts Glaucia and Fabiana Silva. I also thank my cousins Giselly Silva, Guilherme Bueno and Renata Prado for the support.

To my dear friends Patricia, Vanessa, Cristiana and Cristiane Takahashi, Fabiane, Newkelly and Cinthia. I am grateful for having your friendship for all these years!

To everybody else that has dedicated the time to help me, provide advice or, simply, to listen when I needed.

References

- (1) Barber, J. Photosynthetic Energy Conversion: Natural and Artificial. *Chem. Soc. Rev.* **2009**, 38 (1), 185–196.
- (2) WMO. WMO Greenhouse Gas Bulletin | World Meteorological Organization. *WMO Bull.* **2016**, 2015, 1–4.
- (3) Ren, Y.; Sun, D.; Cao, Y.; Tsao, H. N.; Yuan, Y.; Zakeeruddin, S. M.; Wang, P.; Grätzel, M. A Stable Blue Photosensitizer for Color Palette of Dye-Sensitized Solar Cells Reaching 12.6% Efficiency. *J. Am. Chem. Soc.* **2018**, 140 (7), 2405–2408.
- (4) Sonar, P.; Fong Lim, J. P.; Chan, K. L. Organic Non-Fullerene Acceptors for Organic Photovoltaics. *Energy Environ. Sci.* **2011**, 4 (5), 1558.
- (5) Tress, W. Maximum Efficiency and Open-Circuit Voltage of Perovskite Solar Cells. In *Organic-Inorganic Halide Perovskite Photovoltaics*, **2016**, 79–105.
- (6) Buonomano, A.; Calise, F.; Palombo, A. Solar Heating and Cooling Systems by Absorption and Adsorption Chillers Driven by Stationary and Concentrating Photovoltaic/thermal Solar Collectors: Modelling and Simulation. *Renew. Sustain. Energy Rev.* **2018**, 82, 1874–1908.
- (7) Manfredi, N.; Monai, M.; Montini, T.; Peri, F.; De Angelis, F.; Fornasiero, P.; Abboto, A. Dye-Sensitized Photocatalytic Hydrogen Generation: Efficiency Enhancement by Organic Photosensitizer-Coadsorbent Intermolecular Interaction. *ACS Energy Lett.* **2018**, 3 (1).
- (8) Pati, P. B.; Damas, G.; Tian, L.; Fernandes, D. L. A.; Zhang, L.; Pehlivan, I. B.; Edvinsson, T.; Araujo, C. M.; Tian, H. An Experimental and Theoretical Study of an Efficient Polymer Nano-Photocatalyst for Hydrogen Evolution. *Energy Environ. Sci.* **2017**, 10 (6), 1372–1376.
- (9) Queyriaux, N.; Giannoudis, E.; Windle, C. D.; Roy, S.; Pécaut, J.; Coutsolelos, A. G.; Artero, V.; Chavarot-Kerlidou, M. A Noble Metal-Free Photocatalytic System Based on a Novel Cobalt Tetrapyrrolyl Catalyst for Hydrogen Production in Fully Aqueous Medium. *Sustain. Energy Fuels* **2018**, 2, 553–557.
- (10) Roy, S. C.; Varghese, O. K.; Paulose, M.; Grimes, C. A. Toward Solar Fuels: Photocatalytic Conversion of Carbon Dioxide to Hydrocarbons. *ACS Nano*. **2010**, 4 (3), 1259–1278.

- (11) Montoya, J. H.; Seitz, L. C.; Chakthranont, P.; Vojvodic, A.; Jaramillo, T. F.; Nørskov, J. K. Materials for Solar Fuels and Chemicals. *Nat. Mater.* **2016**, *16* (1), 70–81.
- (12) Gupta, R. B. *Hydrogen Fuel: Production, Transport, and Storage*; **2009**.
- (13) Crabtree, G. W.; Dresselhaus, M. S.; Buchanan, M. V. The Hydrogen Economy. *Physics Today*. **2004**, *57* (12), 39–44.
- (14) Isidro-Ortega, F. J.; Pacheco-Sánchez, J. H.; Desales-Guzmán, L. A. Hydrogen Storage on Lithium Decorated Zeolite Templated Carbon, DFT Study. *Int. J. Hydrogen Energy* **2017**, *42* (52), 30704–30717.
- (15) Sergio, T. The Absolute Redox Potential : An Explanatory Note. *Pure Appl. Chem* **1986**, *58* (7), 955–966.
- (16) Li, H.; Tsai, C.; Koh, A. L.; Cai, L.; Contryman, A. W.; Fragapane, A. H.; Zhao, J.; Han, H. S.; Manoharan, H. C.; Abild-Pedersen, F.; et al. Activating and Optimizing MoS₂ basal Planes for Hydrogen Evolution through the Formation of Strained Sulphur Vacancies. *Nat. Mater.* **2016**, *15* (1), 48–53.
- (17) Liu, H.; Yuan, J.; Shangguan, W. Photochemical Reduction and Oxidation of Water Including Sacrificial Reagents and Pt/TiO₂ Catalyst. *Energy and Fuels* **2006**, *20* (6), 2289–2292.
- (18) Maeda, K.; Domen, K. Photocatalytic Water Splitting: Recent Progress and Future Challenges. *J. Phys. Chem. Lett.* **2010**, *1* (18), 2655–2661.
- (19) Damas, G. B.; Marchiori, C. F. N.; Araujo, C. M. Tailoring the Electron-Rich Moiety in Benzothiadiazole-Based Polymers for Efficient Photocatalytic Hydrogen Evolution Reaction. *J. Phys. Chem. C* **2019**, *123* (42), 25531–25542.
- (20) Zhu, L.; Yi, Y.; Wei, Z. Exciton Binding Energies of Nonfullerene Small Molecule Acceptors: Implication for Exciton Dissociation Driving Forces in Organic Solar Cells. *J. Phys. Chem. C* **2018**, *122* (39), 22309–22316.
- (21) Pellegrin, Y.; Odobel, F. Sacrificial Electron Donor Reagents for Solar Fuel Production. *Comptes Rendus Chim.* **2017**, *20* (3), 283–295.
- (22) Schwab, M. G.; Hamburger, M.; Feng, X.; Shu, J.; Spiess, H. W.; Wang, X.; Antonietti, M.; Müllen, K. Photocatalytic Hydrogen Evolution through Fully Conjugated Poly(azomethine) Networks. *Chem. Commun.* **2010**, *46* (47), 8932.
- (23) Du, P.; Eisenberg, R. Catalysts Made of Earth-Abundant Elements (Co, Ni, Fe) for Water Splitting: Recent Progress and Future Challenges. *Energy Environ. Sci.* **2012**, *5* (3), 6012.
- (24) Xie, A.; Zhu, J.; Luo, G. G. Efficient Electrocatalytic and Photocatalytic Hydrogen Evolution Using a Linear Trimeric Thiolato Complex of Nickel. *Int. J. Hydrogen Energy* **2018**, *43* (5), 2772–2780.

- (25) Fateeva, A.; Chater, P. A.; Ireland, C. P.; Tahir, A. A.; Khimyak, Y. Z.; Wiper, P. V.; Darwent, J. R.; Rosseinsky, M. J. A Water-Stable Porphyrin-Based Metal-Organic Framework Active for Visible-Light Photocatalysis. *Angew. Chemie - Int. Ed.* **2012**, *51* (30), 7440–7444.
- (26) Tso, S.; Li, W. S.; Wu, B. H.; Chen, L. J. Enhanced H₂ production in Water Splitting with CdS-ZnO Core-Shell Nanowires. *Nano Energy* **2018**, *43*, 270–277.
- (27) Zou, X.; Zhang, Y. Noble Metal-Free Hydrogen Evolution Catalysts for Water Splitting. *Chem. Soc. Rev.* **2015**, *44* (15), 5148–5180.
- (28) Fujishima, A.; Rao, T. N.; Tryk, D. A. Titanium Dioxide Photocatalysis. *J. Photochem. Photobiol. C Photochem. Rev.* **2000**, *1* (1), 1–21.
- (29) Wang, Y.-F.; Li, J.-W.; Hou, Y.-F.; Yu, X.-Y.; Su, C.-Y.; Kuang, D.-B. Hierarchical Tin Oxide Octahedra for Highly Efficient Dye-Sensitized Solar Cells. *Chemistry* **2010**, *16* (29), 8620–8625.
- (30) Youngblood, W. J.; Lee, S.-H. A.; Maeda, K.; Mallouk, T. E. Visible Light Water Splitting Using Dye-Sensitized Oxide Semiconductors. *Acc. Chem. Res.* **2009**, *42* (12), 1966–1973.
- (31) Jaafar, S. N. H.; Minggu, L. J.; Arifin, K.; Kassim, M. B.; Wan, W. R. D. Natural Dyes as TiO₂ Sensitizers with Membranes for Photoelectrochemical Water Splitting: An Overview. *Renew. Sustain. Energy Rev.* **2017**, *78*, 698–709.
- (32) Fujishima, A. Hydrogen Production under Sunlight with an Electrochemical Photocell. *J. Electrochem. Soc.* **1975**, *122* (11), 1487.
- (33) Li, C.; Yuan, J.; Han, B.; Jiang, L.; Shanguan, W. TiO₂ Nanotubes Incorporated with CdS for Photocatalytic Hydrogen Production from Splitting Water under Visible Light Irradiation. In *International Journal of Hydrogen Energy* **2010**, *35*, 7073–7079.
- (34) Zhang, Z.; Hossain, M. F.; Takahashi, T. Photoelectrochemical Water Splitting on Highly Smooth and Ordered TiO₂ Nanotube Arrays for Hydrogen Generation. *Int. J. Hydrogen Energy* **2010**, *35* (16), 8528–8535.
- (35) Park, J. H.; Kim, S.; Bard, A. J. Novel Carbon-Doped TiO₂ Nanotube Arrays with High Aspect Ratios for Efficient Solar Water Splitting. *Nano Lett.* **2006**, *6* (1), 24–28.
- (36) Li, Z.; Ding, D.; Liu, Q.; Ning, C.; Wang, X. Ni-Doped TiO₂ Nanotubes for Wide-Range Hydrogen Sensing. *Nanoscale Res. Lett.* **2014**, *9* (1), 118.
- (37) de Brito, J. F.; Tavella, F.; Genovese, C.; Ampelli, C.; Zandoni, M. V. B.; Centi, G.; Perathoner, S. Role of CuO in the Modification of the Photocatalytic Water Splitting Behavior of TiO₂ nanotube Thin Films. *Appl. Catal. B Environ.* **2018**, *224*, 136–145.

- (38) Hwang, D. W.; Kim, J.; Park, T. J.; Lee, J. S. Mg-Doped WO₃ as a Novel Photocatalyst for Visible Light-Induced Water Splitting. *Catal. Letters* **2002**, *80* (1–2), 53–57.
- (39) Wang, F.; Di Valentin, C.; Pacchioni, G. Doping of WO₃ for Photocatalytic Water Splitting: Hints from Density Functional Theory. *J Phys Chem C* **2012**, *116* (16), 8901–8909.
- (40) Li, W.; Li, J.; Wang, X.; Chen, Q. Preparation and Water-Splitting Photocatalytic Behavior of S-Doped WO₃. *Appl. Surf. Sci.* **2012**, *263*, 157–162.
- (41) Govatsi, K.; Seferlis, A.; Neophytides, S. G.; Yannopoulos, S. N. Influence of the Morphology of ZnO Nanowires on the Photoelectrochemical Water Splitting Efficiency. *Int. J. Hydrogen Energy* **2018**.
- (42) Lim, Y.-F.; Chua, C. S.; Lee, C. J. J.; Chi, D. Sol–gel Deposited Cu₂O and CuO Thin Films for Photocatalytic Water Splitting. *Phys. Chem. Chem. Phys.* **2014**, *16* (47), 25928–25934.
- (43) Reshak, A. H. Sulfide Oxide XZnSO (X = Ca or Sr) as Novel Active Photocatalytic Water Splitting Solar-to-Hydrogen Energy Conversion. *Appl. Catal. B Environ.* **2018**, *225*, 273–283.
- (44) Wen, J.; Xie, J.; Chen, X.; Li, X. A Review on G-C₃N₄-Based Photocatalysts. *Appl. Surf. Sci.* **2017**, *391*, 72–123.
- (45) Ye, S.; Wang, R.; Wu, M.-Z.; Yuan, Y.-P. A Review on G-C₃N₄ for Photocatalytic Water Splitting and CO₂ Reduction. *Appl. Surf. Sci.* **2015**, *358*, 1–13.
- (46) Seza, A.; Soleimani, F.; Naseri, N.; Soltaninejad, M.; Montazeri, S. M.; Sadrnezhaad, S. K.; Mohammadi, M. R.; Moghadam, H. A.; Forouzandeh, M.; Amin, M. H. Novel Microwave-Assisted Synthesis of Porous G-C₃N₄/SnO₂ nanocomposite for Solar Water-Splitting. *Appl. Surf. Sci.* **2018**, *440*, 153–161.
- (47) Shen, B.; Hong, Z.; Chen, Y.; Lin, B.; Gao, B. Template-Free Synthesis of a Novel Porous G-C₃N₄ with 3D Hierarchical Structure for Enhanced Photocatalytic H₂ Evolution. *Mater. Lett.* **2014**, *118*, 208–211.
- (48) She, X. J.; Liu, L.; Ji, H. Y.; Mo, Z.; Li, Y. P.; Huang, L. Y.; Du, D. L.; Xu, H.; Li, H. M. Template-Free Synthesis of 2D Porous Ultrathin Nonmetal-Doped G-C₃N₄ Nanosheets with Highly Efficient Photocatalytic H₂ Evolution from Water under Visible Light. *Appl. Catal. B-Environmental* **2016**, *187*, 144–153.
- (49) Sun, Z.; Wang, H.; Wu, Z.; Wang, L. G-C₃N₄ Based Composite Photocatalysts for Photocatalytic CO₂ Reduction. *Catal. Today* **2017**, *300*, 160–172.
- (50) Cao, Y.; Xing, Z.; Li, Z.; Wu, X.; Hu, M.; Yan, X.; Zhu, Q.; Yang, S.; Zhou, W. Mesoporous Black TiO₂-x/Ag Nanospheres Coupled with G-C₃N₄ nanosheets as 3D/2D Ternary Heterojunctions Visible Light Photocatalysts. *J. Hazard. Mater.* **2018**, *343*, 181–190.

- (51) Zhou, S.; Liu, Y.; Li, J.; Wang, Y.; Jiang, G.; Zhao, Z.; Wang, D.; Duan, A.; Liu, J.; Wei, Y. Facile in Situ Synthesis of Graphitic Carbon Nitride (G-C₃N₄)-N-TiO₂ Heterojunction as an Efficient Photocatalyst for the Selective Photoreduction of CO₂ to CO. *Appl. Catal. B Environ.* **2014**, *158–159*, 20–29.
- (52) Kang, Y.; Yang, Y.; Yin, L. C.; Kang, X.; Liu, G.; Cheng, H. M. An Amorphous Carbon Nitride Photocatalyst with Greatly Extended Visible-Light-Responsive Range for Photocatalytic Hydrogen Generation. *Adv. Mater.* **2015**, *27* (31), 4572–4577.
- (53) Zhang, G.; Lan, Z.-A.; Lin, L.; Lin, S.; Wang, X. Overall Water Splitting by Pt/g-C₃N₄ Photocatalysts without Using Sacrificial Agents. *Chem. Sci.* **2016**, *7*, 3062–3066.
- (54) Li, X.; Bi, W.; Zhang, L.; Tao, S.; Chu, W.; Zhang, Q.; Luo, Y.; Wu, C.; Xie, Y. Single-Atom Pt as Co-Catalyst for Enhanced Photocatalytic H₂ Evolution. *Adv. Mater.* **2016**, *28* (12), 2427–2431.
- (55) Indra, A.; Menezes, P. W.; Kailasam, K.; Hollmann, D.; Schröder, M.; Thomas, A.; Brückner, A.; Driess, M. Nickel as a Co-Catalyst for Photocatalytic Hydrogen Evolution on Graphitic-Carbon Nitride (Sg-CN): What Is the Nature of the Active Species? *Chem. Commun.* **2016**, *52* (1), 104–107.
- (56) Liu, J.; Jia, Q.; Long, J.; Wang, X.; Gao, Z.; Gu, Q. Amorphous NiO as Co-Catalyst for Enhanced Visible-Light-Driven Hydrogen Generation over G-C₃N₄ photocatalyst. *Appl. Catal. B Environ.* **2018**, *222*, 35–43.
- (57) Park, J. H.; Ko, K. C.; Park, N.; Shin, H.-W.; Kim, E.; Kang, N.; Hong Ko, J.; Lee, S. M.; Kim, H. J.; Ahn, T. K.; et al. Microporous Organic Nanorods with Electronic Push–pull Skeletons for Visible Light-Induced Hydrogen Evolution from Water. *J. Mater. Chem. A* **2014**, *2* (21), 7656.
- (58) Yang, C.; Ma, B. C.; Zhang, L.; Lin, S.; Ghasimi, S.; Landfester, K.; Zhang, K. A. I.; Wang, X. Molecular Engineering of Conjugated Polybenzothiadiazoles for Enhanced Hydrogen Production by Photosynthesis. *Angew. Chemie - Int. Ed.* **2016**, *55* (32), 9202–9206.
- (59) Sick, T.; Hufnagel, A. G.; Kampmann, J.; Kondofersky, I.; Calik, M.; Rotter, J. M.; Evans, A.; Döblinger, M.; Herbert, S.; Peters, K.; et al. Oriented Films of Conjugated 2D Covalent Organic Frameworks as Photocathodes for Water Splitting. *J. Am. Chem. Soc.* **2018**, *140* (6), 2085–2092.
- (60) Sprick, R. S.; Jiang, J. X.; Bonillo, B.; Ren, S.; Ratvijitvech, T.; Guiglion, P.; Zijnenburg, M. A.; Adams, D. J.; Cooper, A. I. Tunable Organic Photocatalysts for Visible-Light-Driven Hydrogen Evolution. *J. Am. Chem. Soc.* **2015**, *137* (9), 3265–3270.
- (61) Woods, D. J.; Sprick, R. S.; Smith, C. L.; Cowan, A. J.; Cooper, A. I. A Solution-Processable Polymer Photocatalyst for Hydrogen Evolution from Water. *Adv. Energy Mater.* **2017**, *7* (22), 1700479

- (62) Grimme, S.; Antony, J.; Ehrlich, S.; Krieg, H. A Consistent and Accurate Ab Initio Parametrization of Density Functional Dispersion Correction (DFT-D) for the 94 Elements H-Pu. *J. Chem. Phys.* **2010**, *132* (15), 154104.
- (63) Frisch, M. J. et al. Gaussian 09, Revision D.01. *Gaussian 09, Revision D.01. Gaussian, Inc., Wallingford CT*,. 2009.
- (64) Frisch, M. J.; Trucks, G. W.; Schlegel, H. E.; Scuseria, G. E.; Robb, M. A.; Cheeseman, J. R.; Scalmani, G.; Barone, V.; Petersson, G. A.; O., F.; et al. Gaussian 16. *Gaussian, Inc., Wallingford CT*,. 2016.
- (65) Kresse, G.; Marsman, M.; Furthmüller, J. Vienna Ab-Initio Package Vienna Simulation: VASP the GUIDE. *VASP Man.* **2014**, 237.
- (66) Hohenberg, P.; Kohn, W. Inhomogeneous Electron Gas. *Phys. Rev.* **1964**, *136* (3B), B864.
- (67) Kohn, W.; Sham, L. J. Self-Consistent Equations Including Exchange and Correlation Effects. *Phys. Rev.* **1965**, *140* (4A), A1133.
- (68) Koch, W.; Holthausen, M. C. *Wolfram Koch , Max C . Holthausen A Chemist ' S Guide to Density Functional Theory*; 2001; Vol. 3.
- (69) Frau, J.; Muñoz, F.; Glossma-Mitnik, D. A Molecular Electron Density Theory Study of the Chemical Reactivity of Cis- and Trans-Resveratrol. *Molecules* **2016**, *21* (12), 1650.
- (70) Frau, J.; Muñoz, F.; Glossman-Mitnik, D. Application of DFT Concepts to the Study of the Chemical Reactivity of Some Resveratrol Derivatives through the Assessment of the Validity of The “koopmans in DFT” (KID) Procedure. *J. Theor. Comput. Chem.* **2017**, *16* (1), 1750006.
- (71) Perdew, J. P.; Ernzerhof, M.; Burke, K. Generalized Gradient Approximation Made Simple. *Phys. Rev. Lett.* **1996**, *77*, 3865–3868.
- (72) Arbuznikov, A. V. Hybrid Exchange Correlation Functionals and Potentials: Concept Elaboration. *J. Struct. Chem.* **2007**, *48* (SUPPL. 1), S1-S131.
- (73) Heyd, J.; Scuseria, G. E.; Ernzerhof, M. Hybrid Functionals Based on a Screened Coulomb Potential. *J. Chem. Phys.* **2003**, *118* (18), 8207–8215.
- (74) Becke, A. B3LYP. *J. Chem. Phys.* **1993**, *98*, 5648–5652.
- (75) McCormick, T. M.; Bridges, C. R.; Carrera, E. I.; Dicarmine, P. M.; Gibson, G. L.; Hollinger, J.; Kozycz, L. M.; Seferos, D. S. Conjugated Polymers: Evaluating DFT Methods for More Accurate Orbital Energy Modeling. *Macromolecules* **2013**, *46* (10), 3879–3886.
- (76) Yanai, T.; Tew, D. P.; Handy, N. C. A New Hybrid Exchange-Correlation Functional Using the Coulomb-Attenuating Method (CAM-B3LYP). *Chem. Phys. Lett.* **2004**, *393* (1–3), 51–57.

- (77) Zhao, Y.; Truhlar, D. G. The M06 Suite of Density Functionals for Main Group Thermochemistry, Thermochemical Kinetics, Noncovalent Interactions, Excited States, and Transition Elements: Two New Functionals and Systematic Testing of Four M06-Class Functionals and 12 Other Function. *Theor. Chem. Acc.* **2008**, *120* (1–3), 215–241.
- (78) Stephens, P. J.; Devlin, F. J.; Chabalowski, C. F.; Frisch, M. J. Ab Initio Calculation of Vibrational Absorption and Circular Dichroism Spectra Using Density Functional Force Fields. *J. Phys. Chem.* **1994**, *98* (45), 11623–11627.
- (79) Van Voorhis, T.; Scuseria, G. E. A Novel Form for the Exchange-Correlation Energy Functional. *J. Chem. Phys.* **1998**, *109* (2), 400–410.
- (80) McLean, A. D.; Chandler, G. S. Contracted Gaussian-Basis Sets for Molecular Calculations. 1. 2nd Row Atoms, Z=11-18,. *J. Chem. Phys.* **1980**, *72*, 5639–5648.
- (81) Roos, B.; Veillard, A.; Vinot, G. Gaussian Basis Sets for Molecular Wavefunctions Containing Third-Row Atoms. *Theor. Chim. Acta* **1971**, *20* (1), 1–11.
- (82) Krishnan, R.; Binkley, J. S.; Seeger, R.; Pople, J. A. Self-Consistent Molecular Orbital Methods. XX. A Basis Set for Correlated Wave Functions. *J. Chem. Phys.* **1980**, *72* (1), 650–654.
- (83) Blaudeau, J.-P.; McGrath, M. P. Extension of Gaussian-2 (G2) Theory to Molecules Containing Third-Row Atoms K and Ca. *J. Chem. Phys.* **1997**, *107* (13), 5016.
- (84) Johnson, E. Cohesion in Metals. *Nucl. Instruments Methods Phys. Res. Sect. B Beam Interact. with Mater. Atoms* **1989**, *42* (3), 403.
- (85) Adamo, C.; Jacquemin, D. The Calculations of Excited-State Properties with Time-Dependent Density Functional Theory. *Chem. Soc. Rev.* **2013**, *42* (3), 845–856.
- (86) Laurent, A. D.; Adamo, C.; Jacquemin, D. Dye Chemistry with Time-Dependent Density Functional Theory. *Phys. Chem. Chem. Phys.* **2014**, *16* (28), 14334–14356.
- (87) Marques, M. a L.; Maitra, N.; Nogueira, F. Fundamentals of Time-Dependent Density Functional Theory. *Spectroscopy* **2012**, *837* (1), 559.
- (88) Bauernschmitt, R.; Ahlrichs, R. Treatment of Electronic Excitations within the Adiabatic Approximation of Time Dependent Density Functional Theory. *Chem. Phys. Lett.* **1996**, *256* (4–5), 454–464.
- (89) Casida, M. E.; Jamorski, C.; Casida, K. C.; Salahub, D. R. Molecular Excitation Energies to High-Lying Bound States from Time-Dependent density- Functional response theory: Characterization and Correction of the time-Dependent local Density approximation Ionization Threshold Mark. *J. Chem. Phys.* **1998**, *108* (11), 4439.

- (90) Sato, Y.; Kajii, H.; Ohmori, Y. Improved Performance of Polymer Photodetectors Using Indium-Tin-Oxide Modified by Phosphonic Acid-Based Self-Assembled Monolayer Treatment. *Org. Electron. physics, Mater. Appl.* **2014**, *15* (8), 1753–1758.
- (91) Mosquera, M. A.; Chen, L. X.; Ratner, M. A.; Schatz, G. C. Sequential Double Excitations from Linear-Response Time-Dependent Density Functional Theory. *J. Chem. Phys.* **2016**, *144* (20).
- (92) Damas, G.; Marchiori, C. F. N.; Araujo, C. M. On the Design of Donor-Acceptor Conjugated Polymers for Photocatalytic Hydrogen Evolution Reaction: First-Principles Theory-Based Assessment. *J. Phys. Chem. C* **2018**, *122* (47), 26876–26888.
- (93) Olle, I.; Fengling, Z.; Andersson, M. R. Alternating Polyfluorenes Collect Solar Light in Polymer Photovoltaics. *Acc. Chem. Res.* **2009**, *42* (11), 1731–1739.
- (94) Zhang, M.; Guo, X.; Li, Y. Photovoltaic Performance Improvement of D-A Copolymers Containing Bithiazole Acceptor Unit by Using Bithiophene Bridges. *Macromol.* **2011**, *44* (22), 8798–8804.
- (95) Li, Z.; Huo, L.; Guo, X.; Yong, W.; Zhang, S.; Fan, H. Synthesis and Photovoltaic Properties of D- π -A Copolymers Based on thieno[3,2-B]thiophene Bridge Unit. *Polym. (United Kingdom)* **2013**, *54* (22), 6150–6157.
- (96) Moan, J. Visible Light and UV Radiation. *Radiat. home, outdoors Work.* **2001**, 69–85.
- (97) Gorog, S. *Ultraviolet-Visible Spectrophotometry in Pharmaceutical Analysis*; 1995.
- (98) Pati, P. B.; Damas, G.; Tian, L.; Fernandes, D. L. A.; Zhang, L.; Pehlivan, I. B.; Edvinsson, T.; Araujo, C. M.; Tian, H. An Experimental and Theoretical Study of an Efficient Polymer Nano-Photocatalyst for Hydrogen Evolution. *Energy Environ. Sci.* **2017**, *10* (6), 1372–1376.
- (99) Guiglion, P.; Butchosa, C.; Zwiijnenburg, M. A. Polymeric Watersplitting Photocatalysts; A Computational Perspective on the Water Oxidation Conundrum. *J. Mat. Chem. A.* 2014, pp 11996–12004.
- (100) Sprick, R. S.; Wilbraham, L.; Bai, Y.; Guiglion, P.; Monti, A.; Clowes, R.; Cooper, A. I.; Zwiijnenburg, M. A. Nitrogen Containing Linear Poly(phenylene) Derivatives for Photo-Catalytic Hydrogen Evolution from Water. *Chem. Mater.* **2018**, *30* (16), 5733–5742.
- (101) Bredas, J.-L. Mind the Gap! *Mater. Horiz.* **2014**, *1* (1), 17–19.
- (102) Guiglion, P.; Butchosa, C.; Zwiijnenburg, M. A. Polymer Photocatalysts for Water Splitting: Insights from Computational Modeling. *Macromol. Chem. Phys.* **2016**, *217* (3), 344–353.

- (103) Rienstra-Kiracofe, J. C.; Tschumper, G. S.; Schaefer, H. F.; Nandi, S.; Ellison, G. B. Atomic and Molecular Electron Affinities: Photoelectron Experiments and Theoretical Computations. *Chem. Rev.* **2002**, *102* (1), 231–282.
- (104) Hou, Q.; Xu, Y.; Yang, W.; Yuan, M.; Peng, J.; Cao, Y. Novel Red-Emitting Fluorene-Based Copolymers. *J. Mater. Chem.* **2002**, *12* (10), 2887–2892.
- (105) Jespersen, K. G.; Beenken, W. J. D.; Zaushitsyn, Y.; Yartsev, A.; Andersson, M.; Pullerits, T.; Sundström, V. The Electronic States of Polyfluorene Copolymers with Alternating Donor-Acceptor Units. *J. Chem. Phys.* **2004**, *121* (24), 12613–12617.
- (106) Zhang, S.; Guo, Y.; Fan, H.; Liu, Y.; Chen, H. Y.; Yang, G.; Zhan, X.; Liu, Y.; Li, Y.; Yang, Y. Low Bandgap π -Conjugated Copolymers Based on Fused Thiophenes and Benzothiadiazole: Synthesis and Structure-Property Relationship Study. *J. Polym. Sci. Part A Polym. Chem.* **2009**, *47* (20), 5498–5508.
- (107) Gao, J.; Grey, J. K. Spectroscopic Studies of Energy Transfer in Fluorene Co-Polymer Blend Nanoparticles. *Chem. Phys. Lett.* **2012**, *522*, 86–91.
- (108) Gobalasingham, N. S.; Ekiz, S.; Pankow, R. M.; Livi, F.; Bundgaard, E.; Thompson, B. C. Carbazole-Based Copolymers via Direct Arylation Polymerization (DAP) for Suzuki-Convergent Polymer Solar Cell Performance. *Polym. Chem.* **2017**, *8*, 4393–4402.
- (109) Sharma, B.; Alam, F.; Dutta, V.; Jacob, J. Synthesis and Photovoltaic Studies on Novel Fluorene Based Cross-Conjugated Donor-Acceptor Type Polymers. *Org. Electron. physics, Mater. Appl.* **2017**, *40*, 42–50.
- (110) Keshtov, M. L.; Khokhlov, A. R.; Kuklin, S. A.; Osipov, S. A.; Radychev, N. A.; Godovskiy, D. Y.; Konstantinov, I. O.; Sharma, G. D. Synthesis and Photovoltaic Properties Low Bandgap D-A Copolymers Based on Fluorinated Thiadiazoloquinoxaline. *Org. Electron.* **2017**, *43*, 268–276.
- (111) Damas, G.; Marchiori, C. F. N.; Araujo, C. M. G. On the Design of Donor-Acceptor Conjugated Polymers for Photocatalytic Hydrogen Evolution Reaction: First-Principles Theory Based Assessment. *J. Phys. Chem. C* **2018**, *122* (47), 26876–26888.
- (112) Araujo, R. B.; Banerjee, A.; Panigrahi, P.; Yang, L.; Sjödin, M.; Strømme, M.; Araujo, C. M.; Ahuja, R. Assessing the Electrochemical Properties of Polypyridine and Polythiophene for Prospective Applications in Sustainable Organic Batteries. *Phys. Chem. Chem. Phys.* **2017**, *19* (4), 3307–3314.
- (113) Damas, G. B.; Miranda, C. R.; Sgarbi, R.; Portela, J. M.; Camilo, M. R.; Lima, F. H. B.; Araujo, C. M. On the Mechanism of Carbon Dioxide Reduction on Sn-Based Electrodes: Insights into the Role of Oxide Surfaces. *Catalysts* **2019**, *9* (8), 636.

- (114) Tomasi, J.; Mennucci, B.; Cammi, R. Quantum Mechanical Continuum Solvation Models. *Chem. Rev.* **2005**, *105* (8), 2999–3093.
- (115) Ochterski, J. W.; Ph, D. Thermochemistry in Gaussian. *Gaussian Inc Pittsburgh PA* **2000**, *264* (1), 1–19.
- (116) Putungan, D. B.; Lin, S.-H.; Kuo, J.-L. First-Principles Examination of Conducting Monolayer 1T'-MX₂ (M = Mo, W; X = S, Se, Te): Promising Catalysts for Hydrogen Evolution Reaction and Its Enhancement by Strain. *Phys. Chem. Chem. Phys.* **2015**, *17* (33), 21702–21708.
- (117) Hansch, C.; Leo, A.; Taft, R. W. A Survey of Hammett Substituent Constants and Resonance and Field Parameters. *Chem. Rev.* **1991**, *91* (2), 165–195.
- (118) Greeley, J.; Jaramillo, T. F.; Bonde, J.; Chorkendorff, I.; Nørskov, J. K. Computational High-Throughput Screening of Electrocatalytic Materials for Hydrogen Evolution. *Nat. Mater.* **2006**, *5* (11), 909–913.
- (119) Lan, Z. A.; Zhang, G.; Chen, X.; Zhang, Y.; Zhang, K. A. I.; Wang, X. Reducing the Exciton Binding Energy of Donor–Acceptor-Based Conjugated Polymers to Promote Charge-Induced Reactions. *Angew. Chemie - Int. Ed.* **2019**, *58*, 10236–10240.
- (120) Brédas, J. L.; Beljonne, D.; Coropceanu, V.; Cornil, J. Charge-Transfer and Energy-Transfer Processes in π -Conjugated Oligomers and Polymers: A Molecular Picture. *Chem. Rev.* **2004**, *104* (11), 4971–5003.
- (121) Li, H. W.; Guan, Z.; Cheng, Y.; Lui, T.; Yang, Q.; Lee, C. S.; Chen, S.; Tsang, S. W. On the Study of Exciton Binding Energy with Direct Charge Generation in Photovoltaic Polymers. *Adv. Electron. Mater.* **2016**, *2* (11).
- (122) Lee, H.; Jo, H.; Kim, D.; Biswas, S.; Sharma, G. D.; Ko, J. The Effect of Acceptor End Groups on the Physical and Photovoltaic Properties of A- π -D- π -A Type Oligomers with Same S, N-Heteropentacene Central Electron Donor Unit for Solution Processed Organic Solar Cells. *Dye. Pigment.* **2016**, *129*, 209–219.
- (123) Shi, J.; Isakova, A.; Abudulimu, A.; Van Den Berg, M.; Kwon, O. K.; Meixner, A. J.; Park, S. Y.; Zhang, D.; Gierschner, J.; Lüer, L. Designing High Performance All-Small-Molecule Solar Cells with Non-Fullerene Acceptors: Comprehensive Studies on Photoexcitation Dynamics and Charge Separation Kinetics. *Energy Environ. Sci.* **2018**, *11*, 211–220.
- (124) Zhang, G.; Zhao, Y.; Kang, B.; Park, S.; Ruan, J.; Lu, H.; Qiu, L.; Ding, Y.; Cho, K. Fused Heptacyclic-Based Acceptor-Donor-Acceptor Small Molecules: N-Substitution toward High-Performance Solution-Processable Field-Effect Transistors. *Chem. Mater.* **2019**, *31*(6), 2027–2035.

- (125) Wang, Z.; Zhu, L.; Shuai, Z.; Wei, Z. A- π -D- π -A Electron-Donating Small Molecules for Solution-Processed Organic Solar Cells: A Review. *Macromol. Rapid Commun.* **2017**, *38*, 1700470.
- (126) Akbarimoosavi, M.; Rohwer, E.; Rondi, A.; Hankache, J.; Geng, Y.; Decurtins, S.; Hauser, A.; Liu, S.-X.; Feurer, T.; Cannizzo, A. Tunable Lifetimes of Intramolecular Charge-Separated States in Molecular Donor-Acceptor Dyads. *J. Phys. Chem. C* **2019**, *123* (14), 8500–8511.
- (127) Chochos, C. L.; Chávez, P.; Bulut, I.; Lévêque, P.; Spanos, M.; Tatsi, E.; Katsouras, A.; Avgeropoulos, A.; Gregoriou, V. G.; Leclerc, N. Experimental and Theoretical Investigations on the Optical and Electrochemical Properties of π -Conjugated Donor-Acceptor-Donor (DAD) Compounds toward a Universal Model. *J. Chem. Phys.* **2018**, *149* (12), 12902.
- (128) Wang, L.; Rörich, I.; Ramanan, C.; Blom, P. W. M.; Huang, W.; Li, R.; Zhang, K. A. I. Electron Donor-Free Photoredox Catalysis: Via an Electron Transfer Cascade by Cooperative Organic Photocatalysts. *Catal. Sci. Technol.* **2018**, *8* (14), 3539–3547.
- (129) Yadagiri, B.; Narayanaswamy, K.; Srinivasa Rao, R.; Bagui, A.; Datt, R.; Gupta, V.; Singh, S. P. D- π -A- π -D Structured Diketopyrrolopyrrole-Based Electron Donors for Solution-Processed Organic Solar Cells. *ACS Omega* **2018**, *3* (10), 13365–13373.
- (130) Wang, L.; Fernández-Terán, R.; Zhang, L.; Fernandes, D. L. A.; Tian, L.; Chen, H.; Tian, H. Organic Polymer Dots as Photocatalysts for Visible Light-Driven Hydrogen Generation. *Angew. Chemie - Int. Ed.* **2016**, *55* (40), 12306–12310.
- (131) Liu, A.; Tai, C. W.; Holá, K.; Tian, H. Hollow Polymer Dots: Nature-Mimicking Architecture for Efficient Photocatalytic Hydrogen Evolution Reaction. *J. Mater. Chem. A* **2019**, *7*, 4797–4803.
- (132) Baruch, M. F.; Pander, J. E.; White, J. L.; Bocarsly, A. B. Mechanistic Insights into the Reduction of CO₂ on Tin Electrodes Using in Situ ATR-IR Spectroscopy. *ACS Catalysis*. **2015**, *5*(5), 3148–3156.
- (133) Prakash, G. K. S.; Viva, F. A.; Olah, G. A. Electrochemical Reduction of CO₂ over Sn-Nafion® Coated Electrode for a Fuel-Cell-like Device. *J. Power Sources* **2013**, *223*, 68–73.
- (134) Zhang, S.; Kang, P.; Meyer, T. J. Nanostructured Tin Catalysts for Selective Electrochemical Reduction of Carbon Dioxide to Formate. *J. Am. Chem. Soc.* **2014**, *136* (5), 1734–1737.
- (135) Del Castillo, A.; Alvarez-Guerra, M.; Solla-Gullón, J.; Sáez, A.; Montiel, V.; Irabien, A. Sn Nanoparticles on Gas Diffusion Electrodes: Synthesis, Characterization and Use for Continuous CO₂ Electroreduction to Formate. *J. CO₂ Util.* **2017**, *18*.
- (136) Chen, Y.; Kanan, M. W. Tin Oxide Dependence of the CO₂ Reduction Efficiency on Tin Electrodes and Enhanced Activity for Tin/tin Oxide Thin-Film Catalysts. *J. Am. Chem. Soc.* **2012**, *134* (4), 1986–1989.

- (137) Wu, J.; Risalvato, F. G.; Ke, F.-S.; Pellechia, P. J.; Zhou, X.-D. Electrochemical Reduction of Carbon Dioxide I. Effects of the Electrolyte on the Selectivity and Activity with Sn Electrode. *J. Electrochem. Soc.* **2012**, *159* (7), F353–F359.
- (138) Wu, J.; Risalvato, F. G.; Ma, S.; Zhou, X. D. Electrochemical Reduction of Carbon Dioxide III. the Role of Oxide Layer Thickness on the Performance of Sn Electrode in a Full Electrochemical Cell. *J. Mater. Chem. A* **2014**, *2* (6), 1647–1651.
- (139) Walsh, A.; Watson, G. W. Electronic Structures of Rocksalt, Litharge, and Herzenbergite SnO by Density Functional Theory. *Phys. Rev. B - Condens. Matter Mater. Phys.* **2004**, *70* (23), 1–7.
- (140) Zhang, J.; Han, Y.; Liu, C.; Ren, W.; Li, Y.; Wang, Q.; Su, N.; Li, Y.; Ma, B.; Ma, Y.; et al. Electrical Transport Properties of SnO under High Pressure. *J. Phys. Chem. C* **2011**, *115*, 20710.
- (141) Cui, C.; Han, J.; Zhu, X.; Liu, X.; Wang, H.; Mei, D.; Ge, Q. Promotional Effect of Surface Hydroxyls on Electrochemical Reduction of CO₂ over SnOx/Sn Electrode. *J. Catal.* **2016**, *343*, 257–265.
- (142) Vitos, L.; Ruban, A. V.; Skriver, H. L.; Kollár, J. The Surface Energy of Metals. *Surf. Sci.* **1998**, *411* (1–2), 186–202.
- (143) Mathew, K.; Sundararaman, R.; Letchworth-Weaver, K.; Arias, T. A.; Hennig, R. G. Implicit Solvation Model for Density-Functional Study of Nanocrystal Surfaces and Reaction Pathways. *J. Chem. Phys.* **2014**, *140* (8), 084106.
- (144) Bochevarov, A. D.; Harder, E.; Hughes, T. F.; Greenwood, J. R.; Braden, D. A.; Philipp, D. M.; Rinaldo, D.; Halls, M. D.; Zhang, J.; Friesner, R. A. Jaguar: A High-Performance Quantum Chemistry Software Program with Strengths in Life and Materials Sciences. *Int. J. Quantum Chem.* **2013**, *113* (18), 2110–2142.
- (145) Sato, S.; Morikawa, T.; Saeki, S.; Kajino, T.; Motohiro, T. Visible-Light-Induced Selective CO₂ Reduction Utilizing a Ruthenium Complex Electrocatalyst Linked to a P-Type Nitrogen-Doped Ta₂O₅ Semiconductor. *Angew. Chemie - Int. Ed.* **2010**, *49* (30), 5101–5105.
- (146) Mathivathanan, L.; Torres-King, J.; Primera-Pedrozo, J. N.; García-Ricard, O. J.; Hernández-Maldonado, A. J.; Santana, J. A.; Raptis, R. G. Selective CO₂ Adsorption on Metal-Organic Frameworks Based on Trinuclear Cu₃-Pyrazolato Complexes: An Experimental and Computational Study. *Cryst. Growth Des.* **2013**, *13* (6), 2628–2635.
- (147) Xiang, Z.; Leng, S.; Cao, D. Functional Group Modification of Metal-Organic Frameworks for CO₂ Capture. *J. Phys. Chem. C* **2012**, *116* (19), 10573–10579.
- (148) Millange, F.; Guillou, N.; Walton, R. I.; Grenèche, J. M.; Margiolaki, I.; Férey, G. Effect of the Nature of the Metal on the Breathing Steps in MOFs with Dynamic Frameworks. *Chem. Commun.* **2008**, No. 39, 4732–4734.

- (149) Chibani, S.; Chiter, F.; Cantrel, L.; Paul, J. F. Capture of Iodine Species in MIL-53(Al), MIL-120 (Al), and HKUST-1(Cu) Periodic DFT and Ab-Initio Molecular Dynamics Studies. *J. Phys. Chem. C* **2017**, *121* (45), 25283–25291.
- (150) Perdew, J.; Burke, K.; Ernzerhof, M. Generalized Gradient Approximation Made Simple. *Phys. Rev. Lett.* **1996**, *77* (18), 3865–3868.
- (151) Zhang, C.; Ai, L.; Jiang, J. Solvothermal Synthesis of MIL-53(Fe) Hybrid Magnetic Composites for Photoelectrochemical Water Oxidation and Organic Pollutant Photodegradation under Visible Light. *J. Mater. Chem. A* **2015**, *3* (6), 3074–3081.
- (152) Guo, D.; Wen, R.; Liu, M.; Guo, H.; Chen, J.; Weng, W. Facile Fabrication of G-C₃N₄/MIL-53(Al) Composite with Enhanced Photocatalytic Activities under Visible-Light Irradiation. *Appl. Organomet. Chem.* **2015**, *29* (10), 690–697.
- (153) Bourrelly, S.; Llewellyn, P. L.; Serre, C.; Millange, F.; Loiseau, T.; Férey, G. Different Adsorption Behaviors of Methane and Carbon Dioxide in the Isotypic Nanoporous Metal Terephthalates MIL-53 and MIL-47. *J. Am. Chem. Soc.* **2005**, *127* (39), 13519–13521.
- (154) Torrisi, A.; Bell, R. G.; Mellot-Draznieks, C. Functionalized MOFs for Enhanced CO₂ Capture. *Cryst. Growth Des.* **2010**, *10* (7), 2839–2841.

Acta Universitatis Upsaliensis

*Digital Comprehensive Summaries of Uppsala Dissertations
from the Faculty of Science and Technology 1884*

Editor: The Dean of the Faculty of Science and Technology

A doctoral dissertation from the Faculty of Science and Technology, Uppsala University, is usually a summary of a number of papers. A few copies of the complete dissertation are kept at major Swedish research libraries, while the summary alone is distributed internationally through the series Digital Comprehensive Summaries of Uppsala Dissertations from the Faculty of Science and Technology. (Prior to January, 2005, the series was published under the title "Comprehensive Summaries of Uppsala Dissertations from the Faculty of Science and Technology".)



ACTA
UNIVERSITATIS
UPSALIENSIS
UPPSALA
2020

Distribution: publications.uu.se
urn:nbn:se:uu:diva-398175